INFORMATION TO USERS

This manuscript has been reproduced from the microfilm master. UMI films the text directly from the original or copy submitted. Thus, some thesis and dissertation copies are in typewriter face, while others may be from any type of computer printer.

The quality of this reproduction is dependent upon the quality of the copy submitted. Broken or indistinct print, colored or poor quality illustrations and photographs, print bleedthrough, substandard margins, and improper alignment can adversely affect reproduction.

In the unlikely event that the author did not send UMI a complete manuscript and there are missing pages, these will be noted. Also, if unauthorized copyright material had to be removed, a note will indicate the deletion.

Oversize materials (e.g., maps, drawings, charts) are reproduced by sectioning the original, beginning at the upper left-hand corner and continuing from left to right in equal sections with small overlaps. Each original is also photographed in one exposure and is included in reduced form at the back of the book.

Photographs included in the original manuscript have been reproduced xerographically in this copy. Higher quality 6" x 9" black and white photographic prints are available for any photographs or illustrations appearing in this copy for an additional charge. Contact UMI directly to order.

UMI®

Bell & Howell Information and Learning
300 North Zeeb Road, Ann Arbor, MI 48106-1346 USA
800-521-0600

An Integrated Optical Microcalorimeter

by

Bryon D. Bhagwandin

A dissertation submitted in partial fulfillment of the
requirements for the degree of

Doctor of Philosophy

University of Washington

1999

Program Authorized to Offer Degree: Department of Bioengineering

Doctoral Dissertation

In presenting this thesis in partial fulfillment of the requirements for the Doctoral degree at the University of Washington, I agree that the Library shall make its copies freely available for inspection. I further agree that extensive copying of the dissertation is allowable only for scholarly purposes, consistent with "fair use" as prescribed in the U.S. Copyright Law. Requests for copying or reproduction of this dissertation may be referred to UMI Dissertation Services, 300 North Zeeb Road, P.O. Box 1346, Ann Arbor, MI 48106-1346, to whom the author has granted "the right to reproduce and sell (a) copies of the manuscript in microform and/or (b) printed copies of the manuscript made from microform."

Signature 

Date 6/3/99

University of Washington
Graduate School

This is to certify that I have examined this copy of a doctoral dissertation by

Bryon D. Bhagwandin

and have found that it is complete and satisfactory in all respects,
and that any and all revisions required by the final
examining committee have been made.

Chair of Supervisory Committee:

Martin A. Afromowitz

Reading Committee:

Martin A. Afromowitz

Roy W. Martin

Viola Vogel

Date: June 3, 1999

University of Washington

Abstract

AN INTEGRATED OPTICAL MICROCALORIMETER

by Bryon D. Bhagwandin

Chairperson of the Supervisory Committee: Professor Martin A. Afromowitz (Adjunct)
Department of Bioengineering

Microcalorimetry is the detection and quantification of small changes of heat in a system. Interferometry as a measuring technique is known for its high degree of sensitivity. Bulk optical interferometry is impractical for microcalorimetric measurements. Interferometric fiber calorimeters suffer from a wide range of environmentally induced perturbations that cannot be distinguished from measurand signals. The current work presents a hybrid integrated optical interferometer intended to measure chemical heats of reaction. The device incorporates a novel design to discriminate between measurand-induced signals and environmentally induced signals. The device is composed of two interferometers that share a single sensing arm.

The overall layout of the device together with detailed design calculations for its individual components are presented. The fabrication process contracted to Photonics Integration Research Inc. (Columbus, Ohio), using flame hydrolysis and reactive ion etching is discussed. Phase resolution is enhanced using an up-sampling interpolation routine. Quantification of phase modulation is carried out using a cross correlation algorithm developed for this work. Details for both signal-processing routines are described. Program source code is included in the appendices. Results from tests evaluating basic operation and characterization of phase response are presented. Initial studies using an electronic heater show the relationship between phase modulation and surface-temperature to be 1.98 deg/°C-mm and 1.61 deg/°C-mm for the two

interferometers. Further characterization studies of the device using 10 μl water droplets at fixed temperatures are described. Results from water droplet studies show the phase modulation as a function of temperature to be 2.74 deg/° C-mm and 2.88 deg/° C-mm for the two interferometers. The relationship between phase modulation and heat from the interferometers is calculated to be 274.33 deg/calorie and 288.04 deg/calorie. The experimental results reported provide a measure of device sensitivity to temperature. Further characterization is necessary to determine the heat capacity of the device and ultimately, the device sensitivity to heat. Finally, suggestions for future work are given along with specific modifications of the system for improved performance.

TABLE OF CONTENTS

LIST OF FIGURES

LIST OF TABLES

ACKNOWLEDGEMENTS

Initial funding for this project came from the Center for Process and Analytical Chemistry at the University of Washington. Additional support was provided through a National Institute of Health Predoctoral Training Grant administered by the Department of Oral Biology (Professor Roy Page, Principle Investigator). I would like to express my appreciation to those individuals, departments, and institutions that facilitated this monetary support. Their commitment to higher education and the advancement of science aided in the development of this project, thank you.

Professor Martin Afromowitz has been a mentor, an advisor, and a friend. I would like to thank him for his enthusiasm, support and patience throughout this project. His technical expertise and ability to distill technical challenges into pragmatic achievable goals was invaluable. It was a pleasure to have a partner in this endeavor who was willing to give ownership and control of the project to me while always being available for help weather at work, at home, or even in Taiwan. Thank you Marty.

I would like to acknowledge Viola Vogel, Roy Martin, Selim Tuncel, and Jacob Hildebrandt for serving on my dissertation committee. I appreciate the valuable contribution to this work resulting from the input and comments made by committee members. I would also like to express my gratitude to Isabel Landsberg from the Department of Bioengineering for tirelessly guiding me through the administrative processes and to Mandy Halligan for her editing expertise.

At times, as a graduate student, it seems only fellow graduate students understand the trials, frustrations and excitement that comes during the tenure. I would like to thank Mimi Mar and Carrie Cornish, for listening to the wide range of emotions arising from this project and supporting me through them all. I am grateful to Brian Read because his

friendship, engineering sense and experiences which often proved helpful and encouraging. The inquisitiveness about the project by my good friend Nicolas Loebel provided intellectual stimulation, his technical expertise was helpful through a number of discussions, his encouragement was unfailing, and at times our common interests provided necessary distractions. Thank you Nick.

I am indebted to the management and staff at Bio-Preserve Medical Corporation. They permitted me to take time off whenever it was necessary to conduct research, write this dissertation, or take scheduled examinations. They also generously permitted me to use their computer resources to write the dissertation. For this I am appreciative.

Thank you to my mother Doreen, my sister Deborah, and my brother Omroa for your generous love and support. Your undying belief in me was an encouragement many times throughout this work. To Gaston Cogdell, my father-in-law, I apologize for depriving you the opportunity to ask me, yet again, when I think I will finish ☺. More seriously, thank you to Gaston and Jenelle Cogdell and to Shalmah Lee Prince, my sister-in-law, for your love and favor during this endevor.

A very special debt of gratitude goes out to my best friend and wife, Sarah. Your love, support, patience, and tender affection during this work are deeply appreiciated.

Finally, whatever I do in life, I know that my God sustains me. This project has been no different. For the strength to continue, the security when unsure, and the peace of mind when anxious throughout this task, I give thanks and glory to God.

DEDICATION

For Sarah Leila and Samuel Gaston

INTRODUCTION

INTEGRATED OPTICS

The field of integrated optics has been growing ever since Miller proposed the concept [Miller 1969]. Initial research and development was driven by the communications industry, but now integrated optical devices have found applications in other fields such as chemistry, medicine, and computing [Najafi 1992]. Early development in the field focused on ion diffused planar waveguides [Burgess 1990]. Work continues in planar waveguides because it is ideal for investigation of thin films and monolayer assemblies, but a significant amount of work has been published on the development and optimization of ion diffused channel waveguides [Poszner 1991, Walker 1983b, Ramaswamy 1988a]. Also, Najafi has written a good introduction and overview to ion exchange integrated optics [Najafi 1992].

Another technique for fabrication of integrated optical devices is that of assisted dielectric deposition (chemical vapor deposition, or flame hydrolysis). This technique affords many advantages including resulting devices with: step index profiles, low propagation losses, and low coupling losses manufactured with LSI fabrication techniques, a tested and reliable process with economical, large volume throughput. Development of this fabrication process has been driven by the optical communications industry because structures fabricated with this process interface ideally with fiber. A number of devices fabricated with this process are commercially available including NxN splitters, couplers, ring resonators, wavelength and frequency multiplexers, switches, and interferometers [Takato 1990, Kobayashi 1997].

In addition to communications applications, integrated optical interferometers have been utilized for gas sensing [Brandenberg 1991], environmental sensing [Boiarski 1991], humidity sensing and refractrometry [Lukosz 1991], and immunosensing [Heideman 1991, Boiarski 1992]. All of these sensors operate on the principle of evanescent sensing, where the waveguide core is exposed to the environment, allowing the evanescent wave propagating in the waveguide to interact with the surface of the device.

CALORIMETRY

Calorimetry is the measurement of heat. The principle of modern calorimetry involves allowing the heat released from a sample to flow into the calorimeter; this heat flux is monitored and differentially nulled, thus providing a measure of heat produced. Sources of heat include latent heat due to phase transition, chemical heats of reaction, and change in pressure. Various techniques have been employed to differentially nullify this type of heat production. A brief overview of calorimetry is shown in Figure 1 below. Microcalorimetry focuses on the measurement of small temperature differences produced by heat from chemical reactions. Recent developments of microcalorimeters include: a thermopile sensor deposited on a Mylar membrane to monitor glucose [Muehlbauer 1989, 1990], an integrated silicon based thermopile sensor to monitor urea and penicillin [Bataillard 1993], and a lithographic thin film sensor used to measure specific heat of single crystals [Riou 1997].

Optical calorimeters based on interferometery have been carried out using fiber [Burgess 1984] and with integrated optics [Enokihara 1988]. In both cases these interferometers suffered from environmental noise interference. The current work describes an integrated optical calorimeter designed to discriminate between signals resulting from environmental noise and those produced by a desired measurand. It is based on two Mach-Zehnder interferometers configured so that they share the same sensing arm.

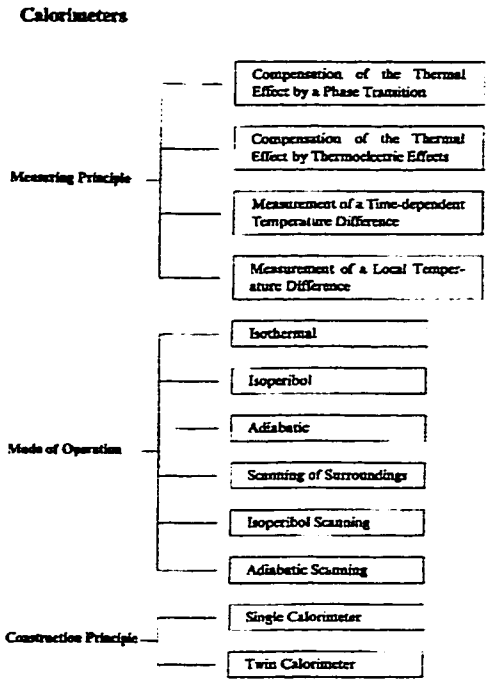

Figure 1. Overview of calorimetry. Adapted from *Calorimetry* [Hemminger 1984].

MOTIVATION FOR THIS WORK

The primary motivation for this work was to provide an interferometrically based microcalorimeter to measure chemical heats-of-reaction. All the interferometric devices referenced above required complex surface preparation, extreme care in etch-concentration and timing-rates, and exhibited coupling losses to the environment at the surface preparation site. This work focused on development of a microcalorimeter that implemented an interferometric sensing modality while excluding the need for complicated surface treatments or direct exposure of the waveguides to the environment. The primary advantages of an integrated optical interferometric approach to

microcalorimetry therefore include: (a) simple design and fabrication, (b) lack of surface preparation, (c) a non-evanescent sensing modality, confining all optical power within the waveguide, thus maintaining optical throughput at the sensing site, and (d) excellent thermal contact between the sensing and reference portions of the interferometer.

CHAPTER 1: INTEGRATED OPTICAL WAVEGUIDE

FABRICATION

Several techniques have been employed to fabricate single mode channel waveguides. The methods most frequently used are ion diffusion [Ramaswamy 1988b, Findakly 1985], or deposition techniques such as chemical vapor deposition [Hanabusa 1989, Kawachi 1990] and flame hydrolysis [Kawachi 1983, 1990, Barbarossa 1992]. Photonic Integration Research, Inc. (PIRI, Columbus, OH) has commercialized the process of flame hydrolysis first reported by Kawachi in 1983 [Kawachi 1983]. Details of the fabrication process are shown in Figure 2 [T. Miyashita 1988]. A silica (SiO_2) glass planar waveguide is formed by flame hydrolysis on a

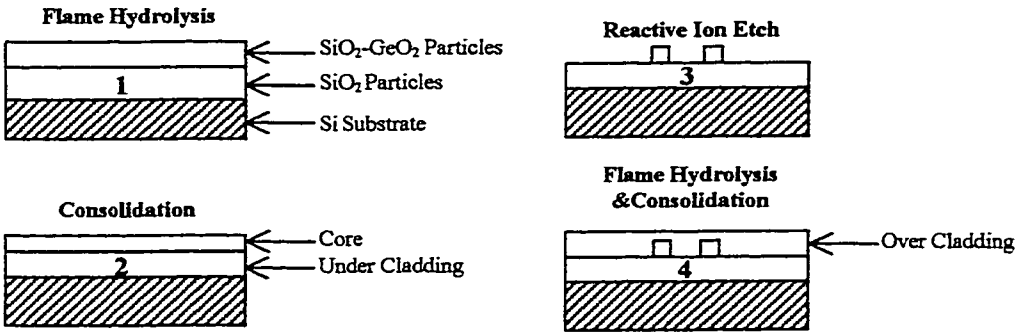

Figure 2. The fabrication process of silica on silicon waveguides. This process uses flame hydrolysis and reactive ion etching. Each step is numbered sequentially.

silicon substrate. Porous glass produced by flame hydrolysis doped with $GeCl_4$ is then deposited on the SiO_2 layer (step 1). Following this deposition, the wafers are heated to 1250 °C for consolidation (step 2). Conventional silicon IC technology is used to create the waveguide core structure. This includes photolithographic masking of the desired core pattern, followed by a reactive ion etching process (step 3). After the core structures are formed, a second layer of silica is deposited by flame hydrolysis and heated for consolidation (step 4). The process results in buried waveguide structures with rectangular/square cross-sectional profiles. This technique is used to produce both multi-mode and single-mode wave guides [Kobayashi 1997]. A maximum resolution of 2 μm is achievable for structures manufactured with this process [Kobayashi 1996]. This includes the manufacture of single waveguides 2 μm in width, as well as the manufacture of two waveguides with a 2 μm separation (wall-to-wall).

The current work involved design, fabrication and testing of a custom Mach-Zehnder interferometer structure for single-mode operation at 632.8 nm. Design and testing was conducted at the University of Washington, Seattle. Early on in the project a significant effort was made to fabricate devices by ion diffusion with unsatisfactory results. A review of this work can be found in Appendix A. Ultimately, design specifications were submitted to PIRI for fabrication using flame hydrolysis and reactive ion etching techniques.

LAYOUT

Previous attempts to use interferometry for calorimetry suffered because the devices were sensitive to such a wide range of environmental interferences making it difficult to isolate the signal from noise [Burgess 1984, Enokihara 1988, Loebel 1998]. The hybrid interferometer shown below was designed to discriminate between signals transduced at the sensing arm from environmental thermal noise impressed upon the device. The device waveguide layout is shown in Figure 3.

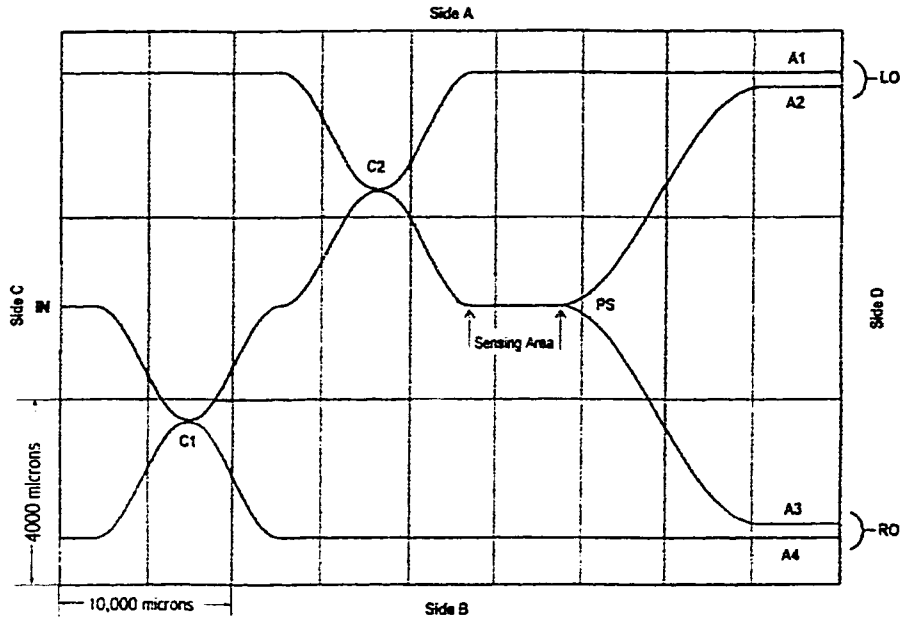

Figure 3. Device waveguide layout: IN optical input port, C1 –6.20 dB directional coupler, C2 – 4.81 dB directional coupler, PS 3 dB power splitter, A1-A4 interferometer arms 1-4 respectively, LO left signal output, RO right signal output.

Let I_0 be the initial power launched into the device, σ_1, σ_2, be the cross-over coupling ratios (assuming an ideal zero loss system) of the two directional couplers (C1, C2) and σ_3 the output-power ratio from the power splitter (PS) respectively. Then from conservation of power

$$A_4 = I_0\sigma_1 \tag{1}$$

$$A_3 = I_0(1-\sigma_1)(1-\sigma_2)(1-\sigma_3) \tag{2}$$

$$A_2 = I_0(1-\sigma_1)(1-\sigma_2)\sigma_3 \tag{3}$$

$$A_1 = I_0(1-\sigma_1)\sigma_2 \tag{4}$$

Here A_j is the power at the output of the j^{th} arm of the device. If radiative losses are included, then Equation (1) – Equation (4) would each have an additional loss term. From the principle of superposition [Hecht 1979] the intensity of the interferogram after recombining the two beam outputs i and j is

$$A_{i,j} = E_i^2 + E_j^2 + 2E_iE_j\cos(\varphi_j - \varphi_i) \tag{5}$$

where E_n is the electrical field and φ_n is the relative phase angle at the output of the n^{th} arm of the device. In Equation (5), $i=1$, $j=2$ for the left output and $i=3$, $j=4$ for the right output. Since power is the square of the electric field $(A = |E|^2)$, Equations (1)-(4) can be substituted into Equation (5) to describe the intensity of the interferogram in terms of the relative phase differences φ_1 and φ_2 for any given input intensity.

The phase of each wave just prior to recombination is given by

$$\varphi_j = k\int_{L_j} n_{eff}(s_j)ds_j \tag{6}$$

where $k=2\pi/\lambda$, s_j is an element of the j^{th} waveguide, Lj is the total arm length of the j^{th} waveguide, λ the vacuum wavelength, and n_{eff} is the effective index of j^{th} waveguide. Index of refraction is a function of temperature and must therefore be considered separately at each element along the length of the waveguides. The phase difference between the waves at the left output (arms one and two) is

$$\Delta\Phi_{LO} = (\varphi_2 - \varphi_1) = kn_{eff}(\Delta L_{2,1}) + const. \tag{7}$$

and

$$\Delta\Phi_{RO} = (\varphi_4 - \varphi_3) = kn_{eff}(\Delta L_{4,3}) + const. \tag{8}$$

for the right output (arms three and four). Here $\Delta L_{2,1}$ and $\Delta L_{3,4}$ are the differences in the lengths of waveguides one and two, and three and four respectively. The constant added to each expression results from the directional couplers, where the effective index is not necessarily the same as the effective index in the simple isolated waveguide. Interferometric phase modulation, as shown in Equations (4) and (5), is a function of the path-length difference in the two arms of the interferometer.

EXPECTED OUTPUT RESPONSE

COMMON MODE RESPONSE

When the optical path length (OPL) of the two arms in an interferometer are unequal, it is considered to be unbalanced. The present device is designed with two (see Figure 3; LO and RO) unbalanced interferometers that are also unbalanced with respect to one another. If all arms are heated equally along their entire length (common mode heating), the phase change in the two central arms will be the same ($\Delta\varphi_2 = \Delta\varphi_3$) because both arms share a single wave guide up to the 3 dB power splitter ($\sigma_3 = 1/2$) and thereafter are identical in length. Since the coupling lengths of C_1 and C_2 (Figure 3) are different, L_1 is not equal to L_4, and the two outer arms (one and four) will produce different phase changes $\Delta\varphi_1 \neq \Delta\varphi_4$. This implies that $\Delta\Phi_{LO}$ and $\Delta\Phi_{RO}$ will differ for common mode heating, and the ratio of these responses must be considered in order to compensate for the differing phase modulations.

MEASURAND PERTURBATION RESPONSE

The device is designed to distinguish OPL perturbations occurring at the sensing area of the device (see Figure 3) from other perturbations. This distinction is observed in the relative direction of phase change by the two output interferograms. Let φ_1, φ_2, φ_3, and φ_4 be the initial phase from waves in arms 1-4 respectively. The initial phase differences in the left output and the right output given in Equation (7) and (8) respectively are φ_2-φ_1 and φ_4-φ_3. Consider a perturbation at the sensing area resulting in a $\delta\varphi$ shift in phase. This shift is added to the initial phase in arms two and three, and therefore Equations (7) and (8) become

$$\Delta\Phi_{LO} = (\varphi_2 - \varphi_1) + \delta\varphi \tag{9}$$

and

$$\Delta\Phi_{RO} = (\varphi_4 - \varphi_3) - \delta\varphi \tag{10}$$

The response of the device to perturbations at the sensing area results in opposing phase modulations. The magnitude of the phase modulation detected at the left and right outputs is only equal if the two interferometers are balanced with respect to one another [i.e. $(\varphi_2 - \varphi_1) = (\varphi_4 - \varphi_3)$]. If this is not the case, prior calibration of the common mode response from each output is required to properly assess measurand-induced perturbations. This characteristic of opposed phase modulations resulting from a measurand perturbation can be used to distinguish such perturbation from environmental influences as discussed below.

GRADIENT RESPONSE

The imbalance between the two interferometers produces asymmetric phase modulation for a static thermal change. Compensation for this imbalance can easily be achieved as discussed above. A more challenging issue is compensation for noise perturbations that may exist simultaneous with a measurand perturbation at the sensing region. It is known that an isolated perturbation occurring at the sensing area results in phase modulations that are opposite in direction. If a thermal gradient moves across the device in the absence of a measurand perturbation, the resulting phase modulations from the two outputs will be in the same direction. As an illustration, consider a linear thermal gradient *h(x)* wide enough to engulf the entire device with decreasing temperature from side B to side A (see Figure 4).

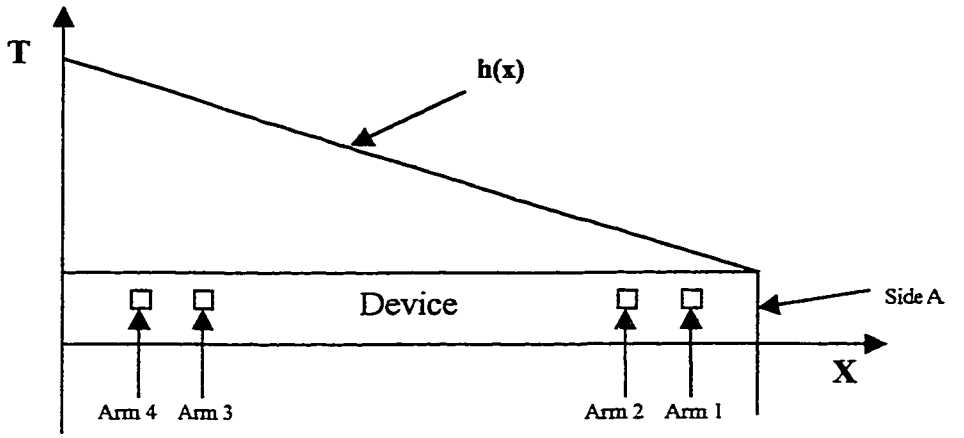

Figure 4. Temperature gradient *h(x)* across the device. The gradient decreases from side B to side A (end view).

In this case, the thermally induced phase shift ($\delta\varphi_j$) in arm four will be greater than that in arm three which will be greater than in arm two which will be greater than that in arm one. The phase difference from the left output will than be:

$$\Delta\Phi_{LO} = (\varphi_2 + \delta\varphi_2) - (\varphi_1 + \delta\varphi_1) = (\varphi_2 - \varphi_1) + (\delta\varphi_2 - \delta\varphi_1) \qquad (11)$$

and from the right output:

$$\Delta\Phi_{RO} = (\varphi_4 + \delta\varphi_4) - (\varphi_3 + \delta\varphi_3) = (\varphi_4 - \varphi_3) + (\delta\varphi_4 - \delta\varphi_3). \qquad (12)$$

Since $\delta\varphi_2 > \delta\varphi_1$ and $\delta\varphi_4 > \delta\varphi_3$, the term $(\delta\varphi_2 - \delta\varphi_1)$ can be written as $+\delta\varphi_{LO}$, and the term $(\delta\varphi_4 - \delta\varphi_3)$ can be written as $+\delta\varphi_{RO}$. This implies that Equations (11) and (12) can be written as:

$$\Delta\Phi_{LO} = (\varphi_2 - \varphi_1) + \delta\varphi_{LO} \tag{13}$$

and

$$\Delta\Phi_{RO} = (\varphi_4 - \varphi_3) + \delta\varphi_{RO} \tag{14}$$

The response of the device resulting from this gradient example shows unidirectional phase modulation for both outputs.

The characteristic unidirectional phase response to thermal gradients and the bi-directional phase response to measurand perturbations provides a unique signature that can be used to discriminate between the two. If the common mode and gradient phase responses from each side of the device are characterized, an analysis routine could be developed and used to isolate the measurand signal. Knowing the common mode phase response from each side, phase modulation from a signal at the sensing site in the absence of thermal noise can be equalized by some constant k ($+\Delta\Phi_{LO} = -k\Delta\Phi_{RO}$). In the presence of a thermal gradient, the two outputs will not be equalized by the constant k ($+\Delta\Phi_{LO} \neq -k\Delta\Phi_{RO}$). However, if the device is characterized such that the phase response from a thermal gradient is known, the output signals could be processed through a routine that would subtract away the appropriate thermal gradient response from each side. This process would yield the characteristic output signal observed from a perturbation at the sensing site in the absence of thermal noise ($+\Delta\Phi_{LO} = -k\Delta\Phi_{RO}$).

ELECTROMAGNETIC MODE THEORY

Maxwell's equations provide the basis for understanding the transmission and propagation properties of electromagnetic waves in dielectric substances. This basic mode theory is well known and can be found in any textbook of electromagnetic theory. A detailed overview of the subject will not be covered here. It is worth noting, however, that the waveguides used in this work have a square cross-sectional profile. The exact solution to the wave equation in this situation (Figure 5) has never been obtained. However, Marcatili derived an approximate solution to the rectangular waveguide problem [Marcatili 1969b]. In this approximation, it is assumed that modes in the guide are tightly bound, that is, propagate well above "cutoff".

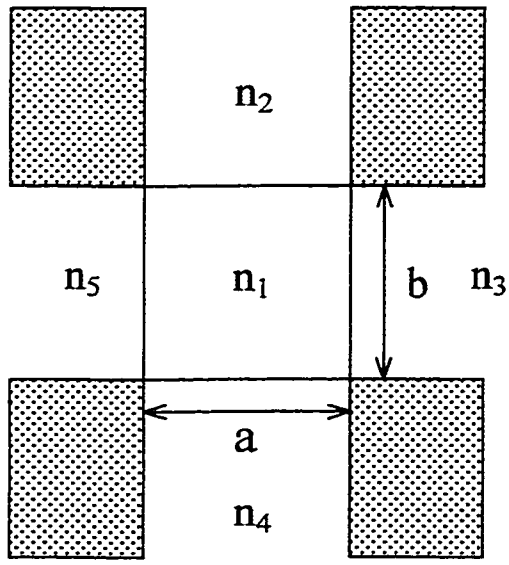

Figure 5. Cross sectional view of a rectangular waveguide. Here n_i is the index of refraction for a given region. The region with index n_1 is the waveguide core. In the present case, $n_1 > n_2 = n_3 = n_4 = n_5$ and a = b.

The meaning of this assumption can be easily understood by considering the case of a circular-core waveguide. Let r_0 be the core radius, n_1 the core index, and n_2 the cladding index, then the modal propagation parameter V is defined as [Senior 1985]

$$V = \frac{2\pi r_0}{\lambda}\sqrt{n_1^2 - n_2^2}\,. \tag{15}$$

The mode fields in circular-core waveguides are described by Bessel functions $J_n[(u_{n,m})(r/r_0)]$ in the core and $K_n[(w_{n,m})(r/r_0)]$ in the cladding. Modal propagation "cutoff" occurs when

$$u_{n,m} > \frac{2\pi r_0}{\lambda}(n_1^2 - n_1^2)^{1/2}\,. \tag{16}$$

For single mode propagation, cutoff first occurs at the root $J_0\,(u_{0,1}) = 0$, corresponding to $V = 2.405$. Equation (16) shows that for a given wavelength, reduction in core size and/or decrease in the core-cladding index differential may induce cutoff.

Turning back to Marcatili's approximation and Figure 5, the field in regions two, three, four, and five decays exponentially with most of the power confined to region one. The cross sectional field distribution for the first order mode is shown in Figure 6.

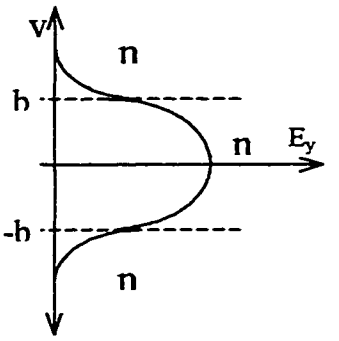

Figure 6. Primary mode field (E_y) distribution in a rectangular waveguide with core width *b*. A cosine function inside the core and an exponential decay in the cladding.

The power in the shaded regions of Figure 5 is assumed to be small enough to be neglected. Marcatili compared his approximate solutions to the results obtained from computer simulations [Godell 1969]. He also compared his approximations to the case where the guide cross sectional profile is circular (a situation where a closed form solution can be obtained). The results show the Marcatili approximations to be very close to both the computer simulations and the case where the guide cross section is circular. A difference does occur in the mode coupling between two guides in close proximity to one another. Assuming the circular guide diameter is equal to the widths of the rectangular guides, the power transferred from one guide to the other in the circular guide case is slightly smaller than for the rectangular guides, assuming equal coupling distance.

DIMENSIONS

The fabrication process carried out by PIRI resulted in a core/cladding index difference (Δ) of 0.69% with a maximum structural resolution of 2 μm. The index of refraction of SiO_2 is 1.4568 at a wavelength of 632.8 nm. These constraints provided the initial conditions for the design process. By approximating the waveguide structure to have a circular cross section, the guide core radius can be written as [Senior 1985]

$$r_0 = \frac{V\lambda}{2\pi(2\Delta)^{1/2}} \tag{17}$$

where V is the normalized frequency, λ is the wavelength in μm, n_1 is the core index (n_2 is the cladding index), and Δ is defined as

$$\Delta = \frac{n_1^2 - n_2^2}{2n_1^2} \approx \frac{n_1 - n_2}{n_1} \qquad \text{for } \Delta << 1. \tag{18}$$

As discussed above, cutoff for a single mode circular-core waveguide is $V < 2.405$. Substituting Equation (18) into Equation (17) and solving gives a waveguide radius of 1.4061 μm and a guide diameter of 2.8122 μm for single-mode operation.

The calculated diameter for a single-mode circular-core guide provides an estimate for the width of a rectangular cross-sectional-core single-mode waveguide. Figure 7 diagrams a conservative relationship between the diameter of a single mode circular core and a single mode rectangular core. A circular diameter of 2.8 μm corresponds to a width of 1.98 μm. Consequently, a core width of $a=2.0\ \mu m$ was used in all design calculations.

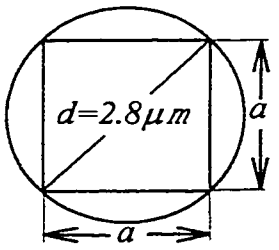

Figure 7. Cross sectional view of rectangular and circular waveguide

CHAPTER 2: WAVEGUIDE COMPONENT DESIGN

The power splitter, S-bend, and directional coupler are the three primary structures involved in the design of most integrated optical devices. Until recently, designing these structures was limited to the analytical approximation and the numerical integration method. Analytical approximations, like that of Marcatili [Marcatili 1969_1, Marcatili 1969_2] and others [Yajima 1978, Cassidy 1993], while useful for providing an understanding of general mode propagation principles, are generally not accurate enough for use in design. S. M. Saad has conducted a review of the numerical methods utilized to compute the modes in arbitrary shaped guides [Saad 1985]. Early work by Godell used cylindrical space harmonics to analyze rectangular guides with aspect ratios (width to height) between one and two [Gdoell 1969], and Schlosser and Unger analyzed guides with larger aspect ratios using rectangular harmonics and numerical methods [Schlosser 1966]. Some examples of the numerical integration methods include the technique of beam propagation based on fast Fourier transform [Feit 1978], and on finite-difference [Accornero 1990], and the technique of mode propagation based on Fourier expansion [Henry 1991]. These numerical methods do provide accurate results, however writing the computer code can be time consuming and if accurate, routines are memory and CPU-time intensive. A finite-difference wave propagation model of a 3-way power-splitter was developed for the present work. The CPU computation time required was in excess of 10 hours per iteration using a Macintosh II-SI personal computer. It was not possible to model the entire structure because the mesh required for the problem was too large for all practical purposes.

Recently, a technique for designing integrated optical waveguide structures based on a set of normalized parameters was introduced [Rasmussen 1994a, Rasmussen 1994b]. Normalized parameters were derived for S-bends, power splitters and directional couplers. These derivations were based on Marcatili's analysis of bends in optical

dielectric guides [Marcatili 1969a]. This technique was used in the present work to design the desired integrated optical device. The resulting design parameters were then used to produce a scaled AutoCAD drawing supplied to Photosciences, Inc. (Torrance, CA). Photosciences, Inc. created a photolithographic mask used by PIRI in the device fabrication process. An overview of the design theory and design results for each component follow.

S-BENDS

Consider the cosine-shaped S-bend shown in Figure 8 connecting two straight sections displaced by distance *d*. As shown, the waveguide width (and height) is *a*, the S-bend has length *L*. The core index is n_1 and the cladding index is n_2. In this analysis, it is assumed that the waveguide bend radius *R* is much larger than the guide width ($R>>a$), and that the waveguides are weakly guiding ($n_1 \approx n_2$).

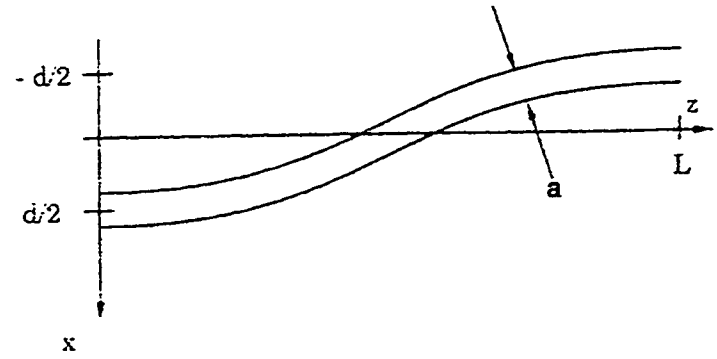

Figure 8. Geometry of cosine-shaped S- bend of length *L*, width *a*

The normalized transverse propagation constant *(U)* in the *x*-direction is defined to be [Senior 1985]

$$U = a(n_1^2 k^2 - \beta^2)^{1/2} \tag{19}$$

where k is the free space wave number and β is the complex propagation constant of the optical field. Following Marcatili's analysis for bends in dielectric waveguides [Marcatili 1969a], the transverse propagation constant U becomes

$$U = u_0(1 + \frac{2C}{u_0} - iA) \tag{20}$$

where u_0 is the normalized transverse propagation constant for a straight waveguide. The term $2C/u_0$ represents the coupling loss at the junction between the straight and curved section of the same guide and A represents the radiation losses. Further,

$$\frac{2C}{u_0} = \frac{1}{8\sqrt{2\pi}} \frac{B^3}{u_0^2} \frac{\lambda}{R} \frac{n_2^{1/2}}{\Delta n^{3/2}} \tag{21}$$

and

$$A=\frac{1-(\frac{u_0}{\pi B})^2}{2+\pi\sqrt{1-(\frac{u_0}{\pi B})^2}}\exp\{-\frac{4\pi}{3}\frac{(\Delta n)^{3/2}}{n_2^{1/2}}\frac{R}{\lambda}[1-(\frac{u_0}{\pi B})^2(1+\frac{2C}{u_0})^2]^{3/2}\} \tag{22}$$

where B is the normalized frequency. Since the approximation $(n_1 \approx n_2)$ can be used for weakly guiding waveguides the propagation constant β can be written as

$$\beta \approx \frac{2\pi}{\lambda} n_2 \tag{23}$$

and

$$\sqrt{n_1^2 - n_2^2} \approx \sqrt{2n_2\Delta n}\,. \tag{24}$$

This implies that the normalized transverse propagation constant for a straight waveguide

$$u_0 = a(n_1^2 k^2 - \beta^2)^{1/2} \tag{25}$$

is only a function of the normalized frequency, B

$$B \approx 2a\sqrt{2n_2\Delta n}\,. \tag{26}$$

Looking now at the loss Equations (21) and (22), if u_0 is only a function of B then for a given normalized frequency, bending loss is determined by the quantity

$$F_s = \frac{R(\Delta n)^{3/2}}{\lambda n_2^{1/2}}. \tag{27}$$

Turning now to the S-bend radius of curvature R, for a cosine-shaped S-bend,

$$R = \frac{1}{x''(z)} = \frac{2L^2}{\pi^2 d}\frac{-1}{\cos(\pi z / L)} \tag{28}$$

and it is clear that

$$F_s = \frac{|R_{\min}|}{\lambda}\frac{(\Delta n)^{3/2}}{n_2^{1/2}} = \frac{2L^2}{\pi^2 d}\frac{(\Delta n)^{3/2}}{\lambda n_2^{1/2}}. \tag{29}$$

F_s, as given by Equation (29), is the characteristic normalized bend loss parameter for cosine-shaped S-bends. This parameter has been verified "by numerous calculations of the bend losses for a large number of combinations of the involved parameters; a, λ, d, L,

Δn, and n_2" [Rasmussen 1994b]. Figure 9 shows a set of design curves calculated by an accurate 3-D beam propagation method.

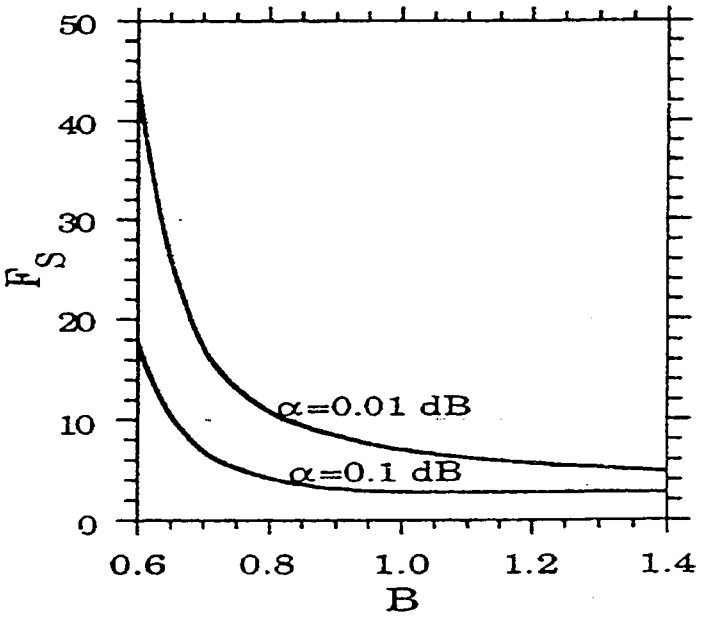

Figure 9. Design curves for a cosine-shaped S-bends (from [Rasmussen 1994a]).

The length L necessary to keep losses below a certain level α, within an S-curve can now be determined through the following procedure; 1) calculate the normalized frequency B, 2) read F_s corresponding to the design loss α, from Figure 9, and 3) calculate L according to Equation (30).

$$L = \pi \sqrt{\frac{F_s \lambda d (n_2)^{1/2}}{2(\Delta n)^{3/2}}}. \tag{30}$$

POWER SPLITTER

The geometry for a symmetric Y-shaped 3-dB power splitter is shown in Figure 10. It consists of two cosine-shaped S-bends of length L and offset d. The power losses occurring in this

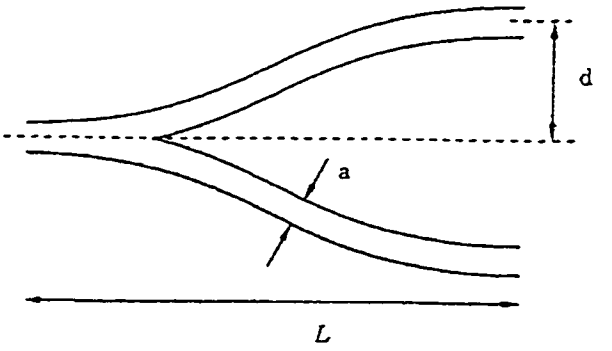

Figure 10. Geometry of a symmetric 3-dB power splitter constructed from two cosine-shaped bends

structure come primarily from bending losses, as described in the previous section, and mode conversion losses [Yajima 1978, Tsutsumi 1988]. Mode conversion losses arise if the taper between the left side (single mode) of the device and the branching structure on the right side is too steep. In this situation, incoming fundamental-mode power will be converted into higher order modes. As the branching structure on the right side of the device returns to a single mode core, power from the higher order modes is lost as radiation. The bending losses decrease with decreasing normalized frequency *(B)* while mode conversion losses will increase with decreasing normalized frequency *(B)*. The characteristic loss curve is therefore expected to show an optimum value for normalized frequency.

Through numerical simulations, Rasmussen et al. have verified that the quantity F_s given in Equation (29) for cosine-shaped S-bends also characterizes the symmetric power splitter shown in Figure 10 [Rasmussen 1994b]. A set of design curves is shown in Figure 11. The design process, similar to that of the S-bend, involves the following three steps; 1) calculate the normalized frequency B, 2) read F_s corresponding to the design loss α, from Figure 11, and 3) calculate L according to Equation (30).

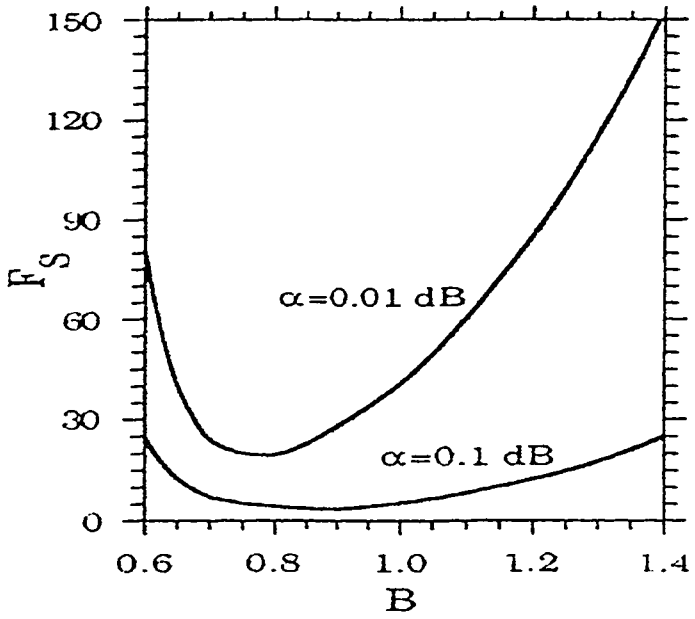

Figure 11. Design curves for a symmetric Y-shaped power splitter (from [Rasmussin 1994a])

DIRECTIONAL COUPLERS

Each side of the symmetric directional coupler is composed of three sub-structures, two S-bends and a straight section. The geometry of the coupler is shown in Figure 12. The field amplitudes

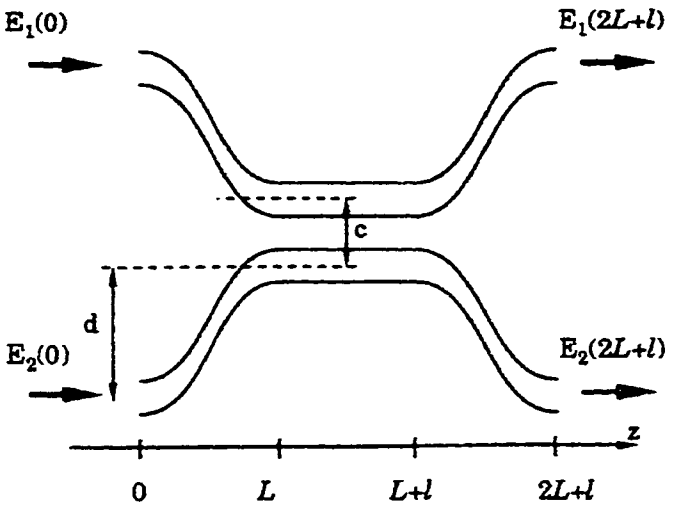

Figure 12. Geometry of a symmetric directional coupler.

$E_1(z)$ and $E_2(z)$ are defined as the overlap integrals of the electromagnetic fields with the fundamental mode of the top and bottom waveguide respectively (Figure 12). At the input and output of the coupler, the guide separation distance is so large that the modes are decomposed into either the sum or the difference of the lowest order eigenmodes of the coupler. If the length (L) and radius of the S-bends are selected so that bending losses are low, then the coupler structure is described by the two lowest-order modes (one symmetric and one antisymmetric). More specifically, the relationship between the input and output fields is given by

$$\begin{bmatrix} E_1(2L+l) \\ E_2(2L+l) \end{bmatrix} = \begin{bmatrix} Cos(\frac{\pi}{2}\frac{l+\Delta l}{L_c}) & -iSin(\frac{\pi}{2}\frac{l+\Delta l}{L_c}) \\ -iSin(\frac{\pi}{2}\frac{l+\Delta l}{L_c}) & Cos(\frac{\pi}{2}\frac{l+\Delta l}{L_c}) \end{bmatrix} \begin{bmatrix} E_1(0) \\ E_2(0) \end{bmatrix} \tag{31}$$

where L_c is the coupling length for 100% transfer of power between two waveguides with a center-to-center separation distance c, and Δl is the length where coupling occurs in the curved part of the structure. The design parameters that must be known for a directional coupler are L_c and Δl. It can be shown [Rasmussen 1994a] that if $\Delta n << l$, the coupling length L_c can be written as

$$L_c = \frac{a^2 n_2}{\lambda} F_c\left(B, \frac{c}{a}\right). \tag{32}$$

Here F_c is a unique function of the normalized frequency B and the normalized guide separation distance c/a. In addition, if $F_s(B)$ is chosen such that losses are kept constant as a function of B, then the relative coupling length of the curved part of the coupler $\Delta l/L_c$ is a function of B and c/a only. Consequently, only F_c and $\Delta l/L_c$ as functions of B and c/a, and F_s as functions of B are needed to design a directional coupler. Design curves for F_c are shown in Figure 13 and for $\Delta l/L_c$ in Figure 14.

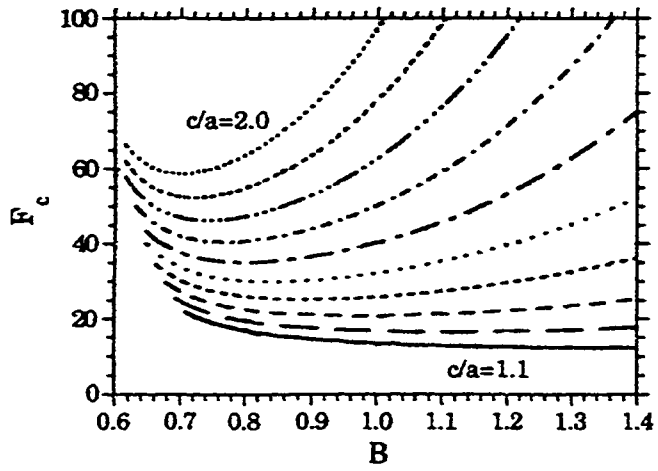

Figure 13. Design curve for straight coupling length of directional coupler (from [Rasmussen 1994b])

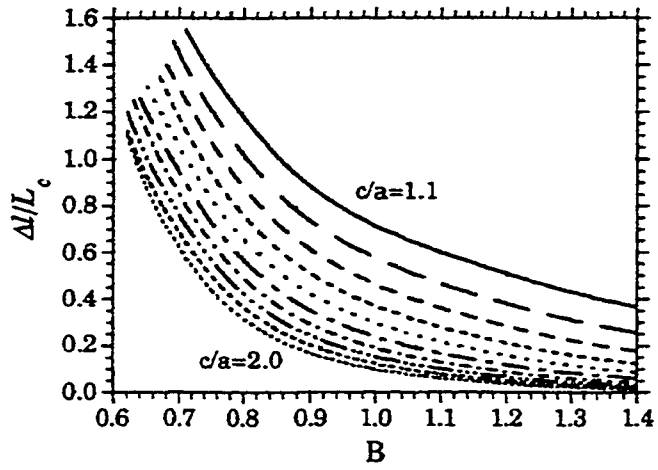

Figure 14. Design curve for curved coupling length of directional coupler (from [Rasmussen 1994b])

The design process involves the following six steps:

1. Determine the length L of the coupler's curved portion using the procedure outlined in the above section on S-bends.

2. Calculate the normalized frequency B.

3. Determine F_c from Figure 13.

4. Using F_c, calculate L_c given in Equation (32)

5. Determine $\Delta l/L_c$ from Figure 14.

6. Calculate the length of the straight portion of the coupler from Equation (33). In this equation, x represents the fraction of power to be coupled from one waveguide to the other.

$$l = \left(x + \frac{\Delta l}{L_c} \right) L_c \tag{33}$$

DESIGN RESULTS

A scaled schematic of the device is shown in Figure 3. It consists of two directional couplers and a 3 dB power splitter. The middle channel on the left side of the device is the input. The right side shows two pairs of output channels (four output channels total). Each of the two pair of output channels produces an interferogram. For any interferogram, maximum visibility occurs when the two interfering beams have equal amplitude. To achieve this, the device was designed so that the first directional coupler divided the power 0.76:0.24 (-6.20 dB) and the second divided it 0.66:0.33 (-4.81 dB). This design choice left ~ 50 % the total input power to be divided 0.5:0.5 (3 dB) by the

coupler. The distribution of output power in each waveguide from top to bottom (Figure 3) was calculated to be –6.01 dB, -5.94 dB, -5.94 dB, and –6.20 dB. The initial known variables are given in Table 1.

Table 1. Initially Known Values Used in Device Design

Symbol	Value	Description
n_2	1.4568	Index of refraction for the silicon dioxide cladding
Δ	0.69 %	Percent difference between core and cladding index
λ	0.6328 μm	Wavelength of light
a	2.0 μm	Waveguide core width required for single-mode
d_{sc}	2500 μm	S-bend offset (shown as d in Figure 8)
d_{ps}	4750 μm	Power splitter offset (shown as d in Figure 10)
c	4.0 μm	Directional coupler center-to-center distance (Figure 12)

The S-bend and power splitter offset values were chosen in order to maximize the number of devices that could be processed on a silicon wafer as shown in Figure 15.

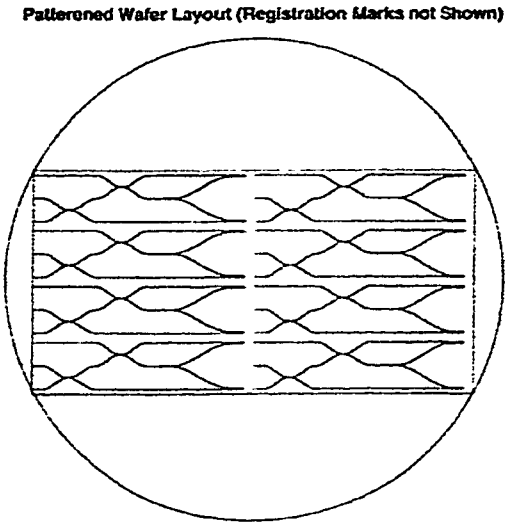

Figure 15. Schematic drawing of silicon wafer with device patterns.

Table 2, Table 3, and Table 4 summarize the design results for the S-bend, power splitter and the two directional couplers respectively.

Table 2. Design Calculation Summary for Cosine Shaped S-Bends

Symbol	Value	Description
B	1.0840	Normalized frequency
F_s	3 (α=0.1 dB)	S-bend normalized parameter from Figure 9
L	5,278.1 μm	S-bend length (Figure 8)
R_{min}	2,258.1 μm	Minimum radius of curvature for α=0.1 dB

Table 3. Design Calculation Summary for Symmetric 3-dB Power Splitter

Symbol	Value	Description
B	1.0840	Normalized frequency
F_s	8 (α=0.1 dB)	power-splitter normalized parameter from Figure 11
L	11,880.6 μm	power-splitter length (Figure 10)
R_{min}	6,021.6 μm	Minimum radius of curvature for α=0.1 dB

Table 4. Design Calculation Summary for Directional Couplers

Symbol	Value	Description
B	1.0840	Normalized frequency
F_c	124 (α=0.1 dB)	Coupling length normalized parameter from Figure13
L_c	1,141.5 μm	Coupling length for 100 % power transfer
$\Delta l / L_c$	0.69	Parameter for coupling in curve from Figure 14
l_{-6dB}	195.2 μm	Straight coupling length for –6.20 dB coupler
l_{-4dB}	297.9 μm	Straight coupling length for –4.81 dB coupler

CHAPTER 3: APPARATUS AND EXPERIMENTAL METHODS

The devices provided by PIRI were placed in the optical configuration diagrammed in Figure 16 below. Light from a helium-neon laser was launched directly into the device using a 10x-microscope objective. Two interferograms were produced, one from the left output and one from the right output. Output pairs were passed through a microscope

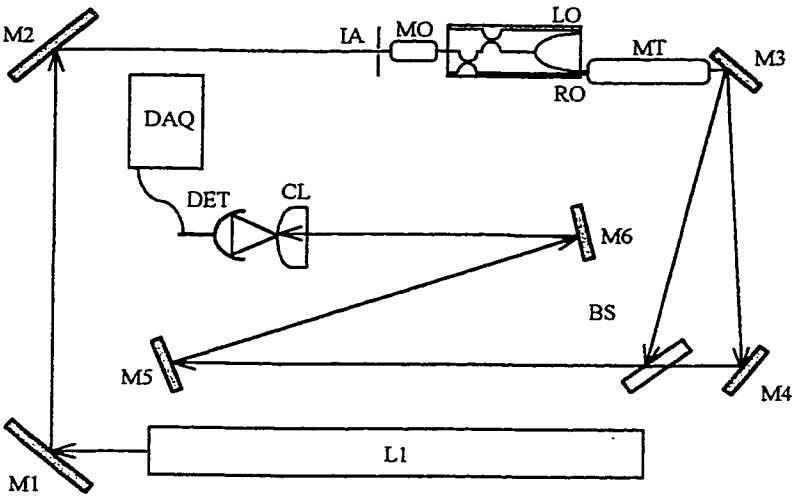

Figure 16. Experimental configuration: L1 HeNe Laser, M1 - M6 mirrors, IA iris aperture, MO microscope objective, LO left output, RO right output, MT microscope tube, BS beam splitter, CL cylindrical lens, DET silicon detector, DAQ PCMCIA-based data acquisition system.

tube configured with a 10x objective and a 10x eyepiece. After traveling through the microscope tube, the diverging beams were superimposed using a beam splitter, mirrors, and a cylindrical lens. The beam was focused onto a silicon charge-coupled photodiode

array (CCD) for detection. Output signals from the array were fed directly to a computer for data acquisition, storage, and analysis.

The microscope tube and its associated deflection mirror (M3, Figure 16) were connected to a translational stage. This facilitated independent collection of data from each of the two output waveguide pairs. Signals were accessible from either side of the device by translating the microscope/mirror assembly and positioning it in front of the two sources. Each source (composed of a pair of waveguide outputs) produced an interferogram when imaged on the 1024 CCD array cells.

Modulation of the interferometric signal was accomplished using two methods. Initially, a length of nichrome (NiCr) wire was configured into a coil 3 mm long and 2 mm in diameter. The NiCr coil was positioned over the sensing area (Figure 3) and brought into contact with the device surface. Increasing amounts of current were programmed through the NiCr coil producing heat, and thereby modulating the interferogram being monitored. Surface temperature of the device was measured for these experiments using a foil thermocouple placed on the device beside the NiCr coil contact point.

A second set of experiments was carried out using heated water droplets to modulate the interferometric signals. Water was heated to a constant temperature using a heater block. A 10 μl droplet was placed on the sensing area of the device while monitoring the interferogram. Heat lost during the transfer of the water from the heater block to the device was measured by placing a heated 10 μl water droplet on a foil thermocouple resting on the surface of the device. This second series of experiments was conducted to more accurately model signal modulation resulting from a chemical reaction occurring on the surface of the device.

POINT SOURCE HEATING

Interferometric signals from the device undergo phase modulations as a result of perturbations in the waveguide optical path length Λ (OPL) ($\Lambda = \int_L n_{eff}(s)ds$, where n_{eff} is the effective index of refraction at points on the path, and L is the entire path length). A schematic of the NiCr heater used to perturb the optical path lengths of the waveguides is shown in Figure 17. The NiCr coil was connected to a power supply so that a programmed current could be driven through it. An ammeter and a voltmeter in the circuit permitted current *(i)* and voltage *(v)* measurements. Joule's law *($P = i^2R$)* gives the transfer function of current to power in the NiCr coil. Some of the electrical power is converted to thermal energy and communicated to the waveguide primarily by conduction and radiation.

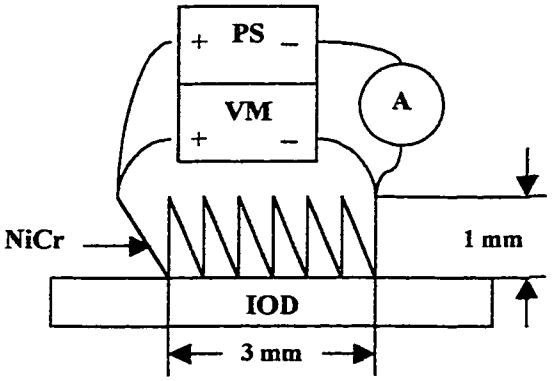

Figure 17. Schematic of the NiCr coil heat source: NiCr nichrome wire, IOD integrated optical device, A ammeter, VM power supply, VM voltmeter. (Not to scale).

Conduction is the transfer of heat from one body at a higher temperature to another body at a lower temperature through physical contact. The heat *(Q)* per unit area *(A)* or heat

flux resulting from conduction is proportional to the spatial temperature gradient [Rohsenow 1973]

$$\frac{Q}{A} = -k\frac{\partial T}{\partial x} \tag{34}$$

The proportionality constant k is a material property known as thermal conductivity.

Thermal radiation is electromagnetic radiation of a body due to its temperature. Calculation of thermal radiation is based on the Stefan-Boltzmann law relating the emitted energy flux of an ideal radiator to the fourth power of temperature

$$E_r = \sigma T^4 \tag{35}$$

Here σ is the Stefan-Boltzmann constant. Most bodies generally do not act as ideal radiators therefore, for most surfaces Equation (35) is modified to

$$E_r = \varepsilon\sigma T^4. \tag{36}$$

The term ε is the emissivity of the surface and takes values between 0 and 1 [Rohsenow 1973]. Equation (34) and Equation (36) show that the amount of electrical power in the NiCr coil that is communicated to the waveguide in the form of heat depends on the

physical properties of the device. The amount of heat actually transferred to the device is difficult to calculate. The difficulty of this calculation was the primary motivation for undertaking the second set of experiments using water droplets for point source heating.

In an effort to more accurately characterize the device-phase-response to temperature and get an initial measure of device phase response to heat, experiments were carried out using water as a heat source. Deionized water and a pipette tip were placed in a test tube. The test tube was placed in a heater block and raised to a set temperature. A 10 μl droplet of water was than extracted from the test tube and placed on the sensing area while simultaneously monitoring the phase modulation at the output of the device.

The device-phase-response to heat can be determined from knowledge of the relationship between heat and temperature for water. A calorie is the amount of heat required to raise one gram of water (1000 μl) one degree centigrade. Therefore 0.01 calories are required to raise a 10 μl water droplet a degree centigrade. Assuming all the heat contained in the droplet is transferred to the device, then an estimate of device sensitivity can be calculated.

Heating the waveguide by any means affects the OPL by a change in physical path length due to thermal expansion or contraction, and by a temperature-induced change in index of refraction. As stated above, phase modulation of the interferogram results from changes in the waveguide OPL. The relationship between phase change and temperature is [Hocker 1979]

$$\frac{1}{L}\frac{\Delta\varphi}{\Delta T}=\frac{2\pi n}{\lambda}\left(\frac{1}{L}\frac{dL}{dT}+\frac{dn}{dT}\right). \tag{37}$$

The term $\frac{dn}{dT}$ is two orders of magnitude larger than the normalized expansion coefficient product, $\frac{1}{L}\frac{dL}{dT}$ for fused silica (SiO_2) [Hocker 1979, Musikant 1985]. The interferometric response is therefore, dominated by the refractive index variation rather than the waveguide length expansion/contraction. Since the linear expansion coefficient is a known physical property of the material, by heating a known length of the sensing area while monitoring the surface temperature and the phase modulation, a length normalized phase modulation with respect to temperature $\frac{1}{L}\frac{d\varphi}{dT}$, a characteristic parameter of the device, can be evaluated.

DATA ACQUISITION

The linear charge-coupled photodiode array used to collect the interferometric spectra was 1024 pixels in length. Each pixel was 13 μm x 13 μm in size. The accompanying interface circuitry was configured for a combined video output and aligned according to the manufacture's specifications. The refresh rate of the array was 81 kHz (set by a RC network on the board). A trigger signal was generated on a separate line to synchronize data acquisition with pixel update rate.

The combined video of the CCD array was connected directly into an analog line of a multifunction data acquisition (DAQ) card. A program was written (see Appendix B) using LabVIEW™ (National Instruments, Austin, TX) to retrieve, display and store the raw data to disk. The program acquired a user-specified number of interferometric spectra (i.e. one sweep of the 1024 CCD array cells) with a variable delay time between each sweep. In addition, when the NiCr coil was used, a digital line on the DAQ card was configured to write an enable/disable signal to the voltage supply driving the coil. The program also incorporated controls for the coil to set up a delay in the initiation of heat and the heat-pulse duration.

SIGNAL PROCESSING

A typical output interferogram is shown in Figure 18. This figure shows that the signal resolution achieved with the CCD array was 30-40 pixels per fringe. Each pixel therefore represents about 10° of phase change. The digital signal processing technique of interpolation was used to improve the signal resolution [Vaidyanathan 1993]. Once higher resolution spectra were obtained, attention was given to phase analysis. A cross correlation operation was conducted on each spectrum with respect to an initial spectrum (one in which the relative phase shift is considered to be 0°). Comparison of the cross correlation spectral peaks, together with knowledge of the phase angle represented by each point, permitted a calculation of the phase shift from one spectrum to the next. An overview of the interpolation routine and the cross-correlation analysis follows.

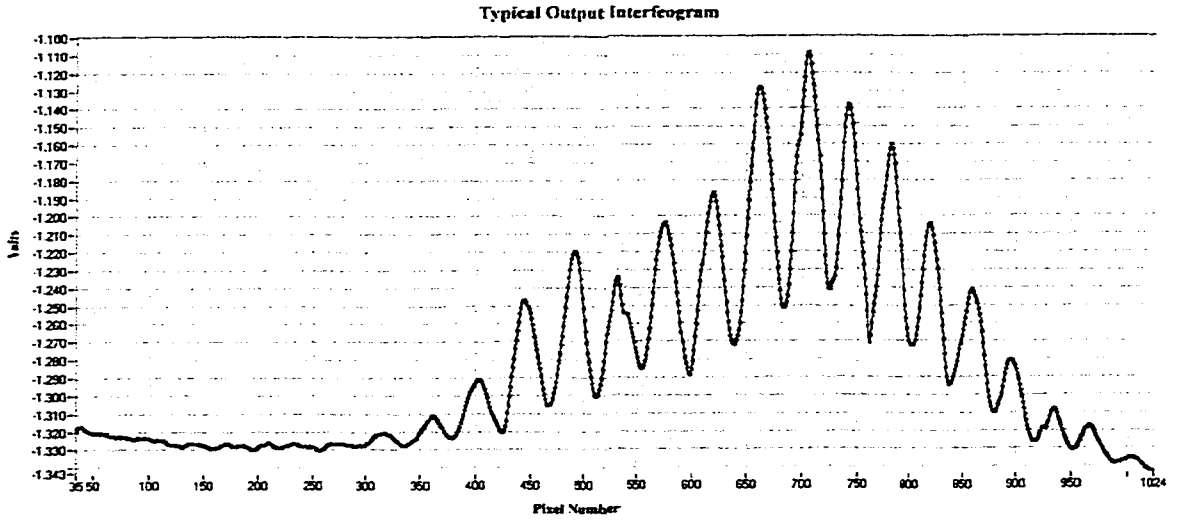

Figure 18. Typical Interferogram

INTERPOLATION

The process of interpolation is required whenever it is necessary to change from one sampling rate to another. When an increase in the sampling rate is desired as in the present case, the process involves interleaving zeros into the data array between sampled data points and passing the array through a low-pass filter. A general system for increasing the sampling rate by an integer value is shown in Figure 19.

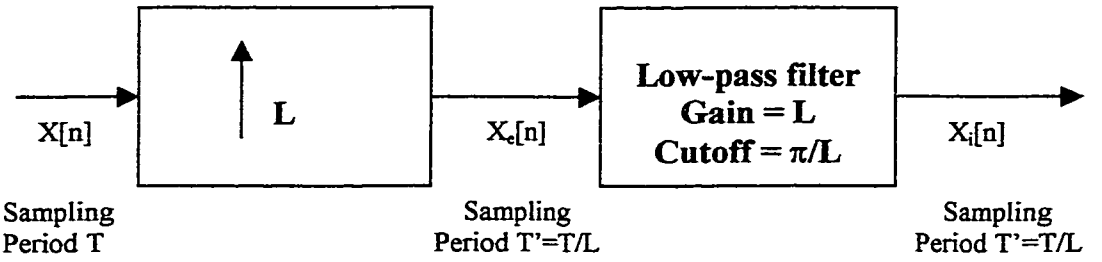

Figure 19. General system for increasing the data-sampling rate by an integer value *L*

If the desired sampling rate increase is a factor of *L*, then the number of zeros to be interleaved is *L-1*. If the original sampling period is *T* and the increased sampling frequency $T' = LT$, then the amplitude scale should be corrected from $1/T$ to $1/T'=1/LT$ corresponding to a gain for the low-pass filter of *L*. Likewise, if the sampling frequency has increased from *T* to *T'* then all information outside of π/T' (Nyquist condition) should be excluded, implying that the low-pass filter cutoff should be set to π/T'. A more detailed explanation of the sampling rate increase process can be found in digital signal processing textbooks [Vaidyanathan 1993].

In practice, ideal low-pass filters cannot be implemented, however, very good approximations can be designed [Oetken 1975]. It has been shown that finite duration impulse response (FIR) filters are preferred to infinite duration impulse response (IIR)

filters for applications of interpolations [Schafer 1973]. Finite impulse response filters have several important and useful characteristics listed below [LabVIEW™ manual 1996].

1) They can achieve linear phase due to filter coefficient symmetry in the realization.

2) They are always stable.

3) The filtering function can be performed using convolution, and as such, a delay can generally be associated with the output sequence given by

$$delay = \frac{n-1}{2} \tag{38}$$

where n is the number of FIR coefficients.

The low-pass filter implemented in the present work uses the Interpolated Finite Impulse Response technique to design a narrow-band low-pass FIR filter [Vaidyanathan 1993]. Table 5 summarizes the design parameter of the interpolation used.

Table 5. Summary of the Interpolation Performed

Parameter	Value
Original sampling frequency	81 kHz
Sampling rate increase	10 x
Pass band frequency (PBF)	~ 450 Hz
Stop-band frequency (SBF)	1.8 x PBF
Attenuation	70 dB
Ripple	± 1%

It should be noted that when utilizing this technique, care must be taken to calculate the delay associated with the filtering process and subtract it from the interpolated signal. The LabVIEW™ code developed for the interpolator used in this work can be found in Appendix C.

CROSS-CORRELATION

The cross correlation $R_{xy}(t)$ of the signals x(t) and y(t) is defined as:

$$R_{xy}(t) = x(t) \otimes y(t) = \int_{-\infty}^{+\infty} x(\tau) y(t+\tau) d\tau, \tag{39}$$

where $\otimes$ denotes the cross correlation.

For a discrete-time function, if h represents a sequence whose indexing can be negative, then let n be the number of elements in the sequence **X**, let m be the number of elements in the sequence **Y** and assume that the indexed elements of **X** and **Y** that fall outside their range equal 0. Specifically,

$$x_j = 0, \; j < 0 \text{ or } j \geq n$$

and

$$y_j = 0, \; j < 0 \text{ or } j \geq m$$

then the cross correlation of **X** and **Y** can be written

$$\boldsymbol{X} \otimes \boldsymbol{Y} = h_j = \sum_{k=0}^{n-1} x_k y_{j+k} \qquad \text{For } j = -(n-1), -(n-2), \ldots, -2, -1, 0, 1, 2, \ldots, m-1. \tag{40}$$

Implementation of the cross correlation transform to the detection of phase shift is accomplished by knowing the phase shift φ corresponding to an adjacent move in the cross correlation peak. Specifically,

$$h_{j+1} - h_j = \Delta\varphi \tag{41}$$

is known. In the present case, the number of points per interference fringe can be determined by finding adjacent peak locations in the interpolated spectrum and dividing by 360°. This phase shift is then the same shift shown in Equation (41) above. Therefore, if an initial interferogram is cross-correlated with itself (auto correlation), the location of the correlation peak can be used to reference any shift in the cross correlation spectra of subsequent interferograms with the initial interferogram. The discrete location of a cross correlation peak relative to the auto correlation peak multiplied by the associated adjacent-point phase shift is equal to the total interference phase change:

$$\Phi = (h_{ccp} - h_{acp})\Delta\varphi \tag{42}$$

where Φ is the total interferometric phase shift, h_{ccp} is the location of the cross correlation peak, h_{acp} is the location of the auto correlation peak and $\Delta\varphi$ is the adjacent- point phase shift. The LabVIEW™ code developed for the cross correlation analysis used in this work can be found in Appendix D.

An alternative analysis of the interferometric spectra was also investigated. It was based on the technique of zero-padded fast Fourier transforms (FFT). An analysis routine was developed (Appendix E) and used on a number of spectra. While accurate, the routine required substantial computer processing time. As a validity check, the results from the cross correlation analysis method described above were compared with those from the FFT routine. The outcome showed that phase shifts calculated using the cross correlation routine produced results that were within ± 1° of the values determined using the FFT

analysis without requiring the CPU overhead. The cross correlation method also produced comparable results to direct peak location comparisons in the interpolated spectra and provided the advantage of automation and insensitivity to amplitude fluctuations during phase modulation.

CHAPTER 4: EXPERIMENTAL RESULTS AND DISCUSSION

Two thermoelectric coolers/heaters (TEC) were incorporated into the experimental apparatus to experimentally model the phase response to common mode heating and thermal gradients. One was placed underneath the device (common mode heater) and one was placed on the side of the device (gradient heater). A heat sink and small fan were placed on the opposite side of the device in an effort to draw heat across the structure. A diagram of this configuration is shown below in Figure 20.

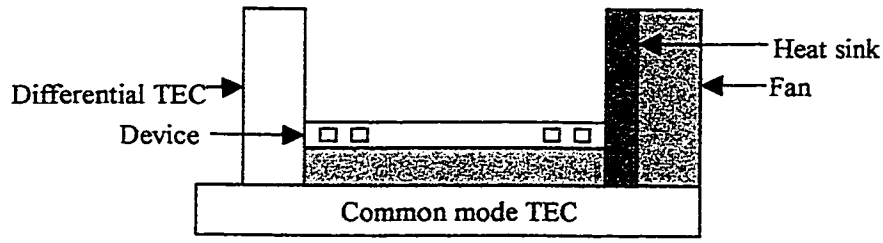

Figure 20. Experimental Layout: TEC thermoelectric coolers/heaters.

Considerable effort was made to characterize the phase response to common mode and gradient heat using the TECs. Unfortunately, physical expansion of the device caused by heating was sufficient enough to alter optical alignment. This alignment change in some instances caused the interferogram to disappear from the detector, and in other instances, caused the Gaussian envelope of interference fringes to shift, thus making phase-shift measurements impossible. Consequently, thermal perturbation experiments focused on point source heating only.

NICHROME COIL HEAT SOURCE

SURFACE TEMPERATURE MEASUREMENTS

Surface temperature of the device was monitored using a foil thermocouple located next to the NiCr coil contact point. The coil, 3 mm in length and 2 mm in diameter, was pulsed for 750 ms with varying amounts of current programmed through it. The thermal profiles for the heating process are shown in Figure 21.

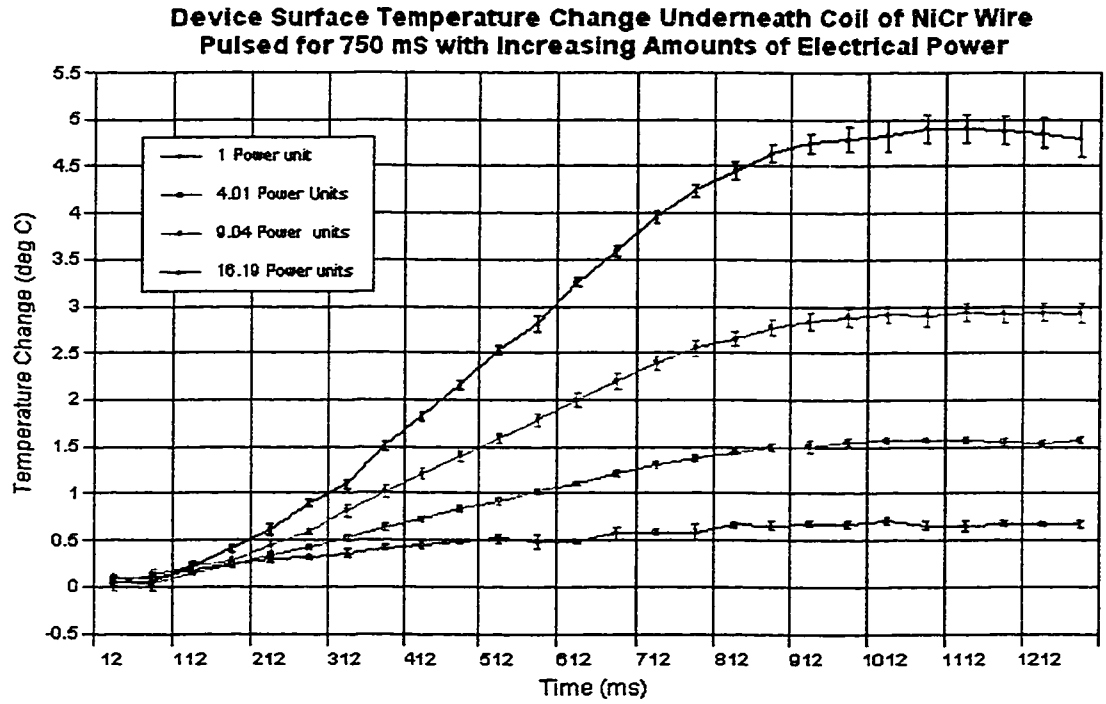

Figure 21. Differential surface temperature profiles from heat generated by a NiCr coil pulsed for 750 ms with increasing amounts of current. Electrical power in the NiCr coil was normalized to 54.8 mW.

The plots are identified by the normalized electrical power calculated based on the programming current. It can be seen that the surface temperature of the device rises throughout the time current flows in the coil and continues for about 150 ms after current

flow stops. After a peak surface temperature is attained for a given power input, the surface temperature exhibits about 300 ms of a quasi-steady state. Thermal profile information was used to correlate phase modulation in the output interferograms to time.

PERTURBATIONS OF THE SENSING AREA

A measurand perturbation of the sensing area was modeled by placing the NiCr coil above the sensing area and pulsing it for 750 ms with varying amounts of current. The resulting phase modulation of the left output is shown in Figure 22. Figure 23 shows the phase modulation measured from the right output. The phase response shown in these

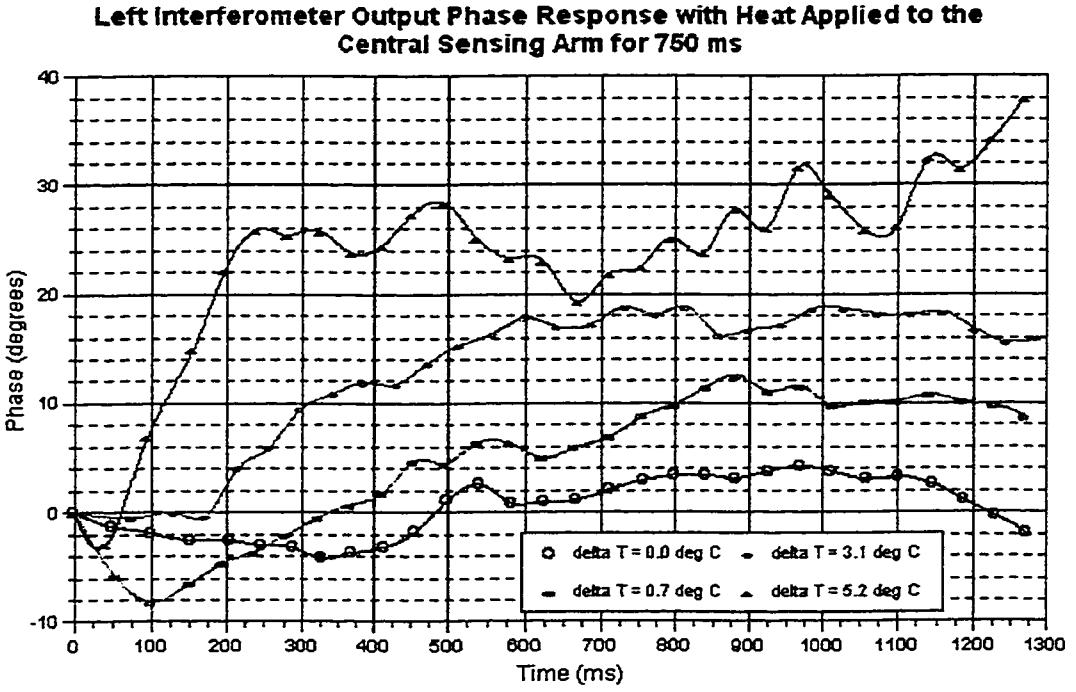

Figure 22. Left output phase response to thermal perturbations from NiCr heater applied to the central sensing arm.

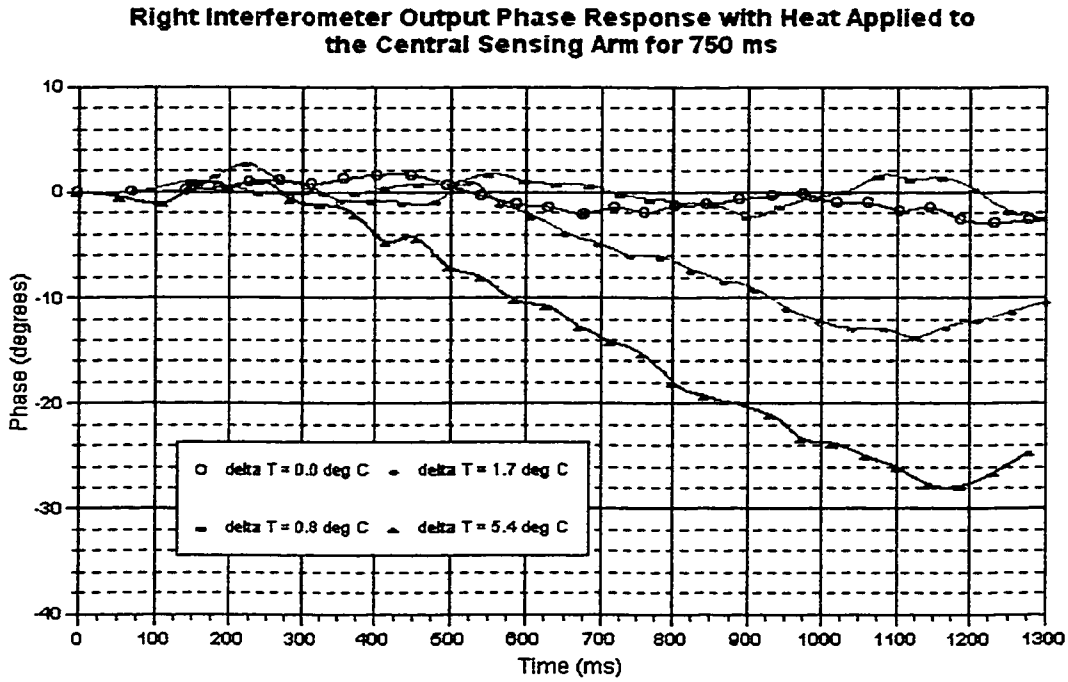

Figure 23. Right output phase response to thermal perturbations from NiCr heater applied to the central sensing arm.

two figures is consistent with the theoretical predictions given in Equation (9) and Equation (10). The two output phase modulations are in opposing directions with the left output phase being shifted positively and the right output phase being shifted negatively. The relationship between phase modulation and temperature given in Equation (37) shows that the phase modulation results from a physical length change due to temperature and an index change due to temperature. The data presented in Figure 22 and Figure 23 is a direct measure of the relationship between phase modulation and temperature. The phase shift per unit temperature is plotted in Figure 24

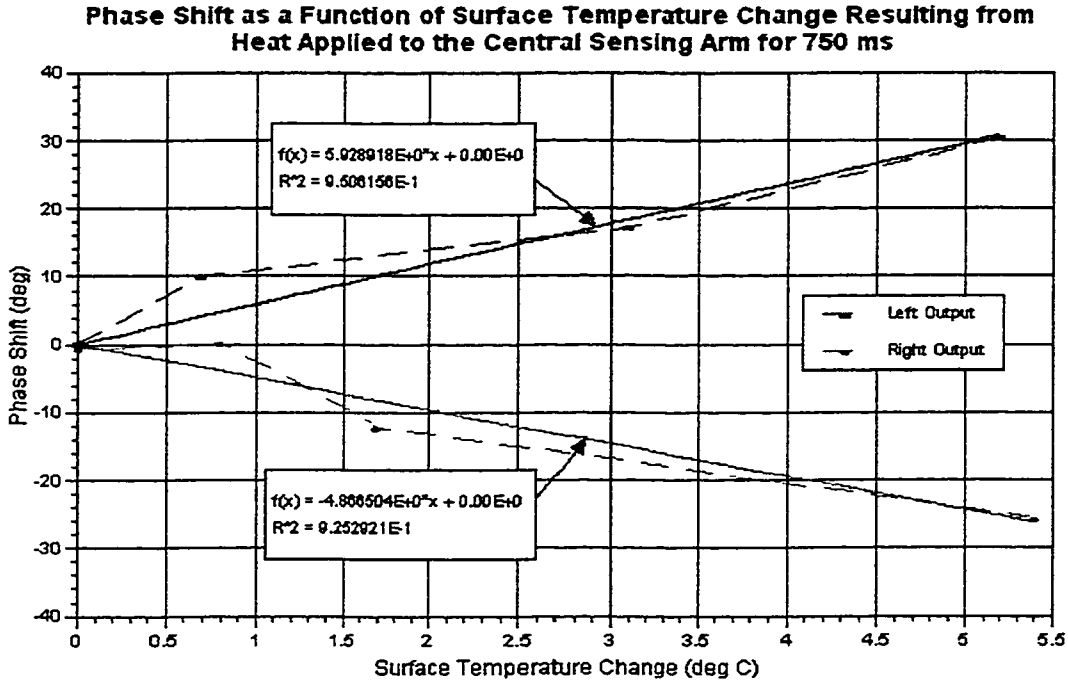

Figure 24. Correlation of phase modulation to sensing-area surface temperature changes produced by NiCr heater coil.

for the right and left output of this device. The left output phase modulation $\Delta\Phi_{LO}$ was 5.93 degrees/°C and the right side phase modulation $\Delta\Phi_{RO}$ was –4.87 degrees/°C. In Equation (37) the change in phase with respect to temperature is normalized to a unit length. Using the length of the NiCr coil (3 mm) as the waveguide heated length (L_l), $\frac{1}{L_l}\frac{\delta\varphi}{\delta T} = 1.98\,\text{deg/°C-mm}$ for the left side output and $\frac{1}{L_l}\frac{\delta\varphi}{\delta T} = 1.63\,\text{deg/°C-mm}$ for the right side. Other work in optical fibers report values of $\frac{1}{L_l}\frac{\delta\varphi}{\delta T}$ close to 6.0 deg./°C-mm

[Loebel 1998, Hocker 1976]. This difference is most likely due to the difference in thermal conduction between the fiber case and the slab waveguide case. The difference in the calculated values of $\frac{1}{L_l}\frac{\delta\varphi}{\delta T}$ for the left side versus the right side was most likely a result of device asymmetry. Heat produced by the coil diffused across the left side waveguides prior to those on the right, producing an asymmetric response between the two signals. This explanation is plausible since the layout of the device (Figure 3) shows the left side outer arm (one) to be in closer proximity to the sensing area than the corresponding arm (four) of the right side. The analysis of a thermal gradient given above predicts that the phase modulation of the left output would move in the same direction as if the sensing area were perturbed (Equation (13) and Equation (9)). If the coil heat diffused over arm one of the device before diffusing over arm four, more of the waveguide comprising the left output would undergo perturbation than the right output.

Differences between reported values for $\frac{1}{L_l}\frac{\delta\varphi}{\delta T}$ by Hocker and by Loebel compared to this work result from differences in material properties used in the various studies. Values for the dependence of refractive index on temperature and for the thermal expansion coefficient vary widely for glass depending on their composition. For example, the thermal expansion coefficient can range from 0.5 – 10.3 x 10^{-6}/°C for silica [Musikant 1985]. In addition, Hocker reports that "$\frac{\delta n}{\delta T}$ is itself a function of temperature of and wavelength, and that tabulated values are averaged over a rather large temperature range and given for only a few wavelengths" [Hocker 1979]. This implies that the value of $\frac{1}{L_l}\frac{\delta\varphi}{\delta T}$ could vary significantly from other studies conducted. Another contributing factor may be the effect of having a waveguide structure anchored to a silicon substrate. Silicon has a thermal expansion coefficient that is an order of magnitude larger then that of silica [Musikant 1985]. This material discontinuity may have an effect of the effective

thermal expansion coefficient of the waveguide. Silicon also has a thermal conductivity two orders of magnitude larger than silica causing it to act as a large heat sink underneath the device [Musikant 1985, CRC Press 1988]. This means heat applied to the surface of the waveguide is rapidly absorbed by the substrate. As a result heat applied to this device may result in a smaller temperature change in the waveguide as compared to the same amount of heat being applied to a fiber. This would in turn effect the overall temperature-dependent phase response $\frac{1}{L_l}\frac{\delta\varphi}{\delta T}$.

Comparison of the temporal response of the phase modulation shows that the left output is modulated much more quickly than the right output. This asymmetry most probably is an additional consequence of diffusion of heat into arm one of the device as previously discussed.

RESPONSE TO TEMPERATURE GRADIENT

The device phase response to a temperature gradient was modeled by locating the NiCr heater above arm four of the device and directly across from sensing area and pulsing it for 750 ms with increasing amounts of current. Phase response from the right output is shown in Figure 25. The thermal perturbations set up by this configuration are analogous to the thermal gradient shown in Figure 4 for the right output. The phase modulation from the right output as given in Equation (14) is directionally opposite to the phase modulation seen when the sensing arm is perturbed (Equation (10)). This oppositely directed phase modulation is observed (Figure 22 and Figure 25) validating the operation of the device and its design. After 600 ms the phase modulation levels off or reverses direction. It was seen in Figure 21 that the surface temperature continues to increase for ~150 ms after current flow in the coil stops. Assuming an isolated system, theory

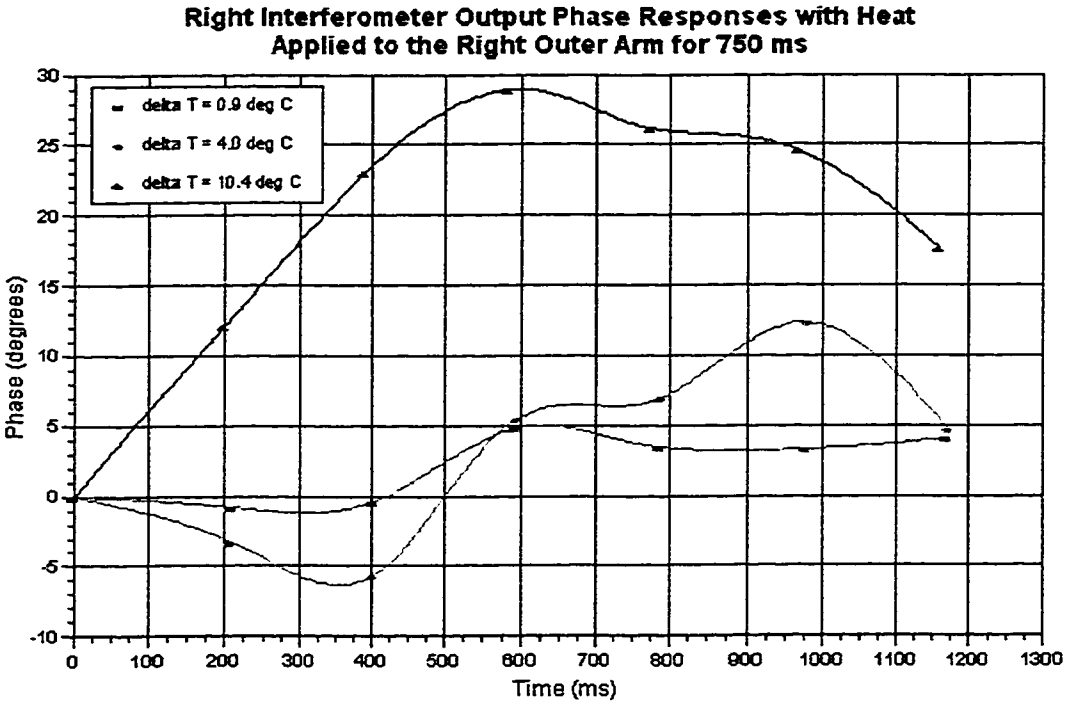

Figure 25. Right output phase-response to thermal perturbations from NiCr heater applied to the right outer arm (four).

(Equation 37) states that the phase modulation in the waveguide will track the thermal profile. The assumption of isolation does not hold in this device and data here suggest that after 600 ms heat from the coil has diffused to the sensing area. As arm three begins to heat, the rate of phase modulation will be reduced. A more detailed analysis is required to make more quantitative or conclusive statements about the dynamics of this situation.

WATER DROPLET HEAT SOURCE

DROPLET TEMPERATURE

It was expected that a 10 μl drop of water would rapidly loose heat when removed from the heating source. Experiments were carried out in order to determine the amount of heat delivered to the surface of the device by the water droplet. Deionized water was placed in a test tube together with a pipette tip. The test tube was placed into a heater block and allowed to equilibrate to a preprogrammed temperature. Temperature of the heater block was determined by placing a foil thermocouple in the heated water. Once the pipette tip achieved thermal equilibrium it was attached to a micropipettor, a 10 μl drop of water was then extracted and dispensed onto a second foil thermocouple located on the surface of the device. Data acquisition from the thermocouple was simultaneously initiated. One hundred readings were collected and averaged from the thermocouple at a rate of 10 Khz (10 ms collection time) at 25 ms intervals for 12.5 seconds. This procedure was repeated five times at five different temperatures. The five spectra collected at each temperature were averaged and are plotted below in Figure 26.

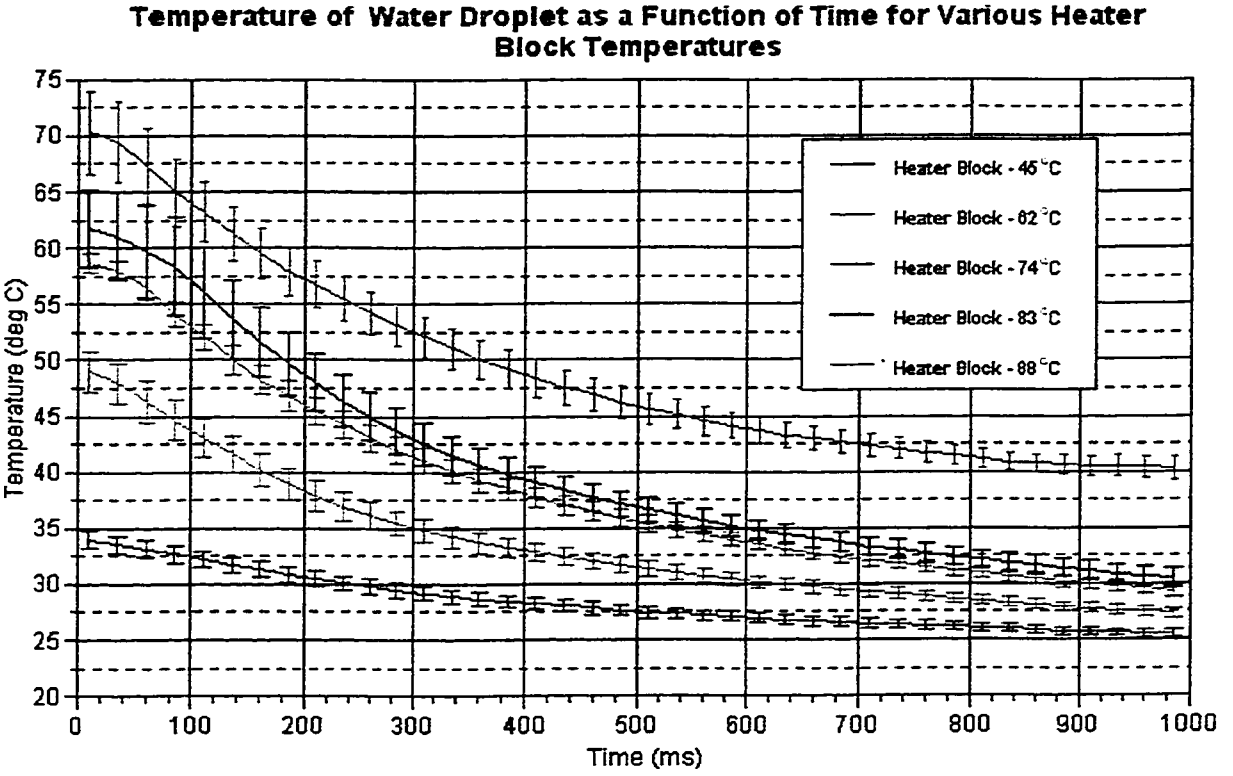

Figure 26. Temperature of a 10 μl water droplet at the surface of the device after being heated to a fixed temperature. Surface temperature of the device was 20 °C.

PERTURBATIONS OF THE SENSING AREA

In order to better model a chemical reaction occurring on the sensing area of the device, heated water droplets were placed on the sensing area while monitoring the interferometric phase modulations at the outputs of the device. Results from these phase modulation studies are shown below. The left side output is shown in Figure 27 and the right output in Figure 28.

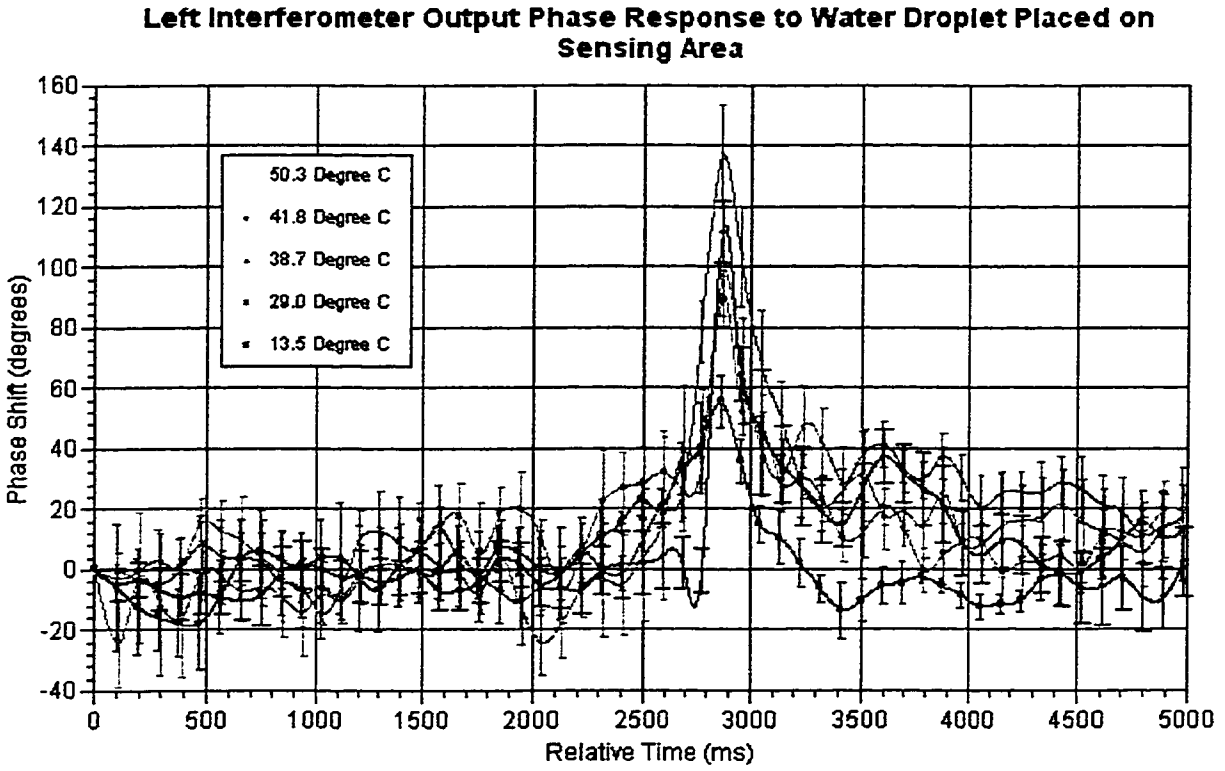

Figure 27. Left output phase response to thermal perturbations from a 10 μl water droplet placed on the central sensing arm. The legend shows the number of degrees centigrade the water droplet was above the device surface temperature.

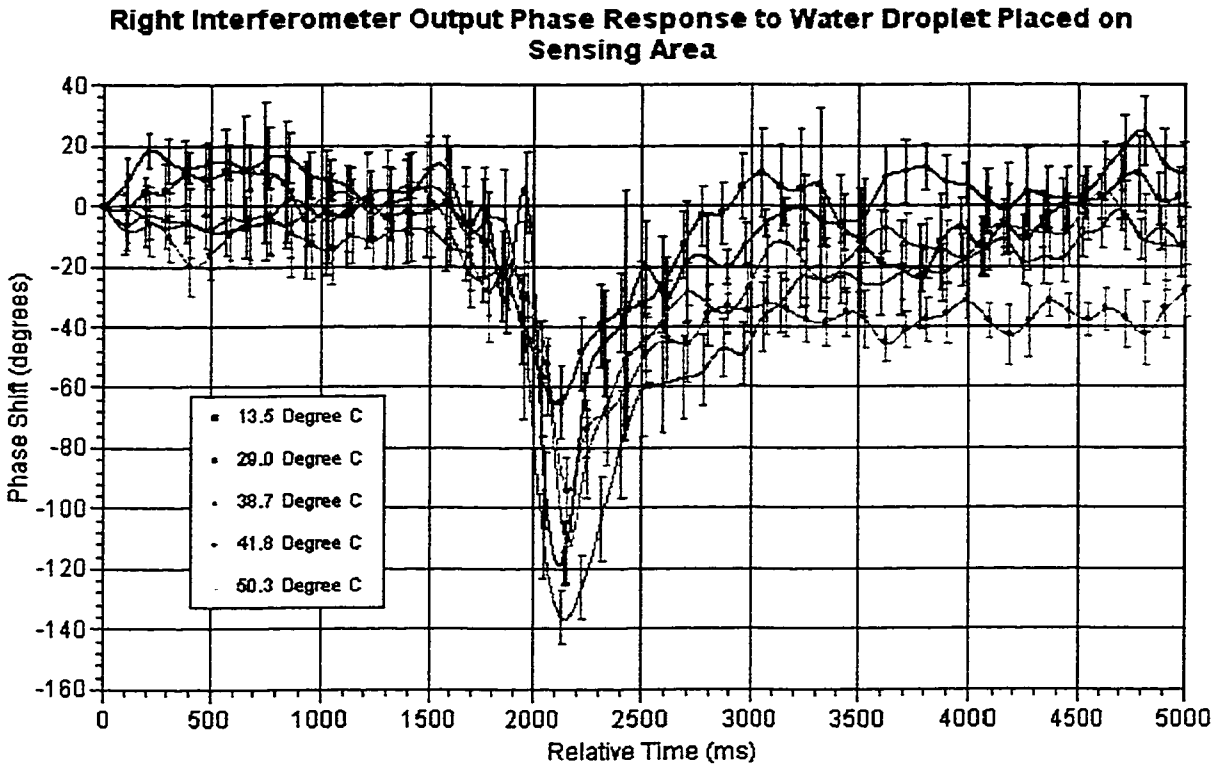

Figure 28. Right output phase response to thermal perturbations from a 10 μl water droplet placed on the central sensing arm. The legend shows the number of degrees centigrade the water droplet was above the device surface temperature.

Data acquisition for this series of experiments was initiated manually. This implies that time shown on the x-axis of Figure 27 and Figure 28 is relative. Data acquisition was initiated sooner when monitoring the left output compared with that of the right. The legend in Figure 27 and Figure 28 shows the number of degrees centigrade the water droplet was above the device surface temperature. The absolute water droplet temperatures are from the data shown in Figure 26.

The surface of the device was treated with siloxane prior to any water droplet experiments in order to make it hydrophobic. The resulting contact length between the

water and the device surface was approximately one millimeter. As in the case of the NiCr coil heater, data from the heated water droplets is a direct measure of the relationship between the device output phase modulation and temperature. The theoretical relationship between these two parameters is given in Equation (37). A plot of phase shift per unit temperature for both outputs is given in Figure 29.

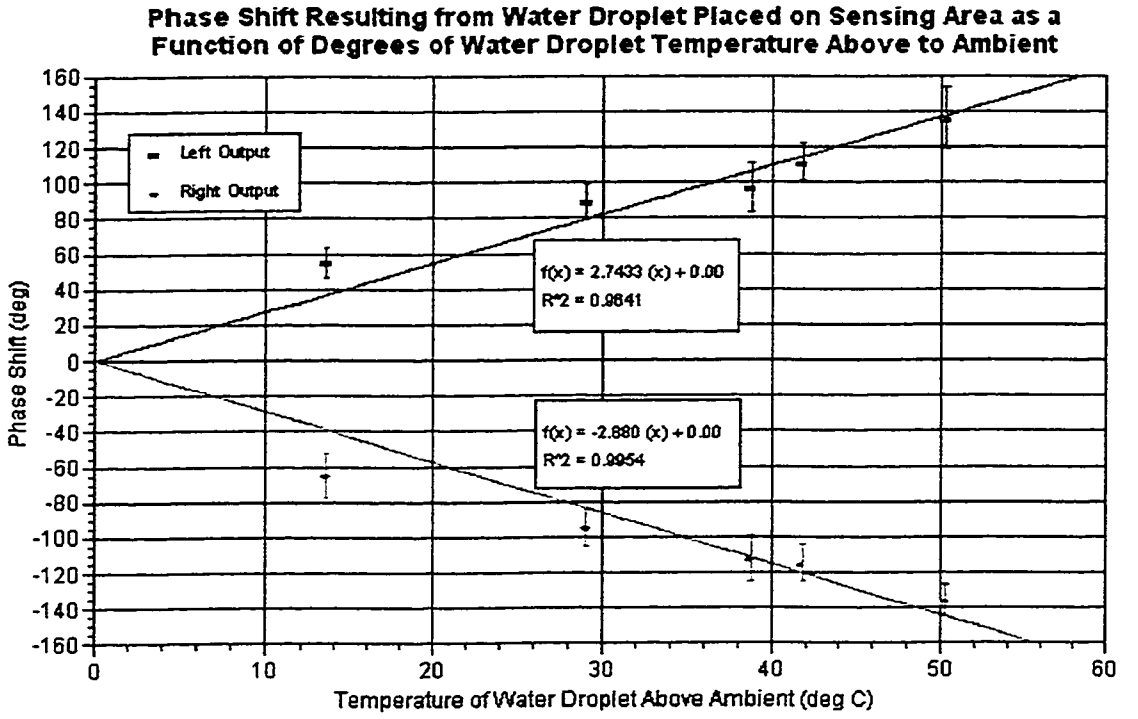

Figure 29. Correlation of phase modulation to temperature increase above ambient of 10 μl water droplet placed on the central sensing arm of the device.

The left output phase modulation $\Delta\Phi_{LO}$ was 2.74 degrees/°C and the right side phase modulation $\Delta\Phi_{RO}$ was –2.88 degrees/°C. In this case the heating length was approximately one millimeter. This corresponds to a length-normalized phase-shift temperature relationship of $\frac{1}{L_l}\frac{\delta\varphi}{\delta T} = 2.74\,\text{deg/°C-mm}$ for the left side output and

$\frac{1}{L_l}\frac{\delta\varphi}{\delta T} = -2.88\,\text{deg}/^{\circ}\text{C-mm}$ for the right. These values show an increase on average of 30% over those measured using the NiCr coil heater. This suggests that the contact length of the water droplet was longer than one millimeter, or the estimate of a three-millimeter heating length in the case of the NiCr coil was too large. It should also be noted that by comparison to the case of the NiCr coil experiments, the magnitude of $\frac{1}{L_l}\frac{\delta\varphi}{\delta T}$ for the right and left outputs in the case of the water droplet experiments are more similar to one another. This is consistent with the hypothesis that heat from the NiCr coil diffused across the device creating an asymmetric phase modulation between the two outputs.

An estimate of device sensitivity can be made using data from the water droplet experiments. One calorie is required to raise the temperature of a gram of water (1 ml) one-degree centigrade. Therefore, 10 mcal are required to raise 10 μl of water one-degree centigrade. Assuming all heat contained in the 10 μl droplet corresponding to temperatures above ambient is transferred to the device, then the data in Figure 27 and Figure 28 show the single output response of this device to varying caloric inputs. From these plots, it can be seen that a water droplet with 135 mcal above ambient heat produces a phase modulation that is a factor of two above the noise level. Using these assumptions, the device shows a minimum resolvable signal of 70 millicalories. This corresponds to detecting 100 mM concentrations of an analyte (in the presence of excess substrate) for a reaction with a heat-of-reaction of 70 kcal/mole.

The estimation of sensitivity above is based on single interferometer outputs and single-reaction chemistry. As in other reports using interferometery for calorimetry [Burgess 1984, Enokihara 1988], this system suffers from environmental noise. Knowing that one degree centigrade is equivalent to 0.01 calorie, the theoretical sensitivity of the current device is 274.33 degrees phase shift per calorie for the left output and –288.04 degrees

phase shift per calorie for the right output (see Figure 29). The advantage of the current device over those previously reported is the ability to discriminate between environmental and measurand signals. The signal-to-noise ratio, and therefore the minimum resolvable signal, should be significantly improved with the incorporation of a differential processing routine applied to signals acquired from both outputs simultaneously. Additionally, for catalytic reactions such as an enzyme assay, the heat released per unit time determines signal levels for calorimetric assays. Heat released per unit time is the product of substrate turnover per second and the heat-of-reaction. This type of sustained reaction will most likely produce a resolvable phase modulation at lower concentrations with the same heats-of-reaction.

COMPARISON TO COMMERCIALLY AVAILABLE CALORIMETERS

Commercially available calorimeters can be divided into two groups, differential scanning calorimeters and isothermal calorimeters. Differential scanning calorimeters use a feedback network to differentially measure heat produced or absorbed by a reference cell and a sample cell. The two cells are incorporated into an adiabatic chamber. Communication with the cells is accomplished through narrow access tubes. The temperature of the two cells and the adiabatic jacket are continually monitored. As heat is generated or absorbed from a chemical reaction in the sample cell, the feedback network is used to add heat to the reference or sample cell so that their temperature difference is zero. The integral of the heat required to maintain this zero thermal differential between the two cells over time is a measure of the total heat resulting from the process being examined. An illustration of this kind of setup is shown in Figure 30A. Differential scanning calorimetry is useful for measuring phase transition properties of lipids, thermodynamic parameters associated with the unfolding of proteins, and the effects of thermodynamic parameters on helix-coil transitions in nucleic acids among other things.

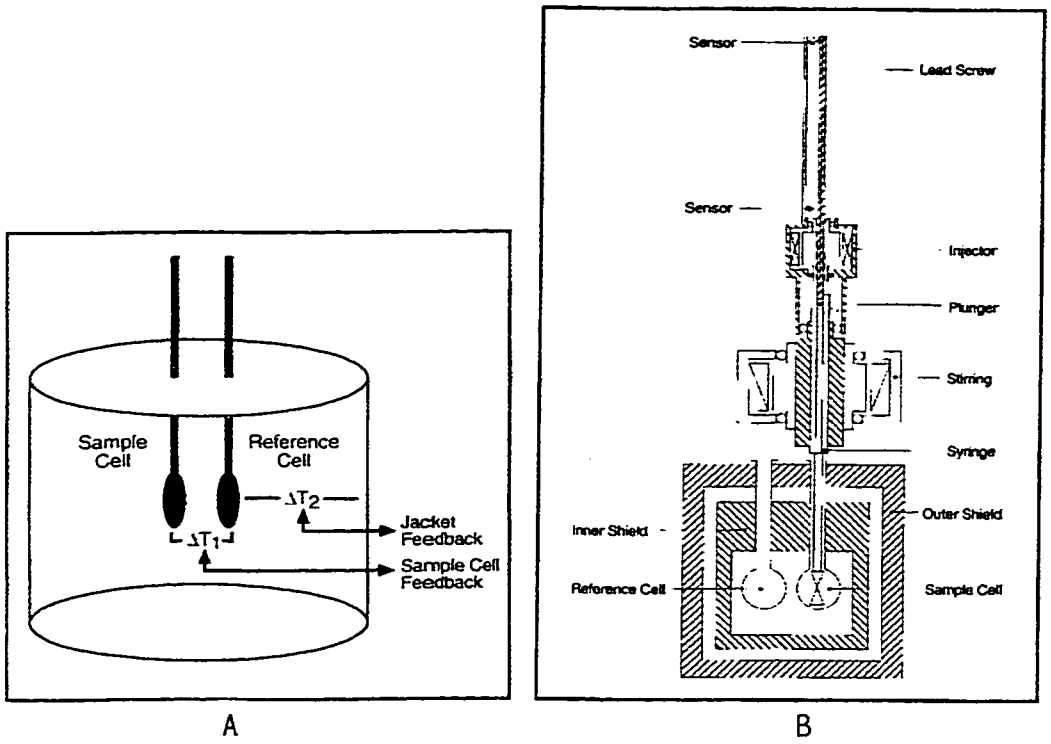

Figure 30. Illustration of commercially available calorimetry chambers. A differential scanning calorimeter chamber is shown on the left *(A)*. An isothermal calorimeter chamber is shown on the right *(B)* (adapted from MicroCal™ product literature).

The device described in this work is an isothermal calorimeter. Isothermal calorimetry involves measuring the heat absorption/emission from a chemical reaction initiated by the addition of a binding component. Absolute temperature measurements are made from a sample cell contained within a thermally insulated chamber. Measurement of this heat allows an accurate determination of binding constants, reaction stoichiometry, enthalpy, and entropy. Figure 30B illustrates an example isothermal calorimetry chamber. The syringe containing a ligand solution is titrated into the sample cell containing a solution of the substrate molecule at a constant temperature. As the two solutions mix, heat is

released in direct proportion to the binding that occurs. As the substrate receptor sites become saturated with added ligand, the heat produced diminished until only background dilution heat is observed. Applications of isothermal calorimetry include binding activity studies, reaction kinetics studies, enzyme and metabolite assays, reaction enthalpy measurements and others.

Three leading calorimeter manufactures, MicroCal ™ Incorporated (Northhampton, MA), Calorimetric Sciences Corporation (Provo, UT), and Thermometric Limited (Stockholm, Sweden) were evaluated for this comparison. Product information from these companies was obtained from their respective web sites [Web Address 1, Web Address 2, Web Address 3] or personal conversations with sales representatives. Current technology in calorimetry uses a large thermal mass (usually water) to keep the temperature of the sample cell constant. Measurement of heat absorption or liberation is determined by measuring the heat necessary to keep the sample cell at a constant temperature. The use of a water bath in these calorimeters results in a large footprint and a weight. The physical size of the instruments evaluated were approximately 18 in^3 and weighed between 45 – 85 lbs. (empty). Reported sensitivity for these devices ranged between 0.1 μcal and 1.0 millicalories. Prices ranged from $26,400.00 to $69,500.00.

The sensing chip described in this work is approximately 1.5" x 0.5" x 0.1" and weighs less than one ounce and has a single output signal resolution of 70 millicalories. Advantages of the current device over commercially available instruments include size, portability, simple sample delivery, and cost. The size and weight of the current device provides the potential for use as both a bench-top system as well as a field instrument. If light were delivered to the device through a fiber, a system could even be developed for remote sensing.

Simple sample delivery in the current device provides another advantage. Since commercially available instruments depend on thermally insulated or adiabatic chambers, sample delivery into these chambers becomes somewhat restricted. The current device

depends on a signal processing routine to exclude thermal noise and thus permits easy access to the sensing area. Liquid samples can be placed directly on the sensing area with the aid of an infusion pump if very accurate time and volumes are required. Gas or liquid samples can be monitored directly in the environment if specific substrate receptor molecules are anchored to the sensing area. Additionally, if several different ligand-specific substrate molecules are each anchored to a different device, a single sample containing several ligands can be evaluated. In this situation, a bank of devices each sensitive to a specific ligand-chemistry would be incorporated into a custom flow cell. A single sample is then passed over all the devices.

Another obvious advantage of the current device is price. Table 6 outlines the development costs for this device.

Table 6. Cost Estimate for Device Development

Item	Cost
Photolithographic Mask	$700.00
Fabrication of Prototype Device	$250.00
Gas HeNe Laser	$1000.00
Two Linear Array Detectors Including Electronics	$1000.00
LabVIEW™ Software Development Platform	$1000.00
Laptop Computer	$1500.00
Data Acquisition Card and Cables	$770.00
Miscellaneous Optical Components	$1500.00
Total Cost	**$7720.00**

This estimate is based on the device prototype fabrication cost, which would go down if the design were frozen and several devices were made. This cost estimate also includes $1,700.00 of nonrecurring costs for the photolithographic mask and the LabVIEW™

development platform. In addition, if all components of the device were integrated and prealigned, the $1,500.00 of miscellaneous optical components would not be necessary. Further reductions in cost could be realized if a diode laser and a fiber pigtail were used to launch light. Considering all this information, it is conceivable that this device could be developed into an instrument for around $5,000.00, significantly less than currently available commercial instruments. Since standard semiconductor processing techniques are used in manufacturing, costs can be reduced even further. (Several devices can be manufactured in a single run on a single wafer and performance can be expected to be identical.) While the device is not as sensitive as those commercially available, it is believed that modifications can be made to improve sensitivity (see *Future Work*).

CHAPTER 5: SUMMARY, CONCLUSIONS AND FUTURE WORK

SUMMARY DISCUSSION

A novel integrated optical calorimeter has been presented. The device has been designed with two interferometric outputs. The phase modulation response of these two outputs permit the discrimination between environmental and measurand perturbations. Design calculations for the device layout and individual components of the waveguides are presented. A computer algorithm was written to interpolatively up-sample the raw data providing better resolution. A computer algorithm was also written to calculate the cross correlation between each individual spectrum and a base line spectrum. The cross correlation routine was used to determine output phase modulation. The signal processing routine was discussed and the computer source code written for the project provided as appendices. A nichrome wire coil was used as a heater to evaluate the consistency of device performance with predictions from theory. The nichrome heater was also used to provide an initial measure of device response to temperature change occurring at the sensing area of the device. In an effort to model a chemical reaction, water droplets of known volume and temperature were placed on the sensing area while monitoring the interferometric outputs for phase modulation. This second series of experiments was carried out to provide an initial measure of device response to heat, but further work should be done to determine the heat capacity of the device. Experimental results from the second series of experiments are presented.

The device layout was designed so that two Mach-Zehnder interferometers sharing a central sensing arm produce two outputs. The two outputs produced unidirectional phase modulation for environmental thermal gradients and directionally opposed phase modulation for measurand thermal signals. The waveguides had square cross-sectional

profiles. A 2.0 μm waveguide width was fabricated to produce single mode operation at a wavelength of 632.8 nm. The waveguides in the device were composed of three individual structures: S-shaped bends, a power splitter, and two directional couplers (-6.20 dB and -4.81 dB). Design calculations for these structures were carried out using a technique based on a set of normalized parameters [Rasmussen 1994a, Rasmussen 1994b]. The S-bends in the directional couplers were 5,278.1 μm long with a 2,258.1 μm minimum radius of curvature. The S-bends in the power splitter were 11,880.6 μm long with a 6,021.6 μm minimum radius of curvature. The –6.20 dB coupler was 195.2 μm long. The –4.81 dB coupler was 297.9 μm long. A 2.0 μm wall-to-wall separation between waveguides was used for both directional couplers. The overall dimension of the device is 4.3 cm long by 1.2 cm wide. Design calculations were sent to Photonic Integration Research Inc. (Columbus, OH) for fabrication using a process of flame hydrolysis and reactive ion etching.

Interferograms collected from the device produced spectra with 30-40 points/fringe which corresponded to about 10° of phase/point. In an effort to improve the resolution of the data, an up-sampling interpolation routine was developed. Spectra were up-sampled by a factor of 10 increasing signal resolution to approximately 1° of phase/point. Phase modulation of output signals were determined using a cross-correlation routine. An algorithm was developed to compute the auto-correlation of a baseline spectrum, and the cross-correlation of each individual spectrum with a baseline spectrum. Knowing the number of degrees represented by each point, the location of each cross-correlation peak relative to the auto-correlation peak provided a measure of phase modulation. Results from the cross-correlation analysis routine were compared with that of a fast Fourier transform routine and a simple peak-to-peak measurement. Results showed phase modulation calculations to be within ± 1° of these other methods.

A nichrome wire was configured into a coil 3 mm long and 2 mm in diameter. The coil was connected to a voltage power supply with a programmable current setting. The coil was brought into contact with the surface of the device's sensing area and used as a point source heater. Thermal perturbations at the sensing arm of the device caused positive phase modulation in the left output interferogram and negative phase modulation in the right output interferogram. The coil heater was placed above the reference arm of the right side interferometer simulating a thermal gradient across the device. A positive phase modulation was observed in the right output interferogram while heating the reference arm (relative to the sensing arm). These phase modulation results were consistent with theoretical predictions.

Experiments were also carried out using the coil heater to characterize the device-phase-response to temperature. Surface temperature was determined by placing a foil thermocouple on the device adjacent to the coil. The length normalized phase response of the left output was 1.98 deg/° C-mm and -1.63 deg/° C-mm for the right.

Another series of experiments was carried out as an initial measure of the device phase response to heat. Deionized water was heated in a heater block to a known temperature. A 10 μl droplet was then placed on the surface of the device at the sensing area while monitoring interferometric output. The water droplet temperature on the surface was determined *a priori* by placing a 10 μl droplet on a foil thermocouple located on the device. Calculations of phase modulation as a function of temperature from these experiments resulted in 2.74 deg/° C-mm from the left output and -2.88 deg/° C-mm from the right output. This corresponds to a phase modulation of 274.33 deg/calorie from the left output and 288.04 deg/calorie for the right.

FUTURE WORK

DESIGN CONSIDERATIONS

There are three issues worthy of consideration for future design-development of this device. They are: further consideration of single mode operation, separation of the two outputs for simultaneous monitoring, and a longer sensing arm. (Integration of beam launch and signal detection might be considered a design-development issue, but it will be considered in the following section under *Increasing Signal-to-Noise Ratio.*) Each of the three issues mentioned is discussed below.

Close evaluation of raw data spectra (see Figure 18) suggests that a small amount of optical power in these waveguides may be propagating in a second order mode. The possibility of this is further strengthened by the fact that the thermal conductivity of silica (waveguide material) and silicon (substrate material) differs by two orders of magnitude [Musikant 1985, CRC Press 1988]. During the fabrication process the deposited silica is annealed at 1250 °C. The large difference in thermal conductivity of the two materials may create a stress-induced birefringence in the waveguides during cooling. It is also possible that the core width is too wide for single mode operation. The design specification was for a 2 μm core width, but the manufacturer could only hold tolerances to ± 0.5 μm. If the devices were manufactured on a glass or quartz substrate the possibility of birefringence would be eliminated. If the core-cladding index differential is reduced from its current value of 0.69 %, then the core width could be larger and still maintain single mode operation (see Equation 15). Alternatively, if the core width remained the same, a longer wavelength of light could be used to assure single mode operation. Implementing these design changes would eliminate any possibility of propagating higher order modes.

In the current work, each interferometric output was monitored separately. In order to take full advantage of the device design, both interferograms must to be monitored

simultaneously. The bulk-optics steering setup currently used requires a microscope tube at the device output. The two device outputs have a 1 cm separation distance. It is not possible to bring two microscope tubes together with a 1 cm center-to-center separation distance. Signal detection would be significantly improved if the device design were modified to increase the output separation distance thereby allowing detection of both outputs simultaneously.

The results of the device-phase-response to temperature reported were normalized to length. If the device were designed to incorporate a longer sensing arm, signal resolution would increase proportionally. In this case, a sample well would need to be added permitting use of small samples while confining their thermal perturbations to the longer sensing arm of the waveguide.

INCREASING SIGNAL-TO-NOISE RATIO

Every attempt to use interferometery for calorimetry has suffered from environmental noise. The current effort has the advantage of distinguishing environmental thermal signals from that of the measurand, however, there are other noise signals that should also be reduced. Three suggestions are presented and discussed below to reduce the overall noise observed in the output signals.

The results presented in this work are from single interferometric outputs of the device. The device was designed to eliminate unwanted thermal perturbations from the environment using both output signals. Proof of this operational principle has been presented, but its advantage has not yet been exploited. A signal processing routine should be developed to eliminate thermal signals from the environment. This task will require making modifications so that both outputs can be monitored simultaneously. Modifications, which allow a simulated thermal gradient to be impressed across the device, will also need to be made. Previous attempts to characterize thermal gradient response suffered because thermal expansion of the device during heating caused

misalignment of the optical system. This suggests that the input source and detection system should be mechanically linked to the device.

Data collected during the current work were from a system setup on an optics table that did not incorporate an air suspension system. Vibrations from walking close to the table could be seen to effect the output interferograms. After optical beams exited the waveguides, they traveled through 1-2 meters of free space and encountered six optical components. Irregularities in these components and their vibrations added additional noise to the monitored signal. Linking the optical source and detection system to the device will reduce the impact of mechanical noise on the system. The source could be coupled to the device by adding an optical fiber pigtail to the input waveguide. If it was properly aligned and mode-matched to the device, a semiconductor laser would provide adequate power for device operation.

Linking the detection system to the device could be accomplished by redesigning the device to have a greater separation distance between the two waveguide-outputs that form each interferogram and mounting a detector in front of each output. If a beam is traveling in a waveguide with core index n_1, cladding index n_2, and exits the guide into a medium (air) of refractive index n_0, the numerical aperture (NA) defines the relationship between the divergence angle of the beam and the three refractive indices The relationship is given by

$$NA = n_0 \sin\theta_d = (n_1^2 - n_2^2) \tag{43}$$

where θ_d is the divergence angle of the beam as it exits the waveguide. Figure 31 shows two waveguides (one interferometric output) from the device as the beams exit the

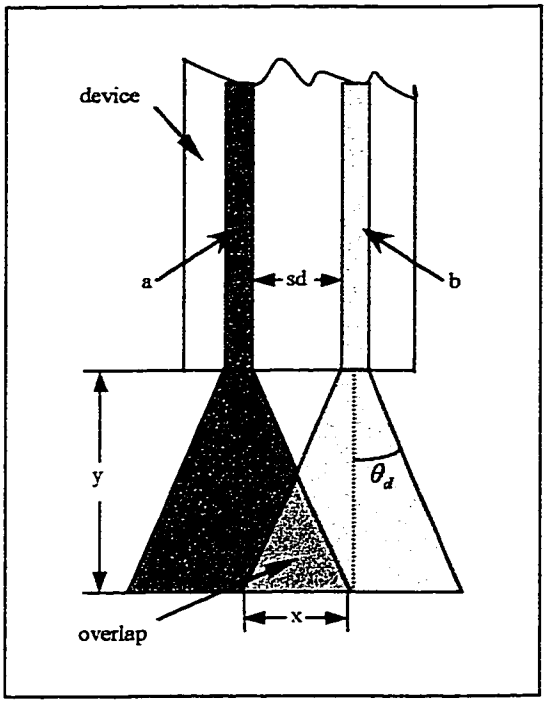

Figure 31. Divergence of optical beams from one side of the device: *a*, *b* waveguides, θ_d divergence angle, *sd* separation distance. Interferogram detected in area of overlap.

waveguides. The area of overlap shown is where an interferogram would be observed. Future design modifications should be made so that the separation distance (*sd*) corresponds to an overlap length (*x*) that is equal to the length of a linear array detector. Having made this change, array detectors could be aligned and mounted directly in front of the device, and interferograms detected without the need for external steering optics. The most significant advantage of this approach would be the elimination of all the residual noise in the signal associated with vibration and irregularities of external optical components currently used. It would also provide integration of the optical detection system, eliminate the need for microscope tubes, and allow detection from both outputs, thus eliminating the design changes suggested above for simultaneously detecting signals from each output of the device.

A final suggestion to increase the signal to noise ratio involves isolating the device from air currents. This can be accomplished by simply enclosing the entire system in a box. In this case a bulkhead fitting could be incorporated into the enclosure with a small fixed tube aligned to deliver samples to the sensing area. Available sample-volume and system dead-volume would need to be considered if this modification were incorporated. A custom-mounting block could be fabricated to hold the semiconductor laser on one side, the two detectors on the other and the device in the middle. A box 6"x12"x8" would enclose the entire system, if the source and detectors were coupled to the device using such a mounting block. Implementing these suggestions will significantly reduce noise observed in the data and provide greater sensitivity of the device-phase-response.

BIBLIOGRAPHY

Accornero, R., Artiglia, M., Coppa, G., Di Vita, P., Lapenta, G., Potenza, M., and Ravetto, P., **Finite difference methods for the analysis of integrated optical waveguides,** Electron. Lett., Vol. 26, 1959-1960, 1990.

Barbarossa, G. and Laybourn, P. J. R., **Vertically integrated high-silica channel waveguides on Si,** Electron. Lett., Vol. 28, No, 5, 1992, 437-438.

Bataillard, P, Steffgen, E., Haemmerli, S., Manz, A., and Widmer, H. M., **An integrated silicon thermopile as biosensor for the thermal monitoring of glucose, urea and penicillin,** Biosensors and Bioelectronics, Vol. 8, 1993, 89-98.

Boiarski, A. A., Busch, J. R., Bhullar, B. S., Ridgway, R. W., Wood, V. E., **Integrated-optic sensor with macro-flow cell,** SPIE, Vol. 1793, 1992, 199-211.

Boiarski, A. A., Ridgway, R. W., Busch, J. R., Turhan-Sayan, G., and Miller, L. S., **Integrated optic biosensor for environmental monitoring,** SPIE, Vol. 1587, 1991, 114-128.

Brandenberg, A, Edelhauser, R., Hutter, F., **Gas sensor based on integrated optical interferometer,** SPIE, Vol. 1510, 1991, 148-159.

Burgess, L. W. Jr., **A Fiberoptic Interferometer for Enthalpimetric Measurements in a Flowing Stream,** *Dissertation,* Virginia Polytechnic Institute and State University, Blacksburg, Virginia, 1984.

Burgess, L. W., **Overview of planar waveguide techniques for chemical sensing,** SPIE, Vol. 1368, 1990, 224-229.

Cassidy, S. A., MacKenzie, F., Beaumont, C. J., Maxwell, G. D., Ainslie, B. J., Nield, M., Jones, C. A., Enokihara, A., Masayuki, I., and Sueta, T., **Integrated-optic fluid sensor using heat transfer,** Appl. Opt., Vol. 27, No. 1, 1988, 109-113.

CRC Press, Inc., ***CRC Handbook of Physics and Chemistry,*** Boca Raton, FL, 70th Ed., 1988.

Feit, M. D. and Fleck, J. A., **Light propagation in graded-index optical fibers,** Appl. Opt., Vol. 17, 1978, 3990-3998.

Findakly, T., **Glass waveguides by ion exchange: a review,** Optical Eng. Vol. 24, No. 2, 1985, 244-269.

Godell, J. E., **A circular-harmonic computer analysis of rectangular dielectric waveguides,** Bell Syst. Techn. J., Vol. 48, 1969, 2133-2160.

Hanabusa, M. and Fukuda, Y., **Single-step fabrication of ridge type glass optical waveguides by laser chemical vapor deposition**, Appl. Opt., Vol. 28, 1989, 11-12.

Hecht, E. and Zajac, A., ***Optics,*** Reading, Massachusetts, Addison-Wesley, 1979.

Heideman, R. G., Kooyman, R. P. H., and Greve, J., **Development of an optical waveguide interferometric immunosensor,** Sensors and Actuators, Vol. B4, 1991, 297-299.

Hemminger, W. and Hohne, G., ***Calorimetry Fundamental and Practice,*** Deerfield Beach, Florida, Verlag Chemie,1984.

Henry, C. H. and Shani, Y., **Analysis of mode propagation in optical waveguide devices by Fourier expansion,** IEEE Quantum Electron., Vol. 27, 1991, 523-530.

Hocker, G. B., **Fiber-optic sensing of pressure and temperature,** App. Opt., Vol. 18, No. 9, 1979, 1445-1448.

Izawa, T., and Kakagome, H., **Silver ion-exchanged glass waveguides,** Appl. Phys. Lett., Vol. 21, 1972, 584-586.

Kawachi, M., **Silica waveguides on silicon and their application to integrated-optic components,** Opt. Quant. Electron, Vol. 22, 1990, 391-416.

Kawachi, M., Yasu, M., Edahiro, T., **Fabrication of SiO_2 – TiO_2 glass planar optical waveguides by flame hydrolysis deposition,** Electron. Lett., Vol. 19, 1983, 583-584.

Kobayashi, Soichi, Ph.D., Photonic Integration Research, Inc., Columbus, OH., **personal discussion,** February 2, 1996.

Kobayashi, S., **Recent development on silica waveguide technology for integrated optics,** SPIE, Vol. 2997, 1997, 264-270.

LabVIEW Analysis VI Reference Manual, Austin, TX, National Instruments, 1996.

Loebel, N. G., **Singlemode Fiber Interferometric Biosensors,** *Dissertation,* University of Washington, Seattle, Washington, 1998.

Lukosz, W. and Stamm, C. H., **Integrated optical interferometer as relative humidity sensor and differential refractometer,** Sensors and Actuators, Vol. A25-A27, 1991, 185-188.

Marcatili, E. A. J., **Bends in optical dielectric guides,** Bell Syst. Techn. J., Vol. 48, 1969a, 2103-2132.

Marcatili, E. A. J, **Dielectric rectangular waveguide and directional coupler for integrated optics,** Bell Syst. Techn. J., Vol. 48, 1969b, 2071-2102.

Miller, S. E., **Integrated optics: An introduction,** Bell Sys. Tech. J., Vol. 48, No. 7, 1969, 2059-2069.

Miyashita, T., Sumida, S. and Sakaguchi, S., **Integrated optical devices based on silica waveguide technologies,** SPIE, Vol. 993, 1988, 288-294.

Muehlbauer, M. J. Giuilbeau, E. J. and Towe, B. C., **Model for a thermoelectric enzyme glucose sensor,** Anal. Chem., Vol. 61, 1989, 77-83.

Muehlbauer, M. J. Giuilbeau, E. J. and Towe, B. C., **Applications and stability of a thermoelectric enzyme sensor,** Sensors and Actuators, Vol. B2, 1990, 223-232.

Musikant, S., ***Optical Materials: An Introduction to Selection and Application,*** New York, New York, Marcel Dekker, Inc., 1985.

Najafi, S. I. (editor), ***Introduction to Glass Integrated Optics,*** Norwood, Massachusetts, Artech House, 1992.

Oetken, G., Parks, T. W. and Schussler, H. W., **New results in the design of digital interpolators,** IEEE Trans. Acoustics Speech, Sig. Process., Vol. ASSP-23, No. 3, 1975.

Poszner, T., Schreiter, G., Muller, R., **Stripe waveguides with matched refractive index profiles fabricated by ion exchange in glass,** J. Appl. Phys., Vol. 70, No. 4, 1991, 1966-1974.

Ramaswamy, R. V. and Srivastava, R., **Ion-exchanged glass waveguides: A review,** J. Lightwave Technol., Vol. 6, No. 6, June 1988a, 984-1001.

Ramaswamy, R. V., Cheng, H. C., and Srivastava, R., **Process optimization of buried Ag^+ -Na^+ ion-exchanged waveguides: theory and experiment,** Appl. Opt., Vol. 27, No. 9, 1988b, 1814-1819.

Rasmussen, T., Bjarklev, A., Lester, C. and Geltzer, P. G., **Normalized parameters for integrated optical waveguide components,** SPIE, Vol. 2212, 1994a, 268-274.

Rasmussen, T, and Bjarklev, A., **Scaling laws for integrated optics waveguides,** Appl. Opt., Vol. 33, No. 15, 1994b, 3231-3236.

Rasmussen, T., Povlsen, J. H. and Bjarklev, A., **Accurate finite difference beam propagation method for complex integrated optical structures,** IEEE Photonics Technol. Lett., Vol. 5, 1993, 339-342.

Riou, O., Gandit, P., Charalambous, M., and Chaussy, J., **A very sensitive microcalorimetry technique for measuring specific heat of μg single crystals,** Rev. Sci. Instrum., Vol. 68, No. 3, 1997, 1501-1509.

Rohsenow, W. M. and Heartnett, J. P., ***Handbook of Heat Transfer,*** New York, New York, McGraw-Hill, 1973.

Rush, J. D. and Thurlow, A, **Wavelength and time multiplexing devices on planar silica motherboards,** Brit. Telecom, Technol. J., Vol. 11, 1993, 137-148.

Saad, S. M., **Review of numerical methods for the analysis of arbitrary shaped microwave and optical dielectric waveguides,** IEEE Trans. Microwave Theory Tech., Vol. MTT-33, 1985, 894-899.

Schafer, R. W. and Rabiner, L. R. **A digital signal processing approach to interpolation,** Proc. IEEE, Vol. 61, No. 6, 1973.

Schlosser, W. and Unger, H. G., **Partially filled waveguides and surface waveguides of rectangular cross section,** *Advances in Microwaves*, New York: Academic Press 1966, 319-387.

Senior, J. M., ***Optical Fiber Communications,*** London, England, Prentice-Hall, 1985.

Takato, N, Sugita, A., **Silica based single mode waveguides and their applications to integrated-optic devices,** Mat. Res. Soc. Symp. Proc., Vol. 172, 1990, 253-264.

Tsutsumi, K., Imada, Y., Hirai, H. and Yuba, Y., **Analysis of single-mode optical Y-junctions by the bounded step and bend approximation,** J. Lightwave Technol., Vol. 6, No. 4, 1988, 590-600.

Vaidyanathan, P. P., ***Multirate Systems and Filter Banks,*** Englewook Cliffs, NJ, Prentice-Hall, 1993.

Walker, R. G. and Wilkinson, C. D. W., **Integrated optical waveguiding structures made by silver ion-exchanged in glass. 1: The propagation characteristics of stripe ion-exchanged waveguides; a theoretical and experimental investigation,** Appl. Opt., Vol. 22, No. 12, 1983a, 1923-1928.

Walker, R. G. and Wilkinson, C. D. W., **Integrated optical waveguiding structures made by silver ion-exchange in glass. 2:Directional coupler and bends,** Appl. Opt., Vol. 22, No. 12, 1983b, 1929-1935.

Web Address 1, **http://www.microcalorimetry.com**, 1999

Web Address 2, **http://www.calscorp.com**, 1999.

Web Address 3, **http://thermometric.com/**, 1999

Yajima, H., **Coupled mode analysis of dielectric planar branching waveguides,** IEEE J. Quantum Electron., QE4, 1978, 749-755.

Yajima, H., **Coupled mode analysis of dielectric planar branching waveguides,** IEEE J. Quantum Electron., Vol. QE-14, No. 10, 1978, 749-755.

APPENDIX A: ION DIFFUSION FABRICATION EFFORT

The first ion-exchanged waveguide fabrication was reported in 1972 [Izawa 1972]. As stated in the text, Najafi has written an excellent overview of ion exchange integrated optics [Najafi 1992]. The ion-exchange process involves replacing an ion in glass (usually Na^+) with an ion larger in size or one of higher polarizablity like Ag^+, K^+, Cs^+, or Tl^+. As a result, the refractive index of the ion-exchanged glass is increased locally creating a waveguide. The ion-exchange process can be carried out thermally (diffusion driven) or accelerated with the aid of an electric field. In the thermal ion-exchange process, a molten salt serves as the ion source. In an electric field assisted process, a thin metallic film serves as the ion source.

The specific application and design specifications of any particular device will determine if an ion-exchange process is suitable for waveguide fabrication. Characteristics of waveguides fabricated using an ion-exchange process include:

- Waveguide fabrication is relatively easy to carry out, however it requires good control over the physics and chemistry of the process to achieve reproducibility of waveguides with accurate dimensions and shape.
- It is very difficult to fabricate waveguides with reasonably similar dimensions in all directions.
- Planar (as opposed to channel) waveguide configurations can be fabricated.
- Channel waveguides can be fabricated which can be matched to conventional optical fibers.

- Waveguides have a graded (not step) index profile.
- Light can be coupled into and out of waveguides using prisms or etched gratings
- Waveguides are at the surface of the substrate (unless buried).
- Waveguide dimensions are limited by achievable resolution of lithography techniques.
- Characterization of propagation losses, effective index, mode profile, and transmission spectrum can be carried out with relative ease.

Some of the characteristics listed above can be viewed as either an advantage or as a disadvantage depending on the application of a particular waveguide structure. For example, waveguides fabricated with ion-exchange techniques are at the surface of the substrate. This feature may be advantageous if access to the guided optical power is desired at the surface. However, it also results in scattering losses associated with surface roughness.

An effort was made to fabricate the devices described in this work using ion diffusion techniques. A photolithographic mask was made with the pattern shown in Figure A1.

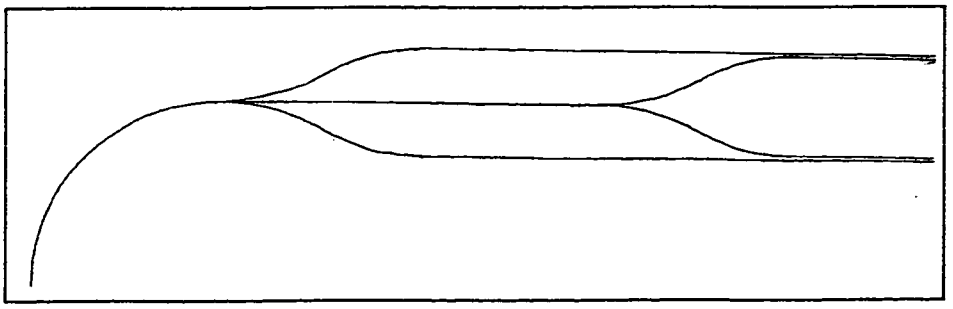

Figure A1. Photolithographic mask pattern for ion diffused device

A two and one-half inch diameter wafer made from BK-7 glass had 1250 angstroms of aluminum evaporated onto its surface. Photoresist was spun onto the aluminum. The photomask was then used to polymerize all photoresist except where a waveguide was desired. The unexposed resist was washed away to expose the aluminum underneath. This technique proved unsatisfactory because the power splitter regions in the waveguide pattern (junctions where one waveguide splits into multiple waveguides) washed out into large undefined triangles in the pattern.

A second attempt at the lithography process was made employing a technique know as liftoff. In this case the glass wafers were first coated with photoresist. A reverse mask used to expose the photoresist covering those regions where a waveguide was desired. The unexposed resist was washed away exposing the wafer underneath. Then 1250 angstroms of aluminum was evaporated onto the wafer and the waveguide patterned in photoresist on the wafer's surface. The resist in the pattern of the waveguides (still remaining on the surface of the wafer) was washed away lifting off the aluminum in these regions. This technique resulted in successfully masking the BK-7 wafer with aluminum everywhere except over regions where waveguides were desired. As stated above, the waveguide dimensions are limited by achievable resolution of lithography techniques. The design specification was to have single mode waveguides operating at 632.8 nm. This specification required waveguide mask apertures to be 5 μm or smaller. The liftoff technique described produced waveguide pattern apertures 3.9 μm wide.

A silver nitrate salt melt was the ion source in this exchange process. Silver ions (Ag^+) from the melt were exchanged for sodium ions (Na^+) in the glass. This increased the local refractive index of the exchanged glass and formed a guiding structure. When aluminum is used as a diffusion mask in silver-sodium exchange, silver ions tend to be reduced to metallic silver at the boundary of the aluminum mask. This increases the absorption losses of the waveguide. The aluminum mask can be anodized to minimize this effect.

The process described by Walker was used to anodize the aluminum mask in this work [Walker 1983a]. The wafer with the aluminum mask on it was used as an anode in an electrolytic cell containing 20% sulfuric acid at 0° C. A voltage of 15V was applied between the anode and an aluminum cathode plate. This caused SO_4^{2-} ions to migrate to the anode and chemically combine with it forming a hard adherent oxide coating. In this process, the oxidation rate decays with distance from the current source and occurs very rapidly at the liquid surface interface. This effect caused premature isolation of the submerged metal mask. To combat this problem, a photoresist mask was used on the aluminum to provide a protected current path past the electrolyte surface. Progression of the anodization process was evaluated by monitoring current flow. When current flow between the anode and the cathode abruptly dropped to zero the process was complete. After being anodized the wafers were rinsed in water and soaked in acetone to prevent hydration and dissolution of the oxide layer.

The ion source for the exchange process was a salt melt composite comprised of a 10^{-4} mole fraction of silver nitrate ($AgNO_3$) in sodium nitrate ($NaNO_3$). Ion diffusion was carried out at 330 °C for 60 minutes. Following ion-exchange, the wafers were cooled, cleaned and diced for optical testing.

The resulting waveguides from the process described are shown in Figure A2. The penny shown in the top photograph is for purposes of scale. Light from a HeNe laser (λ=632.8 nm) was launched into the device by end firing at point *A* shown in the lower left photograph. The light can be seen to have traveled through a single guide, into a power splitter, and out into two separate guides. These photographs were taken with a Polaroid camera positioned above the guide. Waveguides can be seen as a result of light scattered out of the waveguides at the surface of the chip. The waveguides disappear from view because the surface scattering and bending losses removed all optical power traveling in the guides.

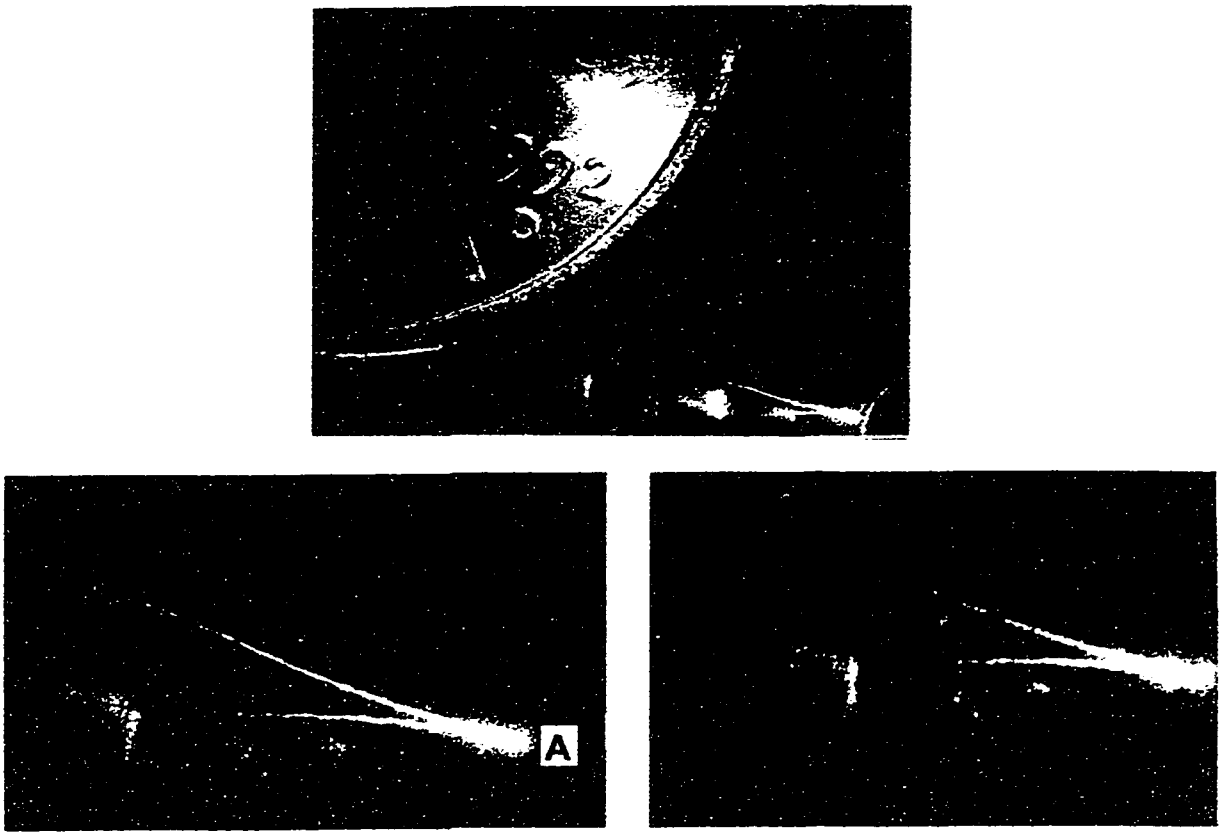

Figure A2. Resulting waveguides from ion-exchange fabrication process

Attempts to detect light at the output of the device were unsuccessful. Further efforts were made to improve the performance of waveguides fabricated using ion diffusion, but without success. Ultimately, this fabrication technique was abandoned. A new device layout design was adopted and individual component design-calculations made. These new design specifications were delivered to Photonics Integration Research Incorporated (Columbus, OH) for device fabrication using flame hydrolysis and reactive ion etching techniques. Details are provided in the text.

APPENDIX B: SCAN AND LOG DATA ROUTINE – USER INTERFACE AND SOURCE CODE

Scan and Log Data Routine: User Interface

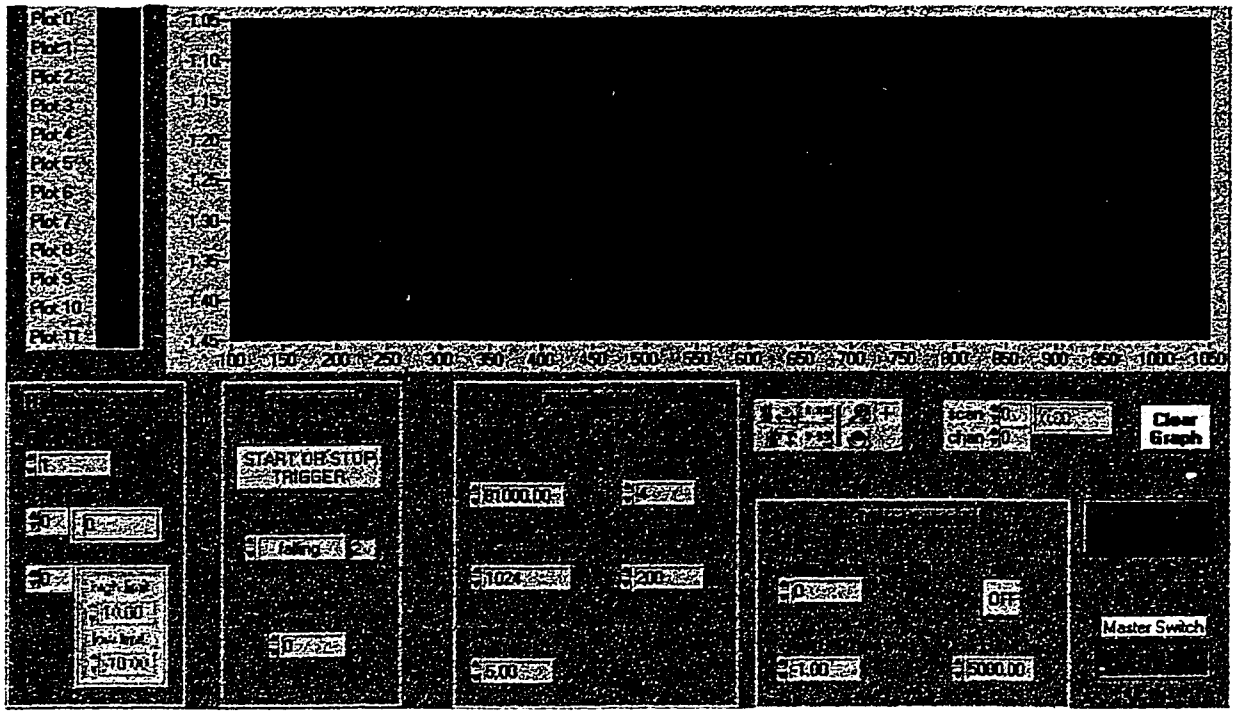

Scan and Log Data Routine: Source Code

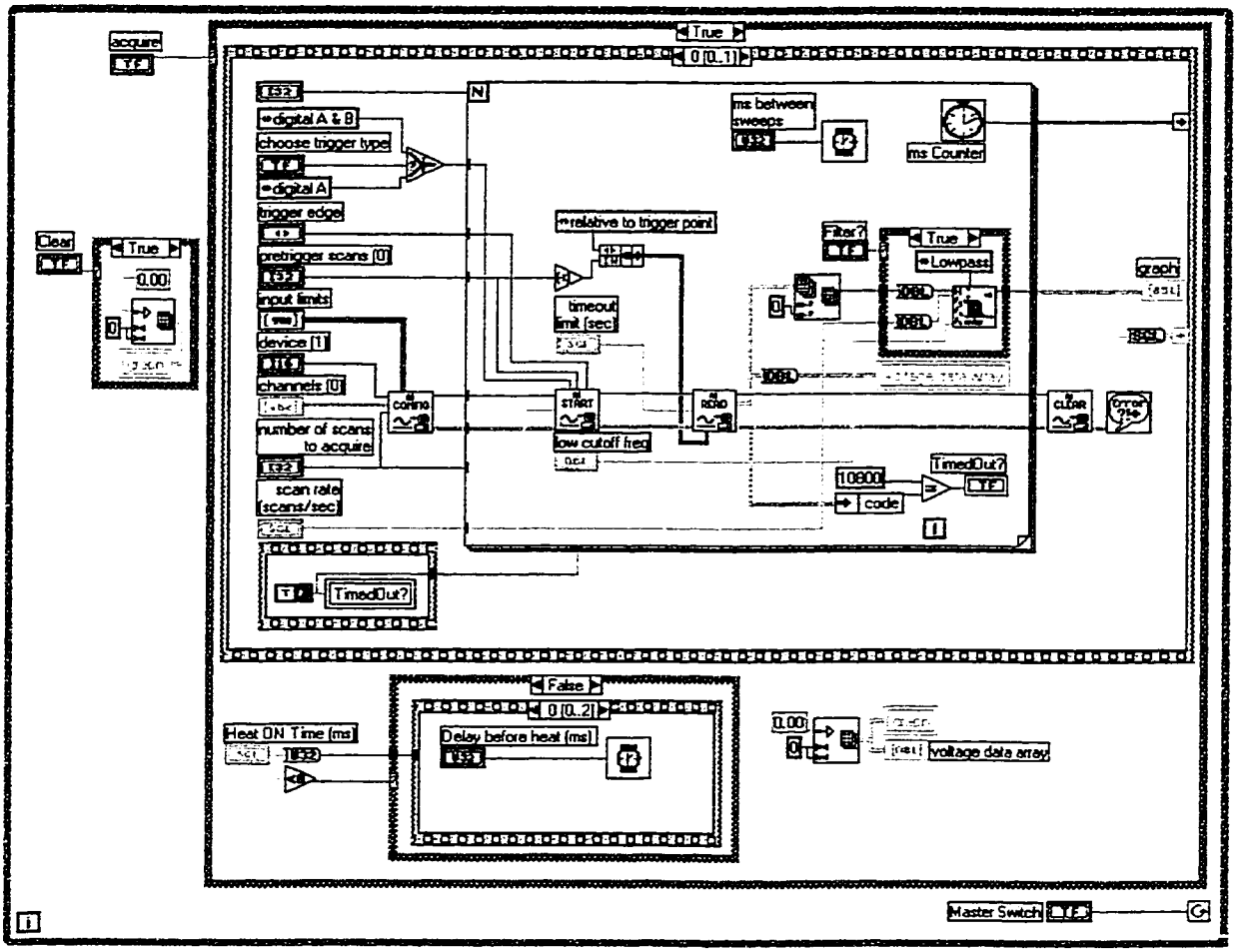

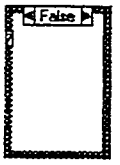

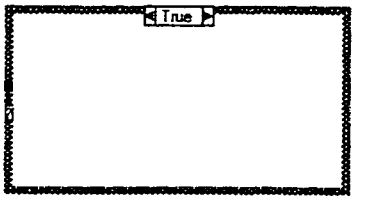

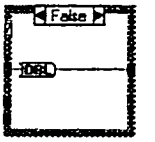

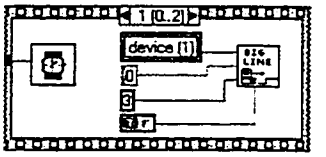

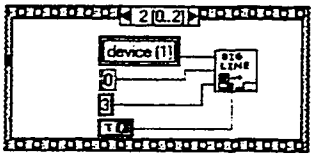
2 [0..2]
device (11)
BIG LIME
0
3

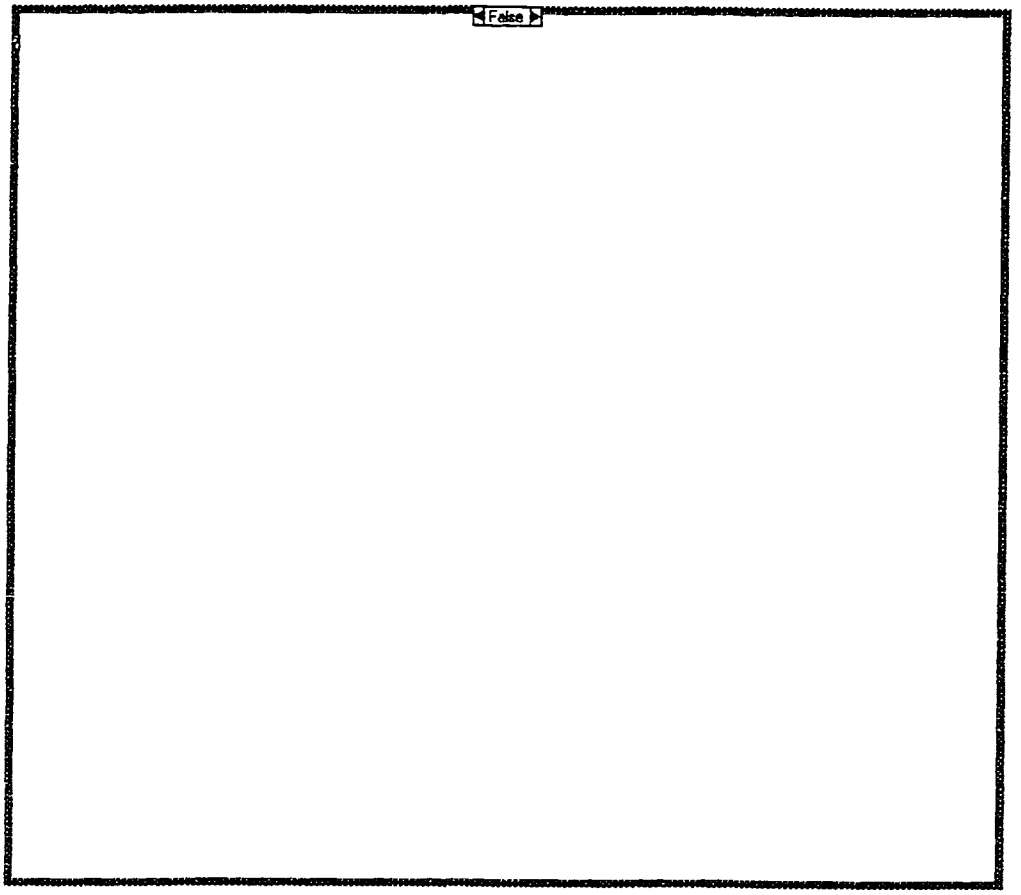
False

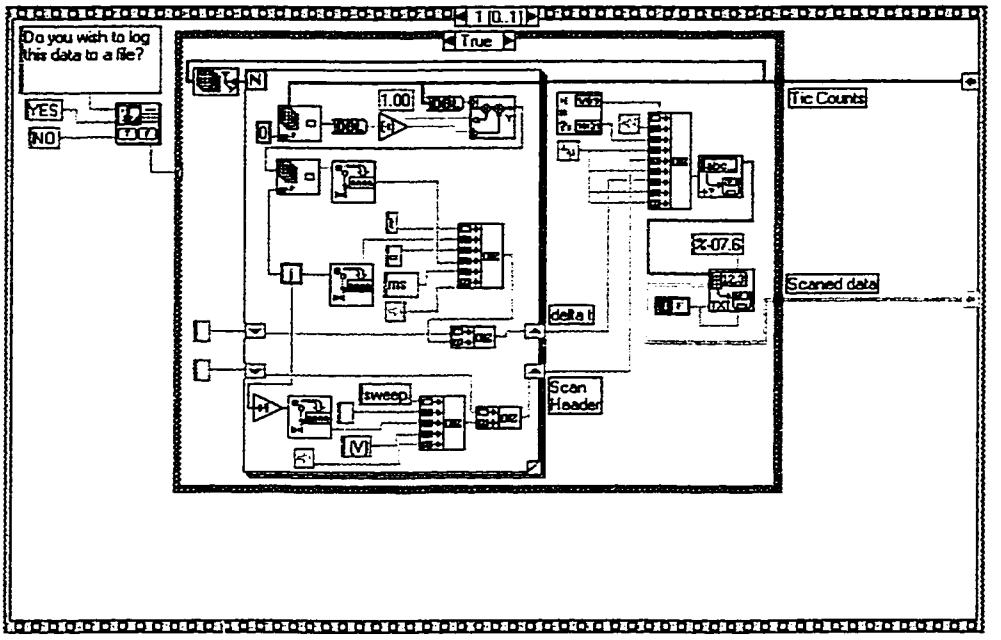
1 [0..1]
True
Do you wish to log this data to a file?
YES
NO
N
1.00
Tic Counts
2-07.6
Scaned data
delta t
Scan Header
sweep
ms
V
Fake

APPENDIX C: DATA INTERPOLATION ROUTINE – USER INTERFACE AND SOURCE CODE

Interpolation Filter Routine: User Interface

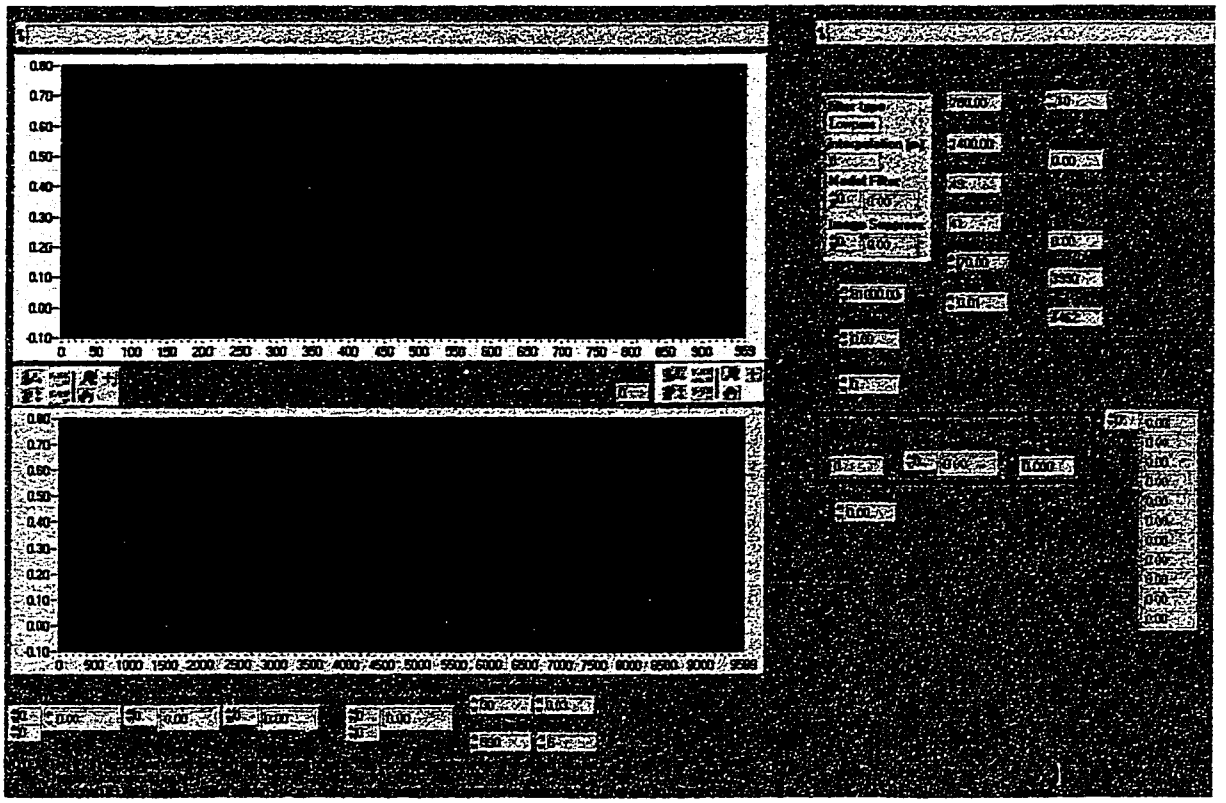

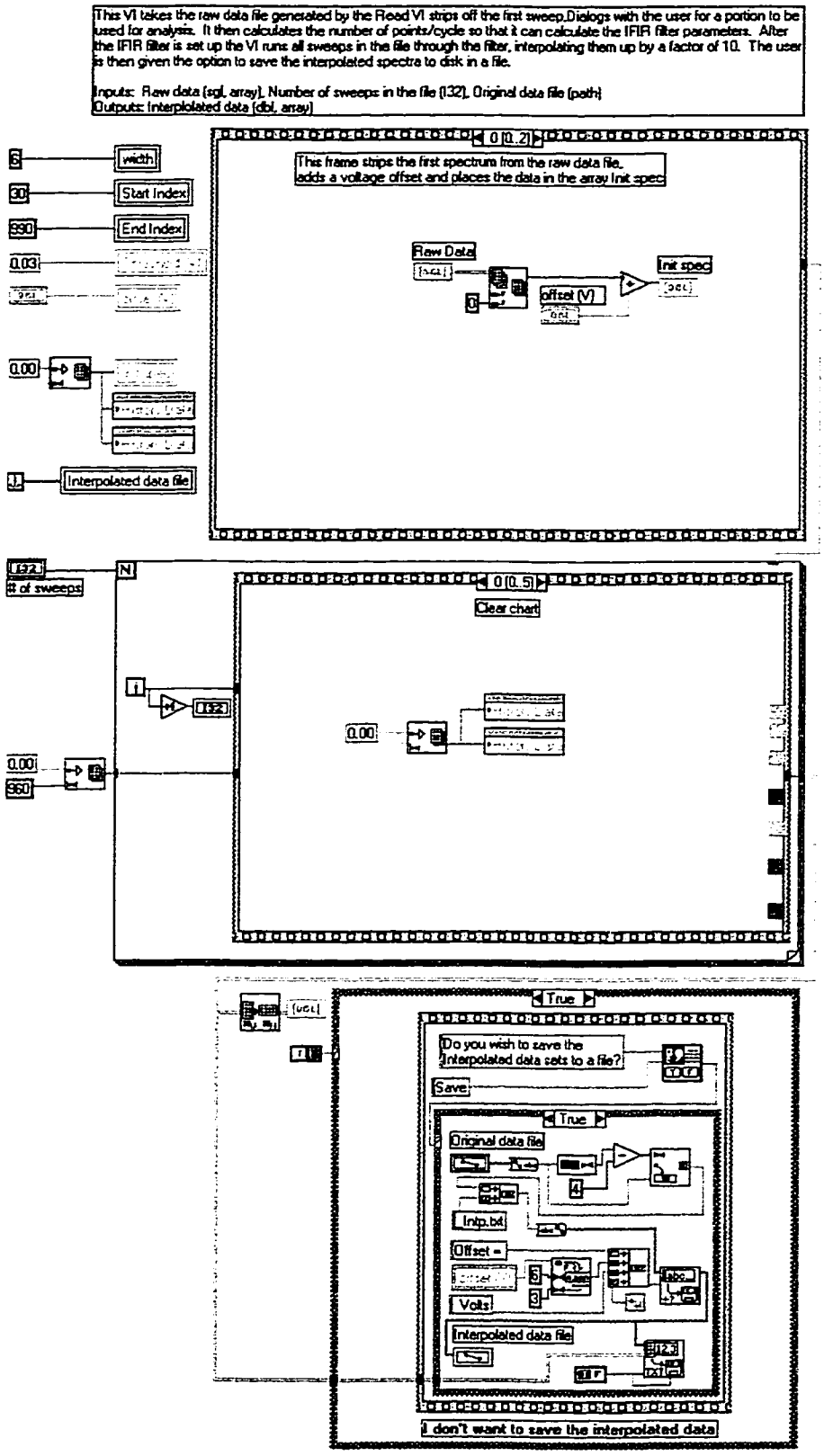
This VI takes the raw data file generated by the Read VI strips off the first sweep.Dialogs with the user for a portion to be used for analysis. It then calculates the number of points/cycle so that it can calculate the IFIR filter parameters. After the IFIR filter is set up the VI runs all sweeps in the file through the filter, interpolating them up by a factor of 10. The user is then given the option to save the interpolated spectra to disk in a file.
Inputs: Raw data (sgl, array), Number of sweeps in the file (132), Original data file (path)
Outputs: Interpolated data (dbl, array)
width
Start Index
End Index
Interpolated data file
This frame strips the first spectrum from the raw data file, adds a voltage offset and places the data in the array Init spec
Raw Data
offset (V)
Init spec
# of sweeps
Clear chart
Do you wish to save the interpolated data sets to a file?
Save
Original data file
Intp.txt
Offset =
Volts
Interpolated data file
I don't want to save the interpolated data

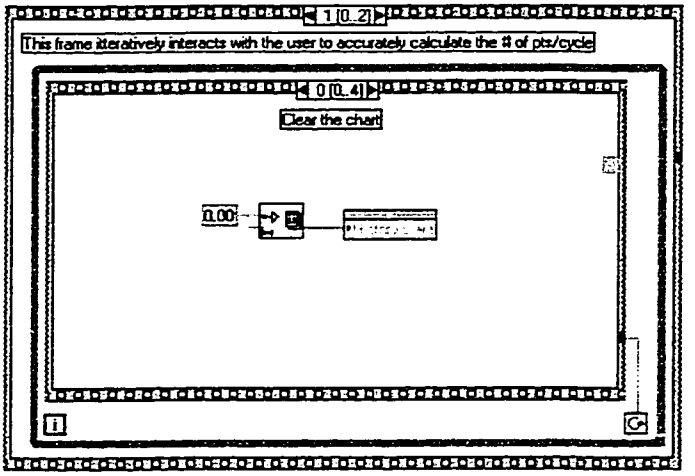
1 [0..2]
This frame iteratively interacts with the user to accurately calculate the # of pts/cycle
0 [0..4]
Clear the chart
0.00
i

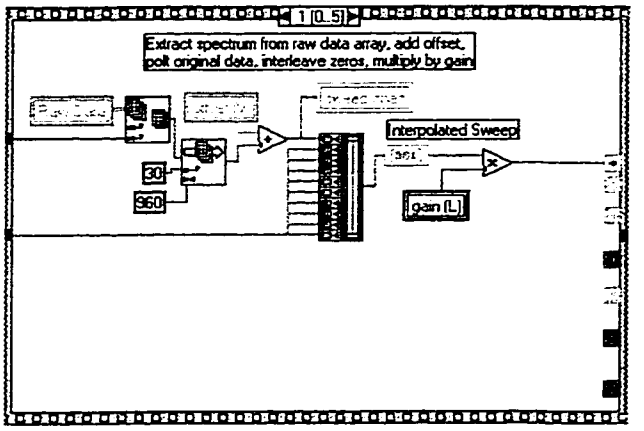
1 [0..5]
Extract spectrum from raw data array, add offset,
poit original data, interleave zeros, multiply by gain
Interpolated Sweep
30
960
gain [L]

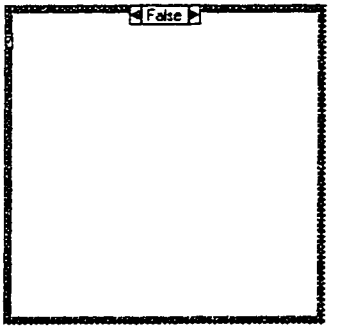
False

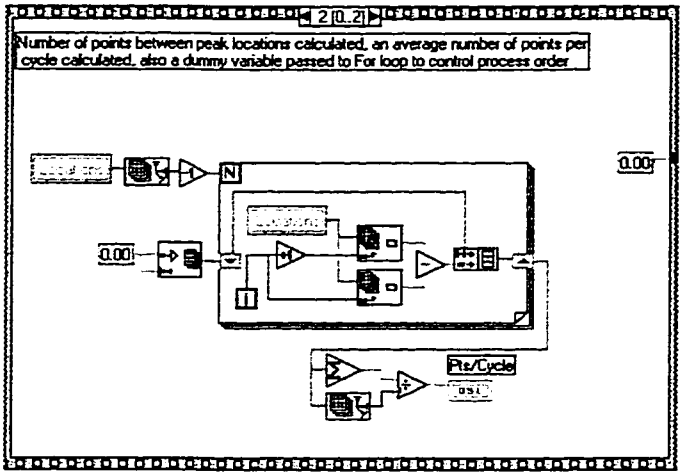
2 [0..2]
Number of points between peak locations calculated, an average number of points per cycle calculated, also a dummy variable passed to For loop to control process order
N
0.00
0.00
Pts/Cycle

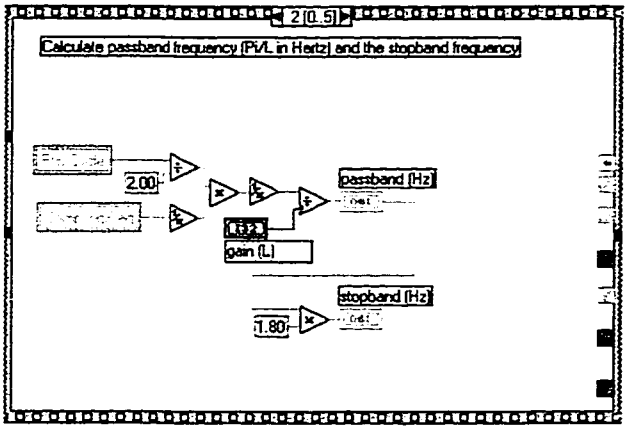
2 [0..5]
Calculate passband frequency (Pi/L in Hertz) and the stopband frequency
2.00
passband (Hz)
gain (L)
stopband (Hz)
1.80

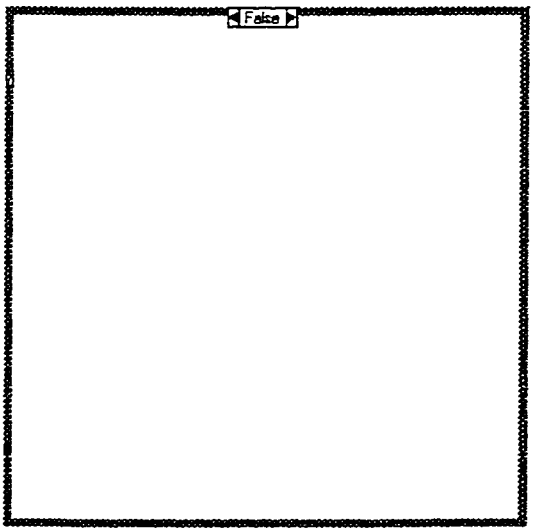
False

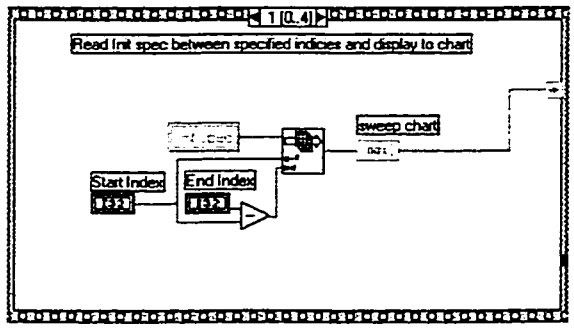
1 [0..4]
Read Init spec between specified indices and display to chart
sweep chart
Start Index
End Index

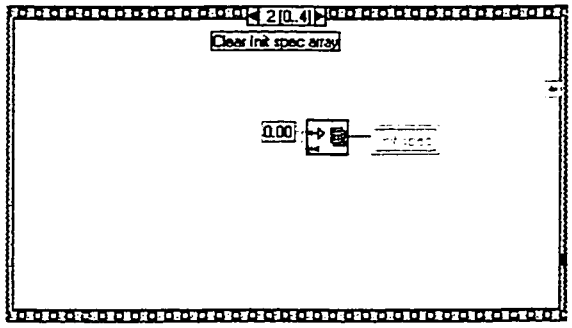
2 [0..4]
Clear Init spec array
0.00

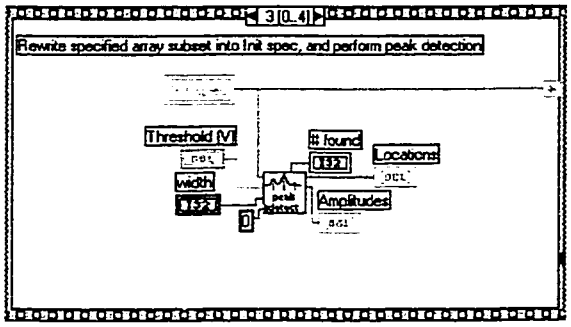
3 [0..4]
Rewrite specified array subset into Init spec, and perform peak detection
Threshold (V)
width
found
Locations
Amplitudes

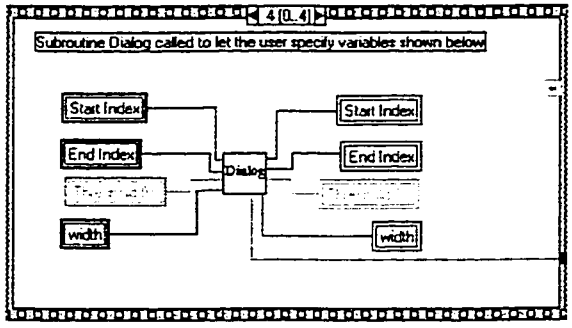
4 [0..4]
Subroutine Dialog called to let the user specify variables shown below
Start Index
End Index
width
Dialog
Start Index
End Index
width

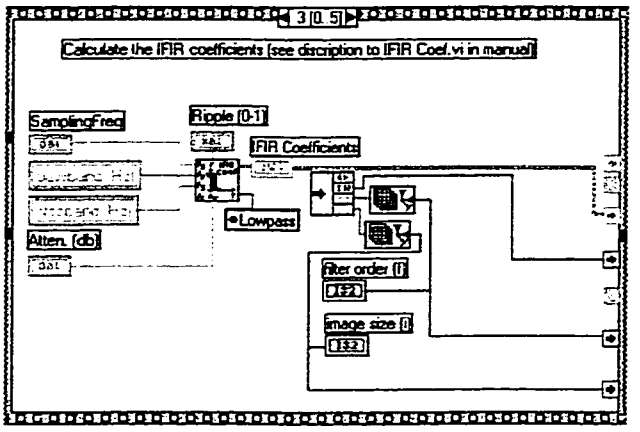
3 [0..5]
Calculate the IFIR coefficients (see discription to IFIR Coef.vi in manual)
SamplingFreq
Ripple [0-1]
IFIR Coefficients
Lowpass
Atten. (db)
filter order (I
image size (I

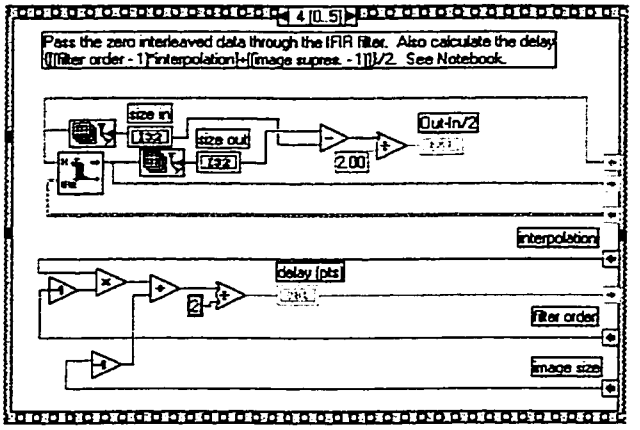
4 [0..5]
Pass the zero interleaved data through the IFIR filter. Also calculate the delay
((filter order - 1)*interpolation)+(image supres. - 1))/2. See Notebook.
size in
size out
2.00
Out-In/2
interpolation
delay (pts
filter order
image size

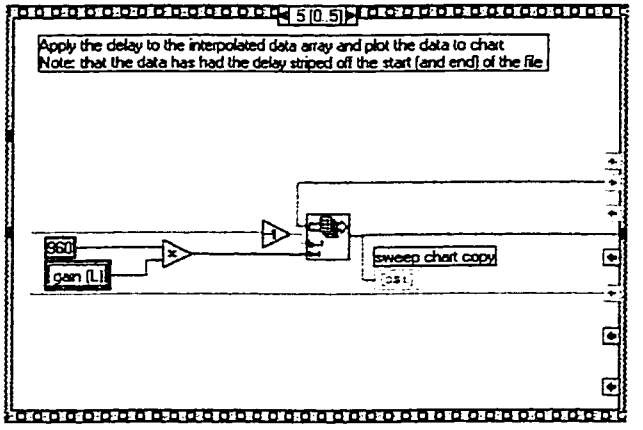
5 [0..5]
Apply the delay to the interpolated data array and plot the data to chart
Note: that the data has had the delay striped off the start (and end) of the file
360
gain (L)
sweep chart copy

APPENDIX D: CROSS CORRELATION ANALYSIS ROUTINE – USER INTERFACE AND SOURCE CODE

Cross Correlation Analysis Routine: User Interface

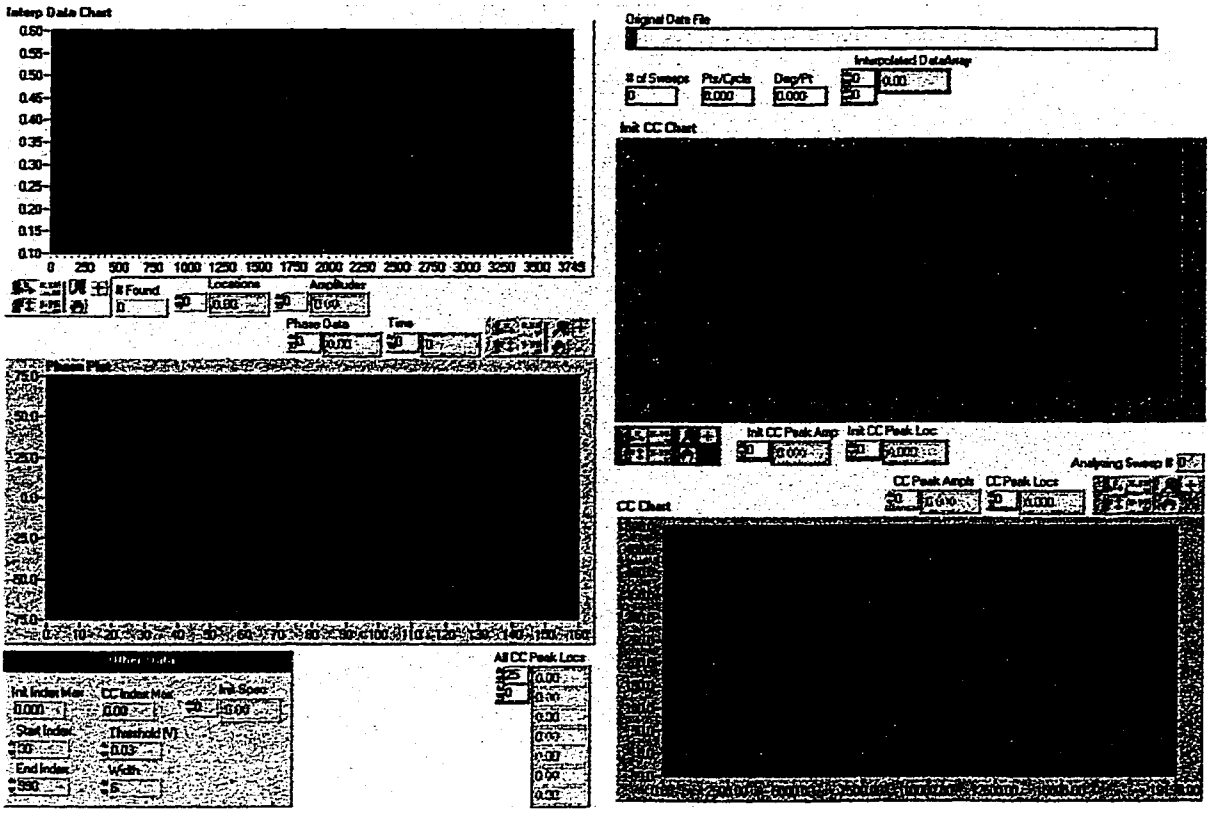

Cross Correlation Analysis Routine: Source Code

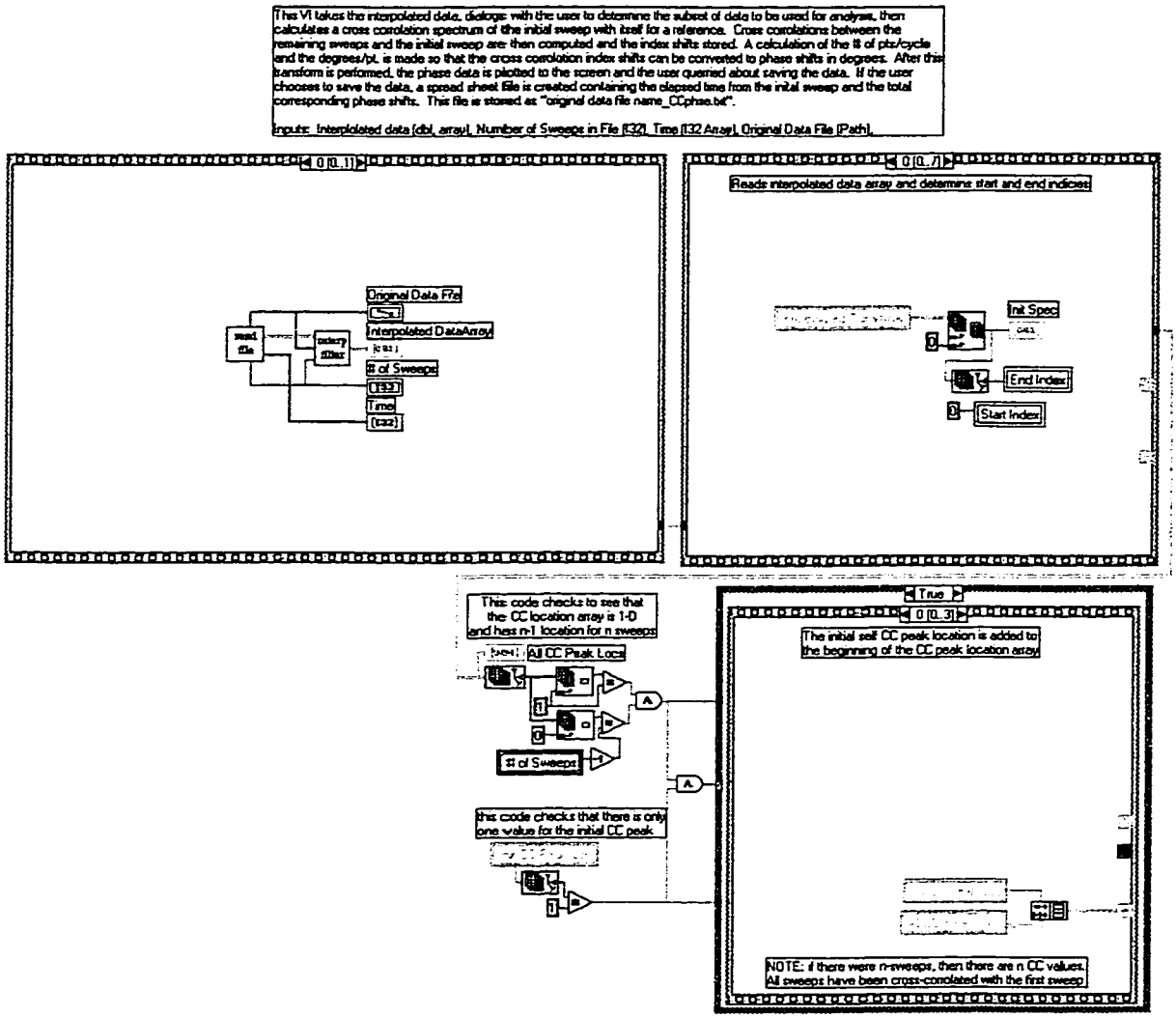

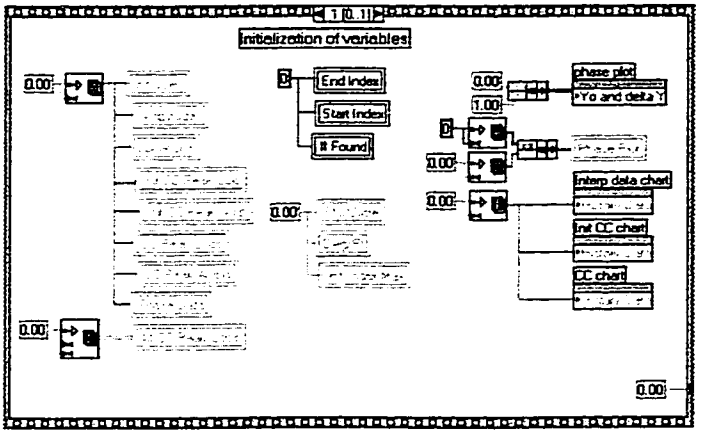
1 [0..1]
Initialization of variables
0.00
End Index
Start Index
If Found
0.00
phase plot
Yo and delta Y
0.00
1.00
0
0.00
0.00
Interp data chart
Int CC chart
CC chart
0.00
0.00

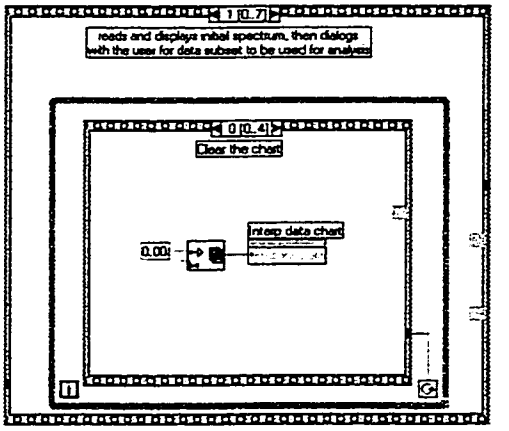
1 [0..7]
reads and displays initial spectrum, then dialogs with the user for data subset to be used for analysis
0 [0..4]
Clear the chart
Interp data chart
0.00
i

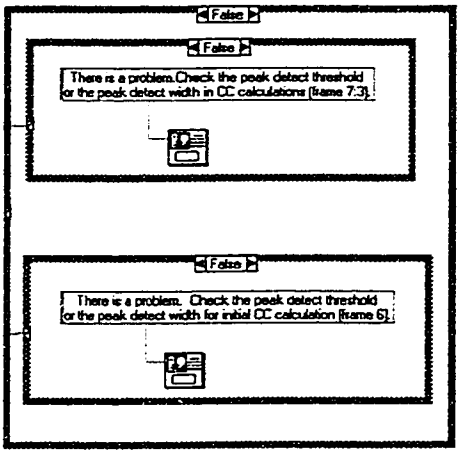
False
False
There is a problem.Check the peak detect threshold or the peak detect width in CC calculations (frame 7.3).
False
There is a problem. Check the peak detect threshold or the peak detect width for initial CC calculation (frame 6).

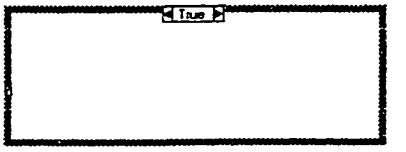
True

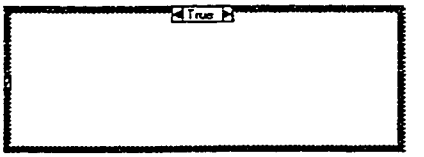
True

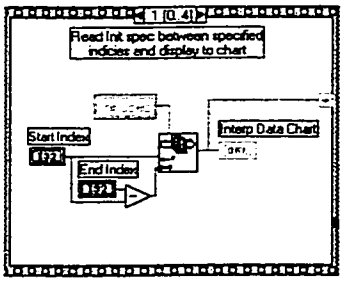
1 [0..4]
Read Int spec between specified indices and display to chart
Start Index
End Index
Interp Data Chart

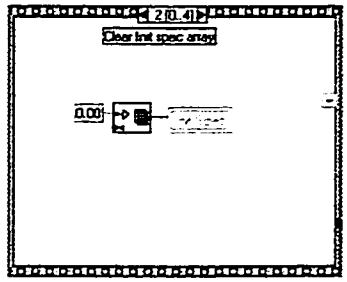
2 [0..4]
Clear Init spec array
0.00

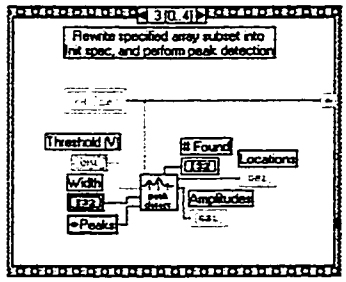
3 [0..4]
Rewrite specified array subset into Init spec, and perform peak detection
Threshold (V)
Width
Peaks
Found
Locations
Amplitudes

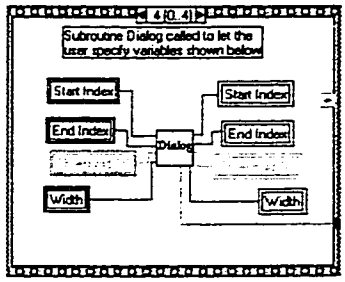
4 [0..4]
Subroutine Dialog called to let the user specify variables shown below
Start Index
End Index
Width
Dialog
Start Index
End Index
Width

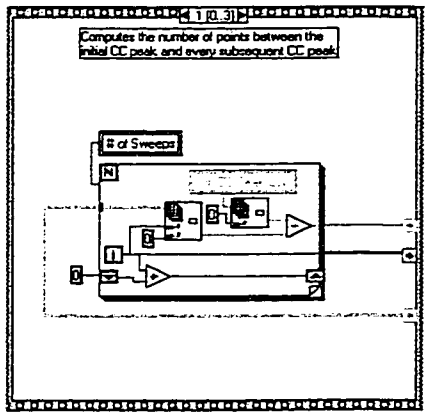
1 [0..3]
Computes the number of points between the initial CC peak and every subsequent CC peak
# of Sweeps
N
0
1
0

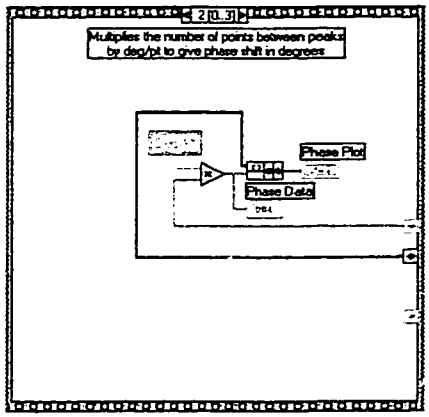
2 [0..3]
Multiplies the number of points between peaks by deg/pt to give phase shift in degrees
Phase Plot
Phase Data

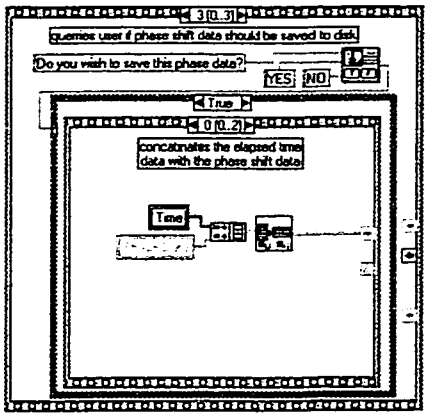
3 [0..3]
queries user if phase shift data should be saved to disk
Do you wish to save this phase data?
YES
NO
True
0 [0..2]
concatinates the elapsed time data with the phase shift data
Time

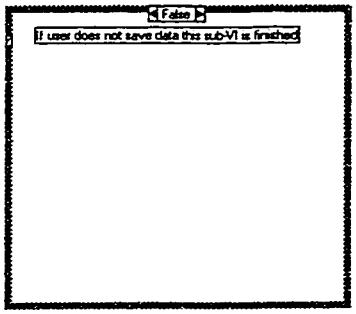
False
If user does not save data this sub-VI is finished

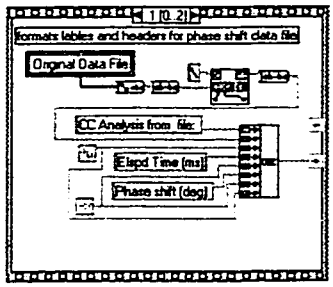
1 [0..2]
formats lables and headers for phase shift data file
Original Data File
CC Analysis from file
Elapd Time (ms)
Phase shift (deg)

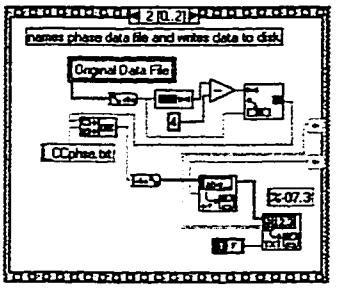
2 [0..2]
names phase data file and writes data to disk
Original Data File
CCphase.txt

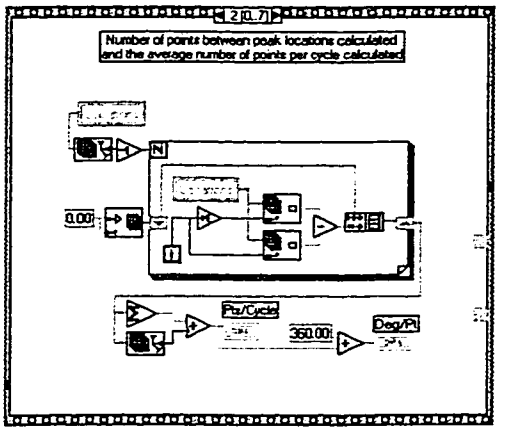
2 [0..7]
Number of points between peak locations calculated
and the average number of points per cycle calculated
N
0.00
i
Pts/Cycle
360.00
Deg/Pt

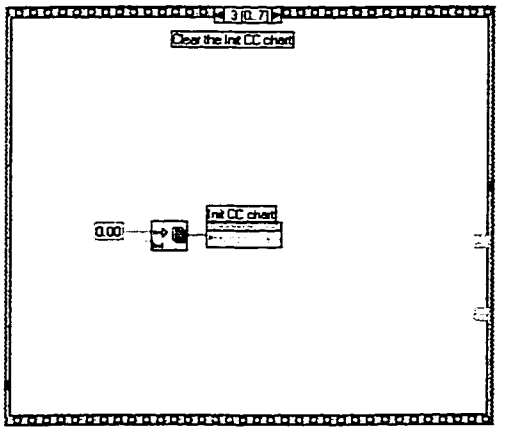
3 [0..7]
Clear the Init CC chart
0.00
Init CC chart

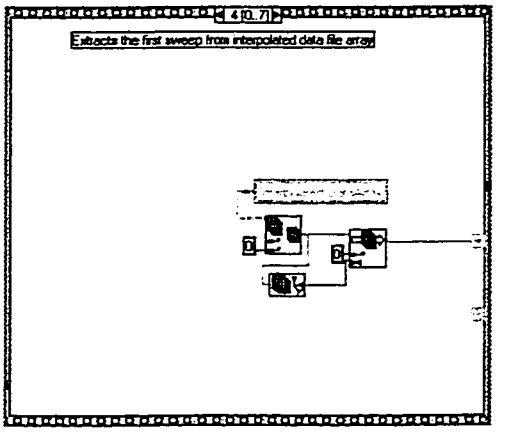
4 [0..7]
Extracts the first sweep from interpolated data file array

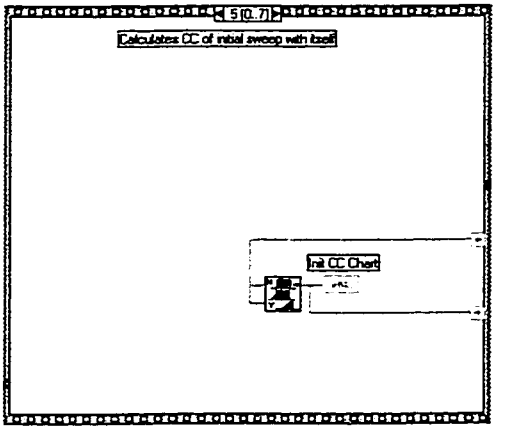
5 [0..7]
Calculates CC of initial sweep with itself
Init CC Chart

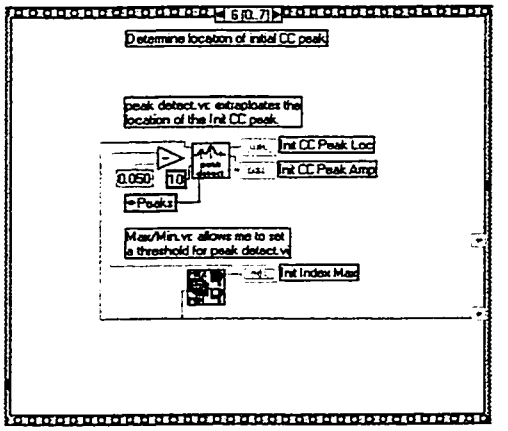
6 [0..7]
Determine location of initial CC peak
peak detect.vi extrapolates the location of the Init CC peak.
Init CC Peak Loc
Init CC Peak Amp
0.050
1.0
Peaks
Max/Min.vi allows me to set a threshold for peak detect.vi
Init Index Max

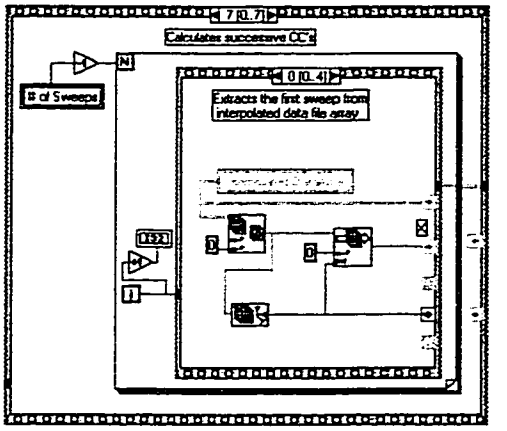
7 [0..7]
Calculates successive CC's
N
# of Sweeps
0 [0..4]
Extracts the first sweep from interpolated data file array
192
1

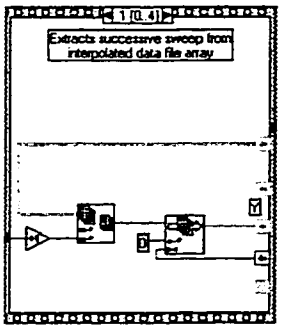
1 [0..4]
Extracts successive sweep from interpolated data file array

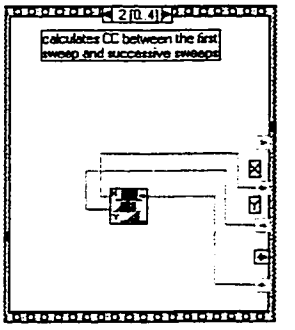
2 [0..4]
calculates CC between the first sweep and successive sweeps

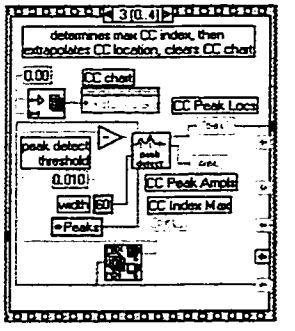
3 [0..4]
determines max CC index, then extrapolates CC location, clears CC chart
0.00
CC chart
CC Peak Locs
peak detect threshold
0.010
width
80
#Peaks
CC Peak Ampls
CC Index Max

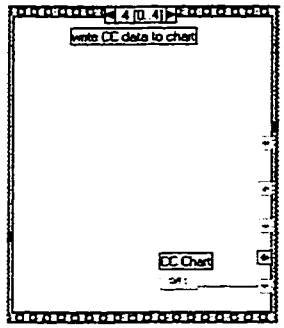
write OC data to chart
OC Chart

APPENDIX E: FAST FOURIER TRANSFORM ANALYSIS ROUTINE – USER INTERFACE AND SOURCE CODE

Fast Fourier Transform Analysis Routine: User Interface

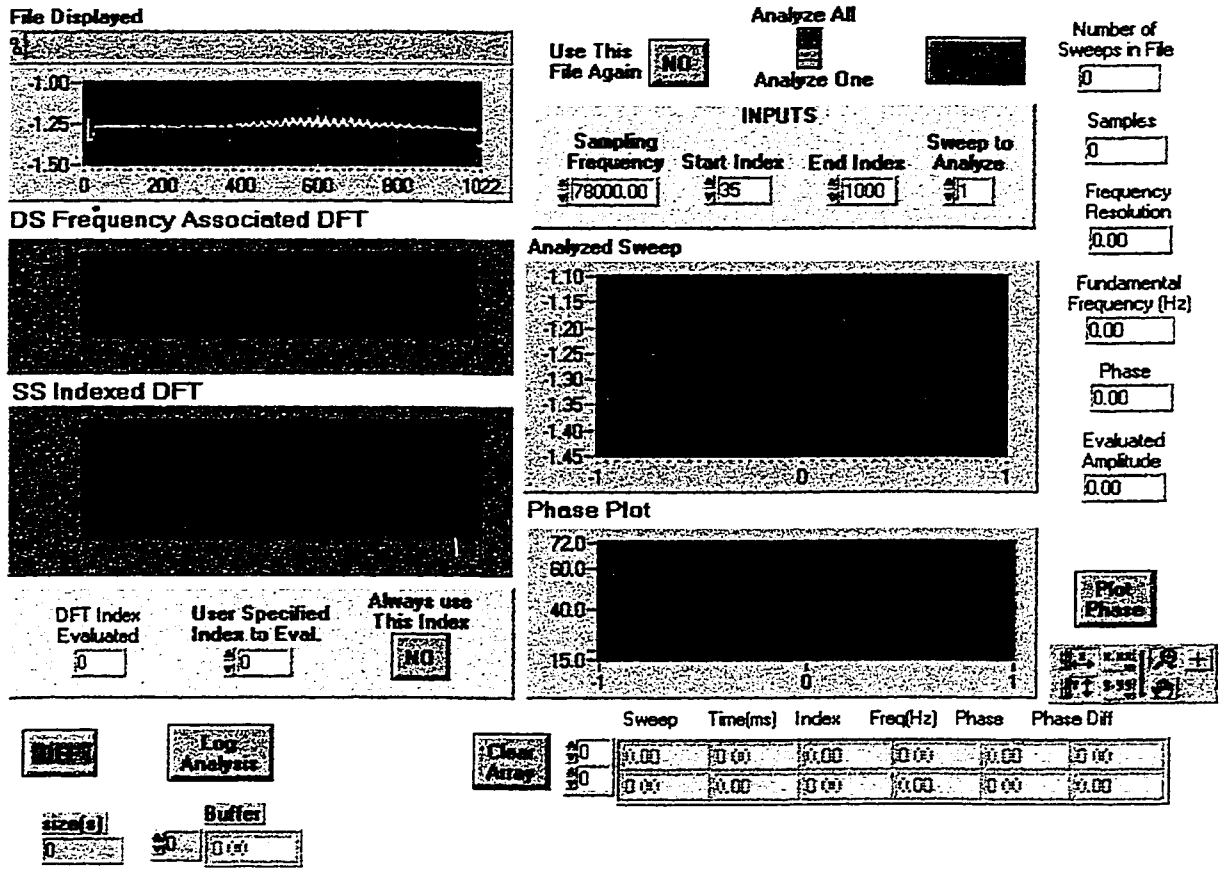

Fast Fourier Transform Analysis Routine: Source Code

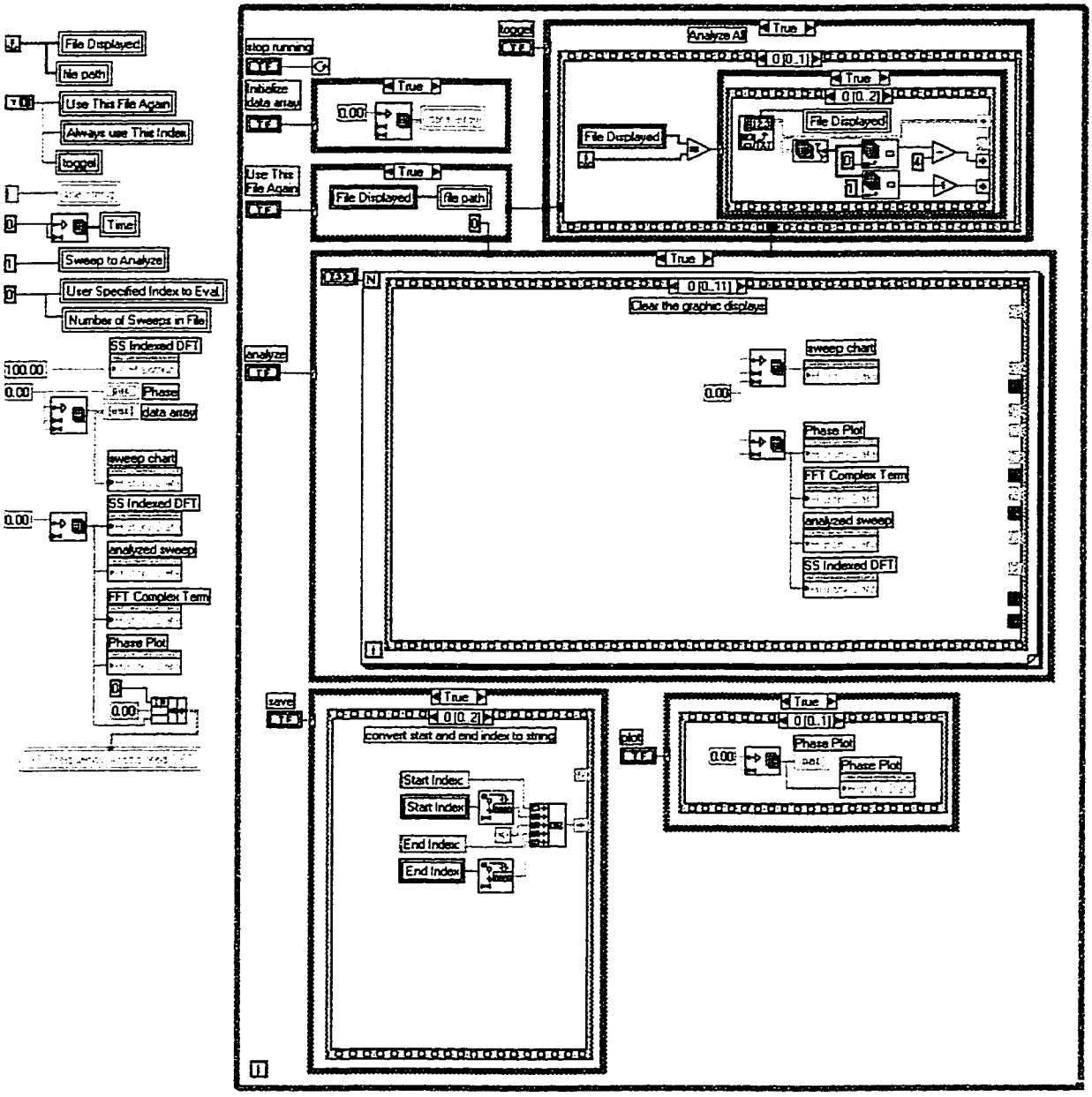

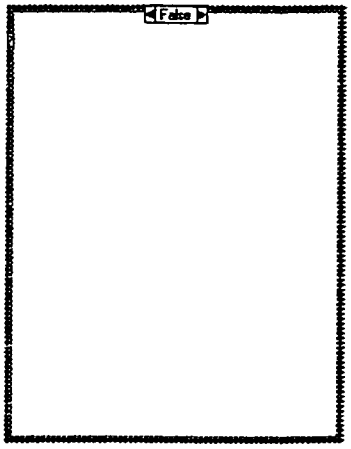
False

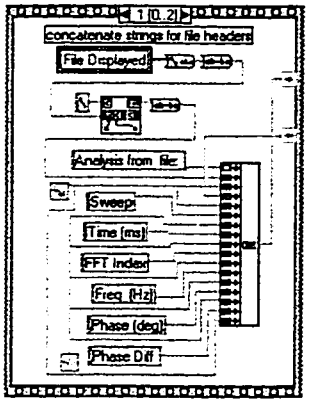
1 [0..2]
concatenate strings for file headers
File Displayed
Analysis from file:
Sweep
Time (ms)
FFT Index
Freq. (Hz)
Phase (deg)
Phase Diff

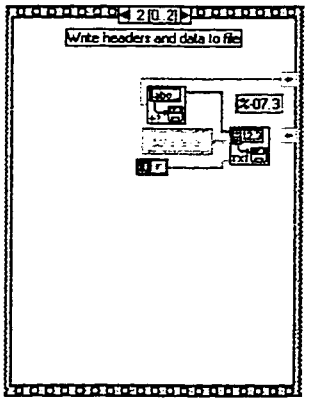
2 [0..2]
Write headers and data to file
%.07.3

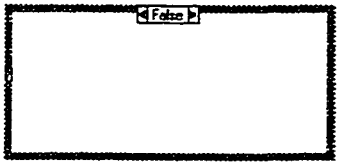
False

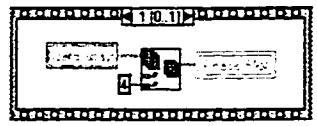
1 [0..1]

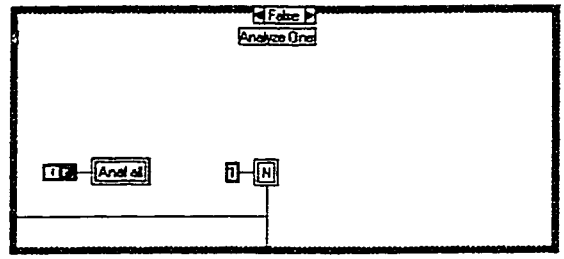
False
Analyze One
Anal all
N

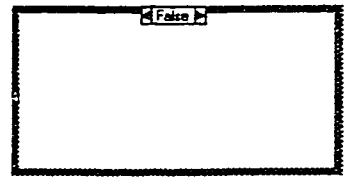
False

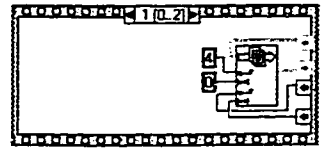
1 [0..2]

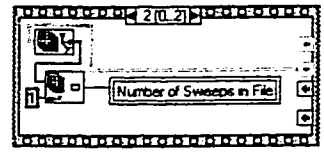
2 [0..2]
Number of Sweeps in File

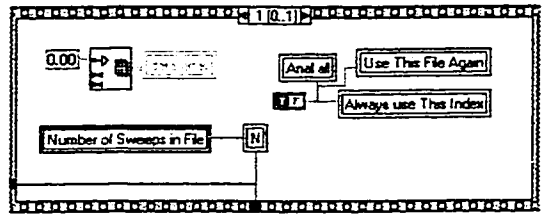
1 [0..1]
0.00
Anal all
Use This File Again
Always use This Index
Number of Sweeps in File
N

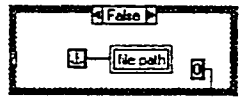
False
No path


False

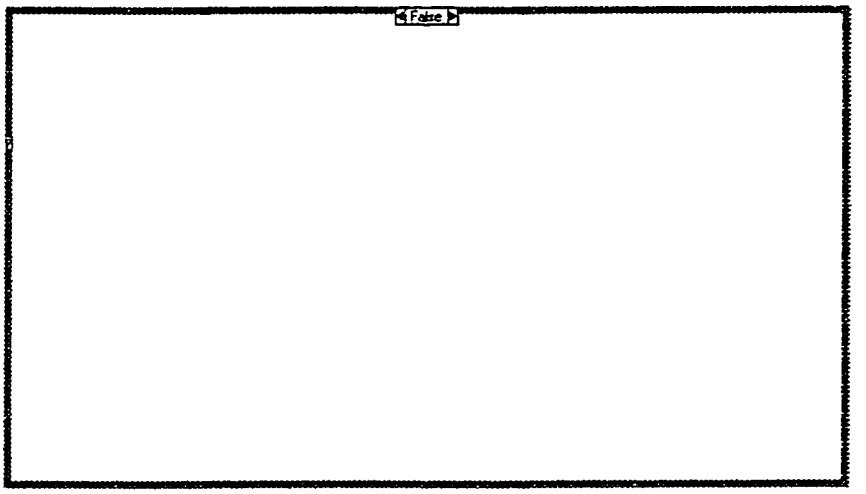
False

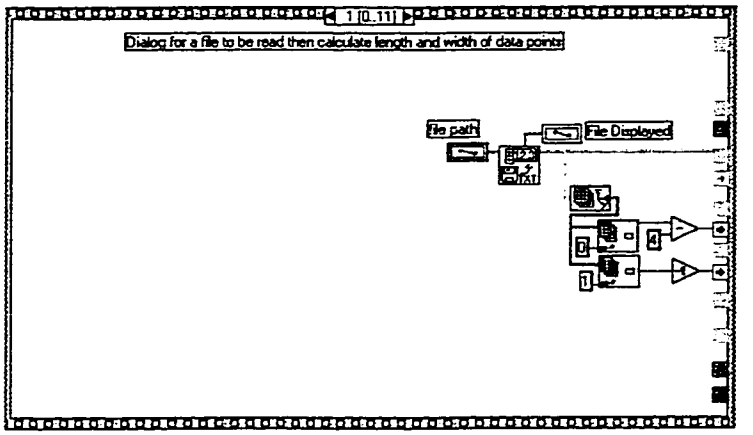
1 [0..11]
Dialog for a file to be read then calculate length and width of data points
File path
File Displayed

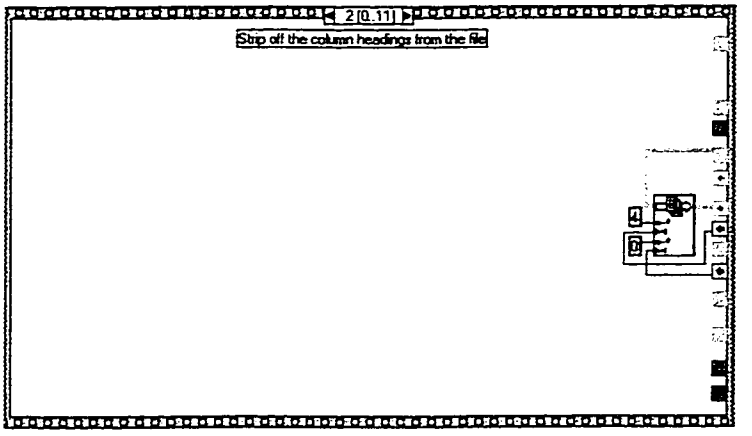
2 [0..11]
Strip off the column headings from the file

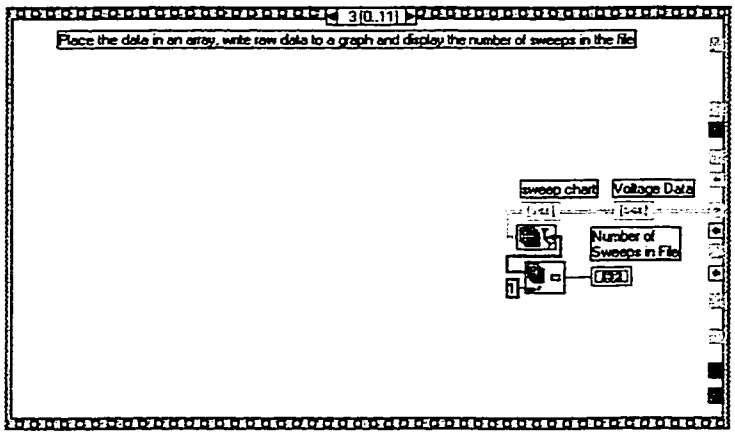
3 [0..11]
Place the data in an array, write raw data to a graph and display the number of sweeps in the file
sweep chart
Voltage Data
Number of Sweeps in File

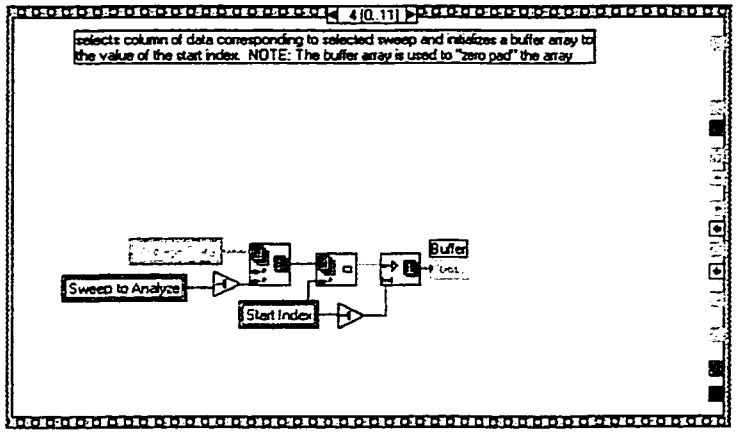
4 [0..11]
selects column of data corresponding to selected sweep and initializes a buffer array to the value of the start index. NOTE: The buffer array is used to "zero pad" the array
Buffer
Sweep to Analyze
Start Index

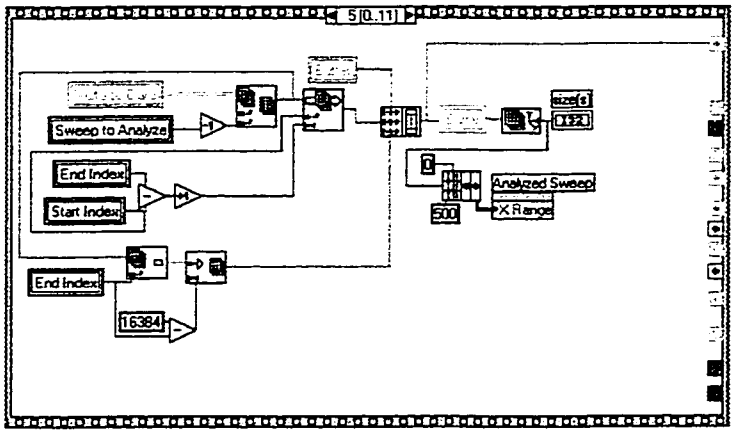
5 [0..11]
Sweep to Analyze
End Index
Start Index
Analyzed Sweep
X Range
500
End Index
16384

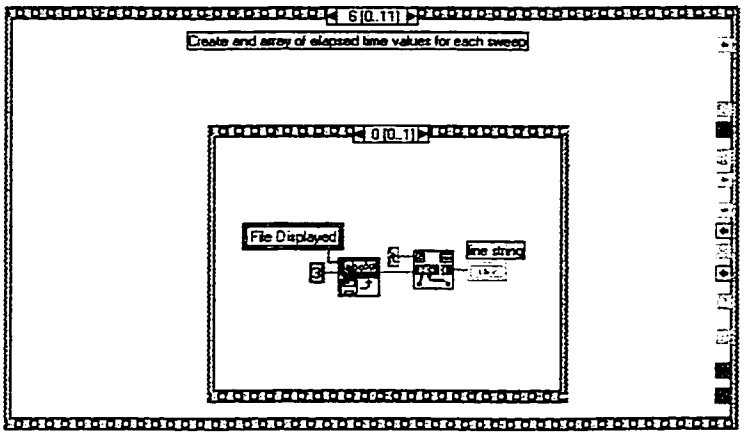
6 [0..11]
Create and array of elapsed time values for each sweep
0 [0..1]
File Displayed
line string

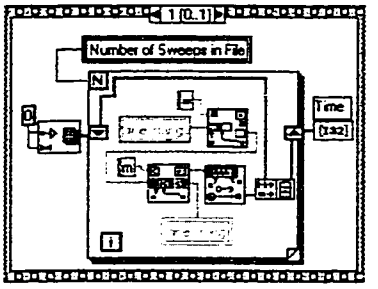
1 [0..1]
Number of Sweeps in File
N
Time
[132]
i

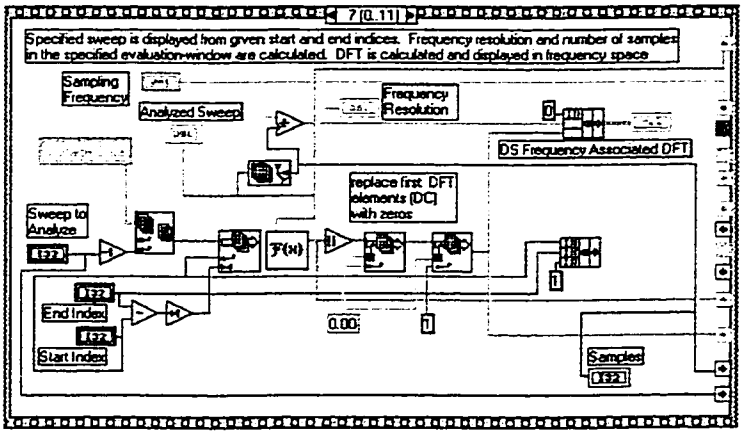
7 [0..11]
Specified sweep is displayed from given start and end indices. Frequency resolution and number of samples in the specified evaluation-window are calculated. DFT is calculated and displayed in frequency space
Sampling Frequency
Analyzed Sweep
Frequency Resolution
DS Frequency Associated DFT
replace first DFT elements (DC) with zeros
Sweep to Analyze
F(x)
End Index
Start Index
0.00
Samples

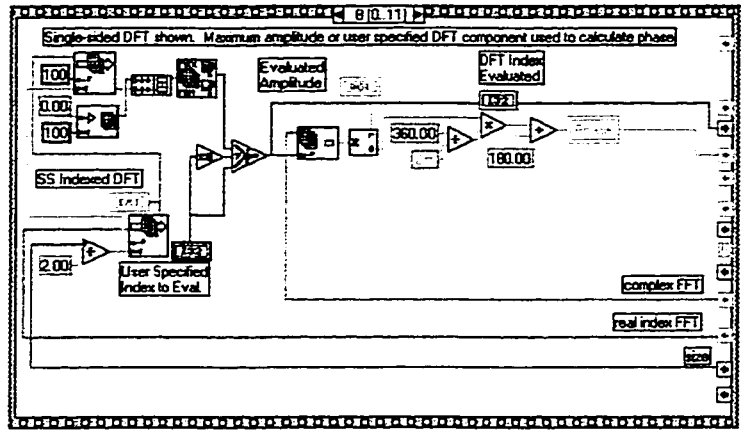
8 [0..11]
Single-sided DFT shown. Maximum amplitude or user specified DFT component used to calculate phase
100
0.00
100
Evaluated Amplitude
DFT Index Evaluated
360.00
180.00
SS Indexed DFT
2.00
User Specified Index to Eval
complex FFT
real index FFT
size

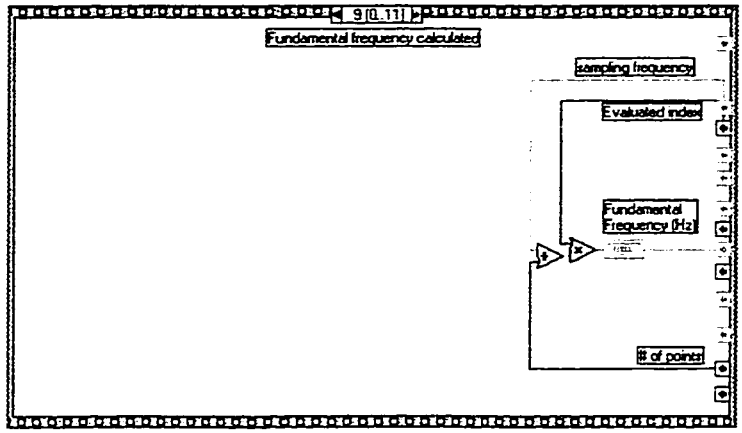
9 [0..11]
Fundamental frequency calculated
sampling frequency
Evaluated index
Fundamental Frequency (Hz)
# of points

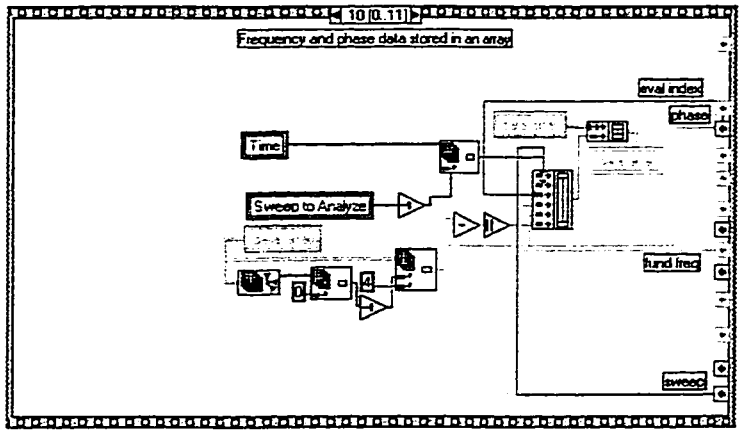
10 [0..11]
Frequency and phase data stored in an array
eval index
phase
Time
Sweep to Analyze
fund freq
sweep

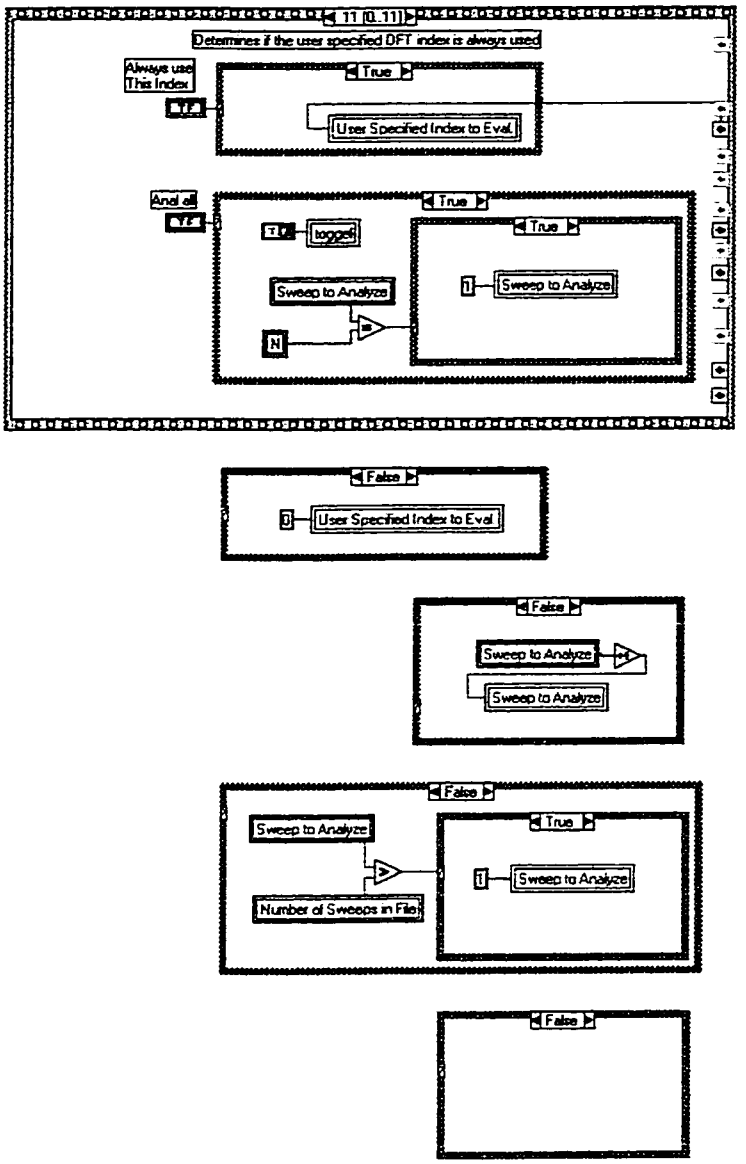
11 [0..11]
Determines if the user specified DFT index is always used
Always use This Index
TF
True
User Specified Index to Eval
Anal all
TF
True
TF
logged
True
Sweep to Analyze
1
Sweep to Analyze
N
False
0
User Specified Index to Eval
False
Sweep to Analyze
Sweep to Analyze
False
Sweep to Analyze
True
1
Sweep to Analyze
Number of Sweeps in File
False

APPENDIX F: PRELIMINARY MODAL INVESTIGATION BY COUPLER HEATING

Close inspection of spectra from the output of these devices (see Figure 18) shows irregular fringe structure. Irregularities in an interferogram can arise from a variety of sources. In the current device, potential sources that could cause irregularities in the interferograms include: dust particles or micro chips on the entrance or exit end face of the waveguides, surface irregularities in any of the steering mirrors, small amounts of reflection (4%) from the two sides of the beam splitter, dark current noise of the array detector, odd/even patterning of the array detector, and pixel dropouts in the detector. In addition to these sources, fine structure observed in an interferogram produced by two waveguides (integrated or fiber) could be the result of intermodal interference.

The number of modes that will propagate in a circular waveguide structure is a function of normalized frequency (V), the difference between the core refractive index (n_1) and the cladding refractive index (n_2), the wavelength of light (λ), and the radius of the waveguide (r). The relationship is given by:

$$V = \frac{2\pi}{\lambda} r (n_1^2 - n_2^2)^{\frac{1}{2}} \qquad \text{(F1)}$$

For values of V less then 2.405 only a single mode will be supported. For values of V much greater then 2.405, the specific number of guided modes (M_s) for a step index circular waveguide is given by the approximate expression [Senior 1885]:

$$M_s \approx \frac{V^2}{2} \qquad \text{(F2)}$$

Because the waveguides fabricated in the present work have a square cross section (and no closed form solution to the wave equation), Equation (F1) can only serve as an approximation for the normalized frequency of the waveguides. An empirical method is therefore necessary to determine the modal properties of these waveguides.

Equation (F1) shows that the number of modes supported by a waveguide is inversely proportional to the wavelength of light being propagated. The single mode cutoff frequency ($\frac{1}{\lambda}$) for a given waveguide is then defined to be the frequency below which, there can only be a single propagation mode. The single mode cutoff frequency for any waveguide can be determined empirically if the proper equipment is available. A monochromator is used as a source to launch light into the waveguide while the far field output is monitored. A single spot or lobe will appear in the far field corresponding to each propagating mode. These spots will be resolvable until there are so many modes propagating that the lobes begin to overlap. Using the monochromator to scan the source wavelength, the single mode cutoff frequency can accurately be determined by looking at the number of lobes in the far field output pattern.

A monochromator was not immediately available for use in the current project. As a preliminary modal investigation of the device, 10 μl drops of water were heated to a controlled temperature and placed on a directional coupler (*C1*, Figure 3) while monitoring the corresponding output (right side). Placing the water-droplet heat source on the coupler heated both arms of the corresponding interferometer equally. It is assumed that if two modes were supported, and enough heat applied to the waveguides, the differential response of the modes would cause them to be spatially separated at the output. This effect might then be observed in the fine structure of the output interferogram.

In each experiment, the interferogram was monitored for three seconds. The spectrum was scanned and recorded every 200 ms during this interval. A three second

experimental duration was chosen based on the results of data presented in Figures 27 and 28. They show an interferometric response of the device occurring in about 500 ms to a heated 10 μl water droplet. Several experiments were carried out in the absence of any water droplets for baseline references. Results from a representative reference experiment are shown in Figure F1. The water droplets used as a heat source were 10 μl in volume. When the water contacted the device, it was 49.2 °C above the device surface temperature. Several experiments were carried out in the same manner as the reference experiments using the water heat-source to heat the coupler. Results from a representative coupler-heated experiment are shown in Figure F2.

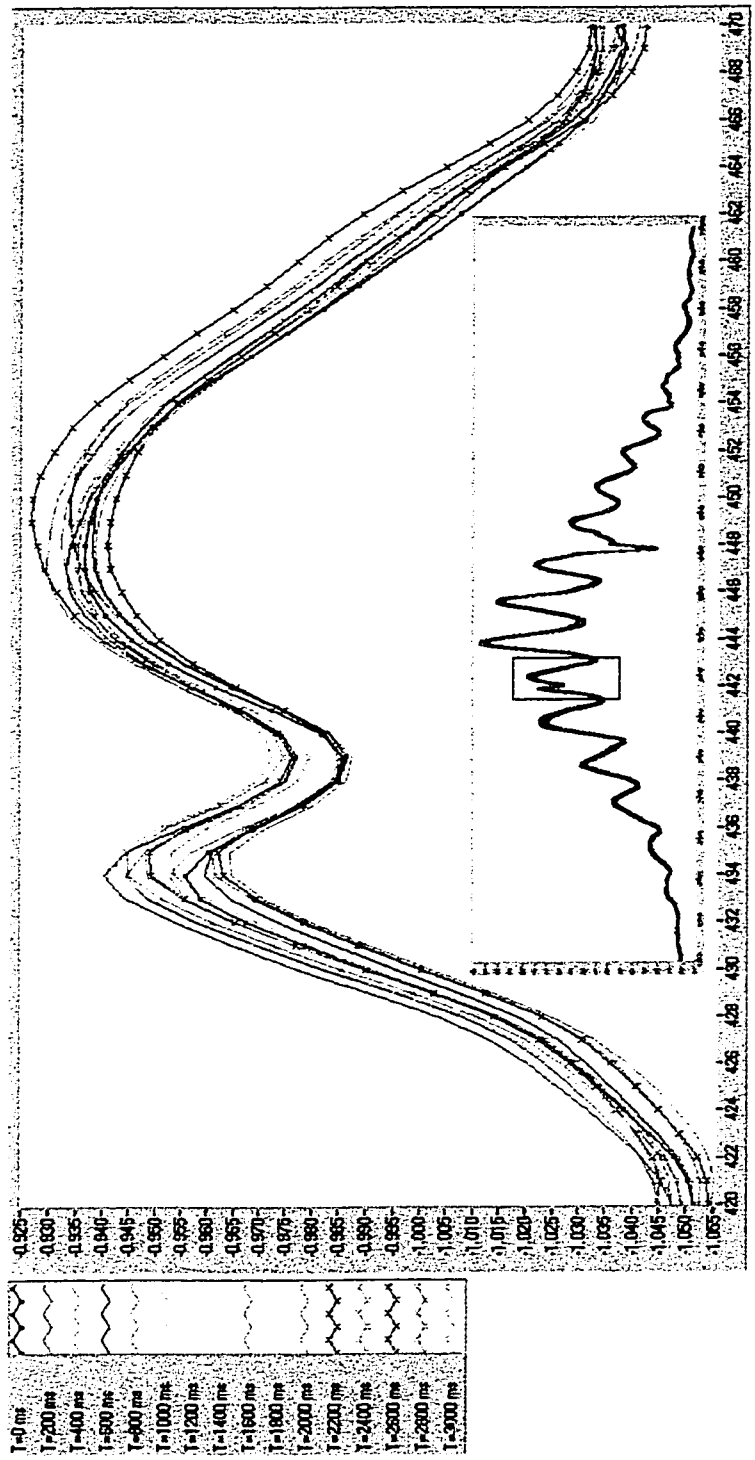

Figure F1. Results from representative baseline reference experiment obtained for modal investigation. The inset shows the entire interferogram. A box in the inset has been placed around the fringe shown in the main graph.

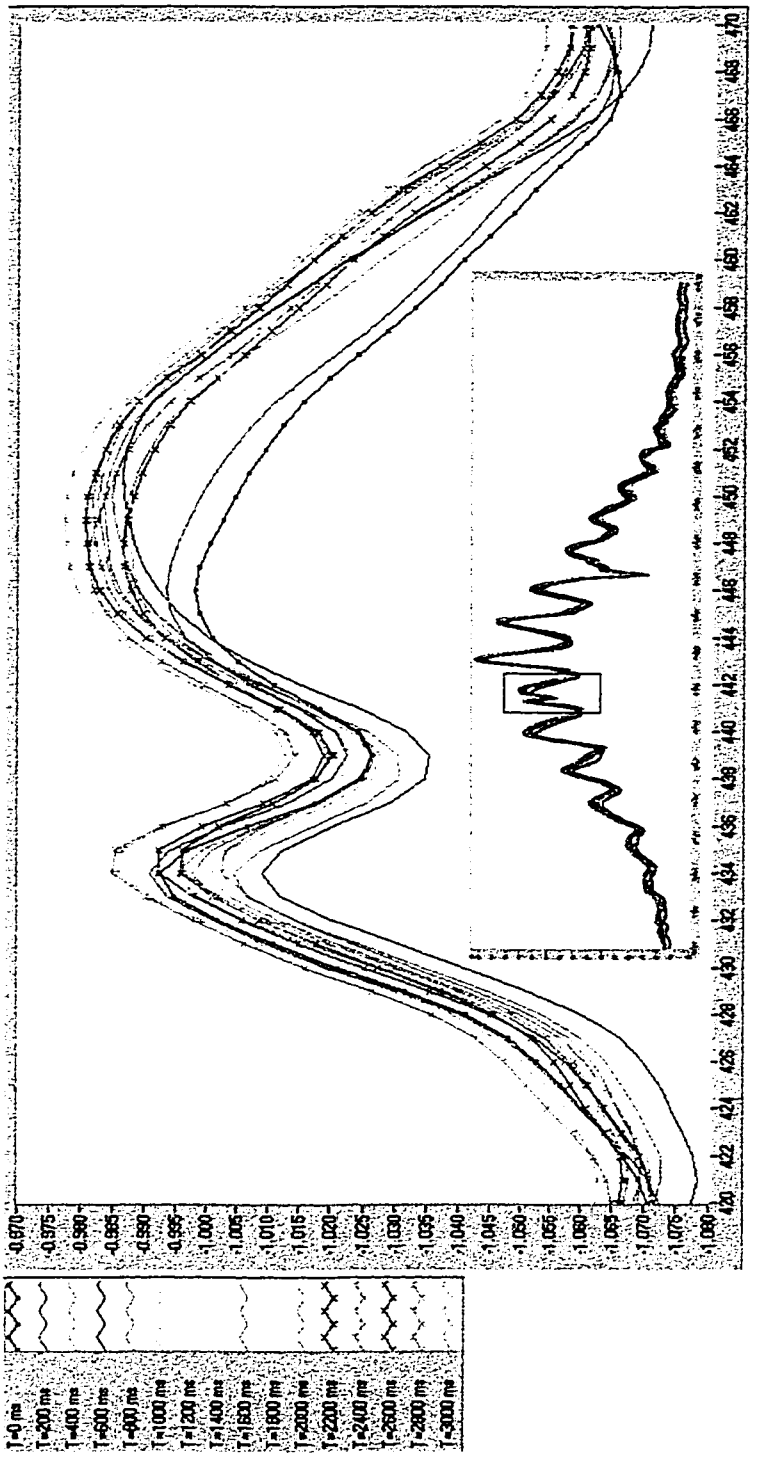

Figure F2. Results from representative heated coupler experiment obtained for modal investigation. The inset shows the entire interferogram. A box in the inset has been placed around the fringe shown in the main graph.

The fringe expanded in Figure F1 and in Figure F2 was chosen because of the fine structure present. It was expected that if changes in the interferogram due to propagation of multiple modes could be detected, they would appear in this fringe. The baseline data in Figure F1 reveal that when there is no active heating of the device, the fringe amplitudes show some variation. The heated coupler data presented (Figure F2) also shows amplitude variations in the peaks of the expanded fringe as well as a slight shift in position. The heated coupler data also shows a trending amplitude decrease of the left peak with respect to time, while the right peak shows a trending amplitude increase.

When a heated water droplet is placed on the coupler it is unlikely that heat will be distributed symmetrically over equal lengths of the interferometer arms. Interferometery is an extremely sensitive sensing technique. Therefore, it is also unlikely that spectral modulations observed while the coupler was heated are void phase shifts from slight asymmetrical heating. It is unclear how much of the amplitude modulation observed in Figure F2 is in fact due asymmetrical heating. Baseline noise in the system and expectation of some asymmetrical heat-induced phase shift make it difficult to draw definitive conclusions about the modal nature of the waveguides from these experiments. The apparent trend differences from baseline of fringe modulation seen while heating the coupler merits further investigation into the propagation modes supported by this device.

Curriculum Vita

Bryon D. Bhagwandin
515 NE 86th Street
Seattle, WA 98115
(206)526-0609

Education

Doctor of Philosophy, Bioengineering, June 1999, University of Washington, Seattle, Washington. Chairman, Professor M. A. Afromowitz. Supported in part by National Institute of Health Predoctoral Training Grant.

Thesis: *An Integrated Optical Microcalorimeter*

Master of Science, Physics, May 1986, Purdue University, West Lafayette, Indiana. Advisor, Professor F. W. Kleinhans. Supported by Methodist Hospital Medical Research Department.

Thesis: *An Electron Paramagnetic Resonance Investigation of the Production Kinetics of Superoxide Anion and Hydroxyl Radical from Stimulated Neutrophils*

Bachelor of Science, Physics, May 1984, Indiana University, Bloomington, Indiana.

Professional Experience

Director of Software Development, January 1996 – Present, Bio-Preserve Medical Corporation, 2889 – 152nd Avenue NE, Redmond, Washington 98052.

Associate Physiologist, October 1987 – September 1990, Eli Lilly and Company, Department of Central Nervous System and Endocrinology, Lilly Corporate Center, Indianapolis, Indiana.

Research Assistant, May 1985 – June 1987, Methodist Hospital of Indiana Inc., Department of Medical Research, Indianapolis, Indiana.

Honors and Awards

Outstanding Application – Biomedical Category. National Competition for Virtual Instrumentation 1998, National Instruments, Austin Texas.

National Institute of Health Predoctoral Training Grant, 1992. Department of Oral Biology, University of Washington, Seattle, Washington.

Graduate Opportunity Program Research Assistantship, 1991. Graduate School, University of Washington, Seattle, Washington.

Whitaker Research Fellow, 1990. Center for Bioengineering, University of Washington, Seattle, Washington.

Publications

List available upon request.

IMAGE EVALUATION
TEST TARGET (QA-3)

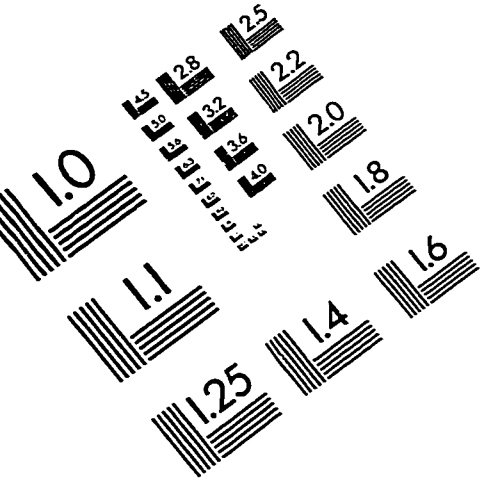

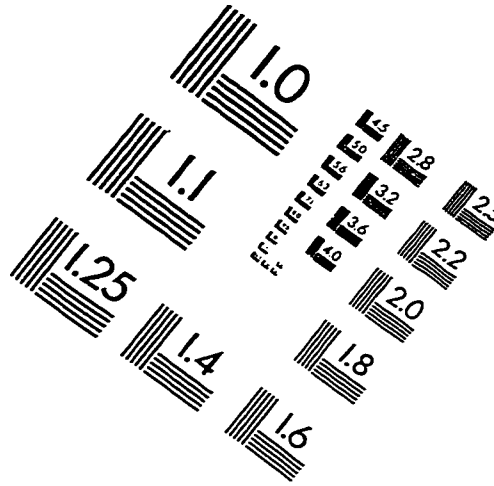

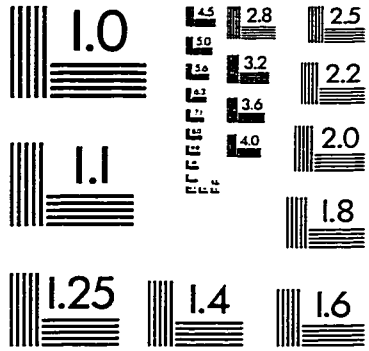

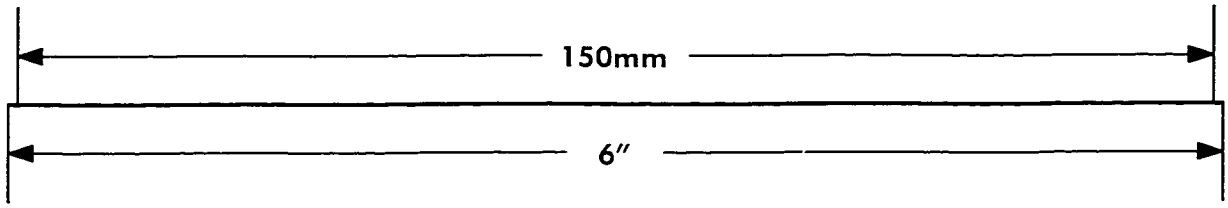

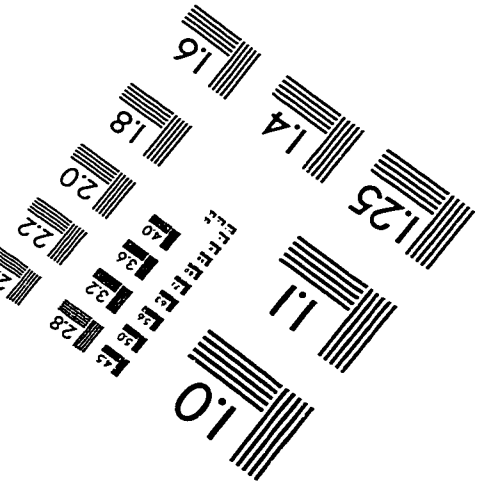

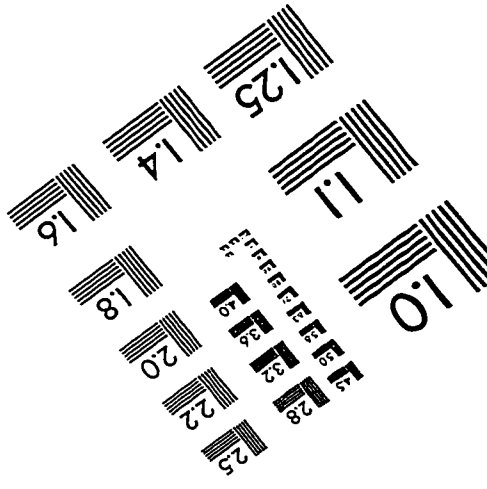

APPLIED IMAGE, Inc
1653 East Main Street
Rochester, NY 14609 USA
Phone: 716/482-0300
Fax: 716/288-5989